International Advanced Researches and Engineering Journal
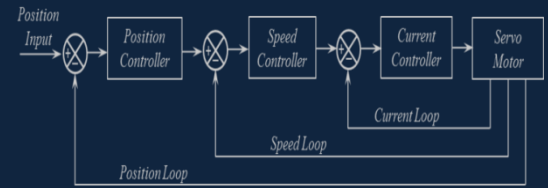
Aerospace Engineering,
Aquaculture and Fisheries Engineering,
Architecture,
Bioengineering,
Cell and Tissue Engineering
Chemical Engineering,
Civil Engineering,
Computer Engineering,
Electrical and Electronics,
Energy,
Environmental Engineering,
Food Engineering,
Geomatics Engineering,
Health in Engineering
Industrial Engineering,
Industrial Applications,
Machine Theory and Dynamics,
Marine Science and Technology,
Materials and Nano Science,
Manufacturing,
Mechanical Engineering,
Mechanics,
Mechatronics,
Medical,
Modeling and Simulation,
Physics Engineering,
Robotics,
Sustainable Science Technology,
Textile Engineering
Transport Science and Technology

$F=ma$

$E=mc^2$

$$\int \frac{dy}{dx} dt$$
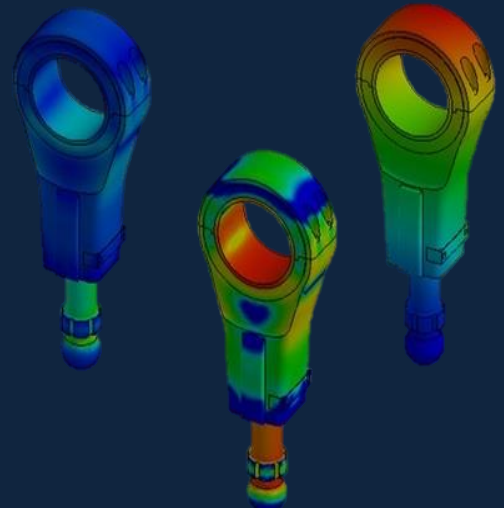
International Advanced Researches and Engineering Journal (IAREJ) is a double-blind peer-reviewed and publicly available online journal that has Editorial Board (https://dergipark.org.tr/en/pub/iarej/board). The editor in chief of IAREJ welcomes the submissions that cover theoretical and/or applied researches on **Engineering** and related science with Engineering. The publication language of the Journal is **English**. **Writing Rules** are given in Author Guidelines (https://dergipark.org.tr/en/pub/iarej/writing-rules). IAREJ publishes **original papers** that are research papers and technical review papers.

IAREJ publication, which is **open access**, is **free of charge**. There is no article submission and processing charges (APCs).

IAREJ is indexed & abstracted in:

Crossref (Doi beginning: 10.35860/iarej.xxxxxx)
Directory of Open Access Scholarly Researches (ROAD)
Directory of Research Journals Indexing (DRJI)
Google Scholar
Index Copernicus (ICI Journal Master List)
J-Gate
Rootindexing
Scientific Indexing Services (SIS)
TUBITAK ULAKBIM TR Dizin (TR index)
WorldCAT

Authors are responsible from the copyrights of the figures and the contents of the manuscripts, accuracy of the references, quotations and proposed ideas and the Publication Ethics (https://dergipark.org.tr/en/pub/iarej/page/4240).

Table of Contents

Research Article

The effect of different sliding speeds on wear behavior of ZrO₂ reinforcement aluminium matrix composite materials

İjlal Şimşek [a],* , Doğan Şimşek [b] and Dursun Özyürek [c]

ªKarabuk University, TOBB Technical Sciences Vocational School, Karabuk, 78050, Turkey
ᵇNational Defense University, Land Forces NCO Vocational School, Balikesir, 10100, Turkey
ᶜKarabuk University, Technology Faculty, Karabuk, 78050, Turkey

ARTICLE INFO	ABSTRACT
	Due to the many advantages it provides metal matrix composite materials, it is used as a publication in many industrial applications, especially in the automotive industry. Therefore, it is necessary to know the properties of these materials such as mechanical, tribological and corrosion. In this study, the effect of different sliding speeds was investigated on wear behavior of aluminum matrix composite materials produced by adding different amounts of ZrO_2 by mechanical alloying method. 4 different amounts (3%, 6%, 9% and 12%) ZrO2 were added to the aluminum 2% graphite matrix. Composite powders mechanically alloyed for 60 minutes, were produced green compact samples by cold pressed with a pressure of 700 MPa. The green compacts produced were sintered for 2 hours at 600 °C. The produced aluminum composites were characterized by microstructure, density and hardness measurements. Wear tests were carried out on a block on-ring type wear testing device, under 20 N load and three different sliding speed (0.2 ms^{-1}, 0.4 ms^{-1} and 0.6 ms^{-1}) and three different sliding distances (53 m, 72 m and 94 m). As a result of the studies, hardness and density values increased as the amount of ZrO_2 in the matrix increased. Wear test results showed that weight loss decreased with increasing amount of reinforcement in the matrix.

1. Introduction

Aluminium and its alloys are commonly used in aviation, automotive and defence sectors due to their low density, good mechanical properties and good corrosion properties [1,2]. However, relatively low wear resistance of aluminium and its alloys despite good mechanical properties restricts the use of these alloys in some tribological applications. The aluminium matrix composites (AMCs) display better wear performance when compared to aluminium alloys [3-5]. AMCs are manufactured with the continuous addition of fibre, short fibre and particle reinforcements. In many studies related to AMCs, it is reported that carbides [6-8], nitrides [9] and oxides [10, 11] are used as reinforcement agent. Particle reinforced AMCs are commonly used owing to their availability, low costs, mechanical properties and variety of production methods [12-14]. Along with these advantages, AMCs have other features such as high elasticity module, high hardness, good electricity, thermal conductivity and good corrosion resistance, as well [4, 12]. AMCs can be manufactured through fluid (infiltration) [15], solid (powder metallurgy) [16-20] and semi-solid (thixo-moulding) [21-23] methods. Prabhu et al. [24] reports that powder metallurgy (PM) offers numerous advantages and thus, this technology is more preferred in the production of AMCs. The biggest advantage of the PM method for AMC is that the reinforcement material can properly disperse within the matrix. Powder metallurgy method essentially consists of three phases: mixing the powders, pressing and sintering. Furthermore, mechanical alloying (MA), which is a powder metallurgy method, is preferred in the production of AMCs with better mechanical properties when compared to the other particle reinforced composite production methods [16]. In many studies, it was reported that reinforcement materials such

as Al_2O_3 [11, 15, 18] and SiC [6, 16, 23, 25] improved the wear resistance of AMC materials. Zirconia (ZrO_2) is considered as a good reinforcement material in AMC materials owing to its high hardness and high elasticity module. However, it has high thermal stability and thermal shock resistance at high temperatures. [1, 26]. Baghchesara et al. [27] reported in their study that the AMC materials produced at different casting temperatures with the addition of different amounts of ZrO_2 had improved mechanical properties thanks to the increasing amounts of ZrO_2 reinforcements. In their study, Ramachandra et al. [28] stated that weight loss decreased with the increasing amount of ZrO_2 added into the matrix. In the studies conducted in the literature, ZrO_2 reinforcement has been addressed in a limited manner.

In the present study, AMC materials were produced with the addition of different amounts of ZrO_2 into Al-%2 graphite matrix by using the MA method. The study aimed to determine the effects of ZrO_2 added into the AMC materials on microstructure, hardness and wear behaviours at different sliding speeds.

2. Materials and Method

In the experimental studies, aluminum (Al) powder (vol.%) having a size of <50 μm and a purity of 99.5% and graphite of 2% having a size of <40 μm were used as the matrix material. The Al matrix was reinforced with ZrO_2 (vol.%) having a powder size of 0-50 μm in three different amounts (3%, 6% 9% and 12%). The chemical composition of the AMCs powders produced is provided in Table 1.

The powders having the chemical composition given in Table 1 are mechanically alloyed in a planetary mill. During mechanical alloying (MA) processes, a stainless steel milling cell (400 ml), stainless steel balls having a diameter of 10 mm, a ball to powder ratio of 1:10, 1% of ethanol is used to prevent agglomeration, and a milling time of 60 minutes were used in the atmospheric environment. Mechanical alloying was performed in 30 minute periods. It was allowed to stand for 10 minutes between the periods to prevent the dust from overheating. In the mechanical alloying process, Fritsch Pulverisette brand planetary type mechanical alloying device was used. After mechanical alloying, powder size analysis was made from 12% ZrO_2 added composite powder. Particle analyzer Malvern brand 3000 was used for powder size analysis.

The average powder size of composite powders with 12% ZrO_2 added, (D50) is 55.89 μm. Mechanically alloyed Al composite powders were cold pressed (700 MPa) and green compacts of Ø10x7 mm were produced. The produced green compacts were sintered at 600 °C under argon for 120 minutes and cooled to room temperature in a furnace.

Table 1. Chemical composition of AMCs powders produced

Sample	Al (wt.%)	Grafit (wt.%)	ZrO_2 (wt.%)
AlGr	98	2	---
AlGr3ZrO2	95	2	3
AlGr6ZrO2	92	2	6
AlGr9ZrO2	89	2	9
AlGr12ZrO2	86	2	12

Standard metallographic treatments were applied for the microstructure analyses and the samples prepared were etched with a solution of 2 ml HF, 3 ml HCl, 20 ml HNO_3, 175 ml H_2O (Keller's) solution for 10-15 seconds. Microstructure analyzes of the etched samples were carried out by Carl Zeiss Ultra Plus Gemini Scanning Electron Microscope and Electron Diffraction Spectroscopy (SEM). In addition, the sintered samples were made by Rigaku brand XRD (X-ray diffraction) device. However, samples were characterized hardness and density measurements. Density measurements were made using density measurement kit in Precisa XB200h brand precision scale according to Archimedes' principle [29]. Density measurements were taken on three samples and averaged. Hardness measurements were taken with using Shimadzu microhardness tester for 10 seconds by using HMV2. The hardness measurements were obtained by using three different samples, at five different points and used averaged. Wear tests were carried out at four different sliding distances (53 m, 72 m and 94 m) at three different sliding speeds (0.2 ms^{-1}, 0.4 ms^{-1} and 0.6 ms^{-1}) under different loads of 20 N on a pin on disc wear test device according to ASTM G99-05 standard [30]. The sliding distance used in the wear tests was determined according to stopping distances of a vehicle in different speeds [31]. Before each wear test, the surface of samples and disks were cleaned with acetone. In the wear tests, three different samples were tested for each parameter and the results were averaged. Wear rates were calculated by the equation given in Equation 1 using the weight loss results obtained [30].

$$Wa = \Delta m/(M.s.\rho) \qquad (1)$$

Wherein, Wa is the wear rate, Δm is the weight loss (g) obtained after the wear test, M is the load (N) used in the tests, s is the sliding distance (m), and ρ is the density (g/cm³) of the wear sample. After the wear test, worn surface SEM images were examined and the active wear mechanisms were tried to be determined.

3. Results and Discussion

3.1 Microstructure examinations

Microstructure SEM images of composite materials produced by adding different amounts of ZrO_2 are given in Figure 1.

When the SEM images of AMC materials produced with the addition of different amounts of ZrO_2 given in Figure 1 are examined, insoluble graphite particles (grey areas 2. location) are observed in the matrix material (Figure 1.a). It is seen that these graphite particles in the matrix material are not coarse particles as the amount of reinforcement material increases. The reason why graphite particles are observed in the structure is that it further contracted with the influence of hard reinforcement particles added into the matrix along with high-energy balls during MA. Table 2 shows the EDS analysis results of AMC materials with different amounts of ZrO_2 added.

In the study conducted by Şimşek [32], similar results were obtained. Furthermore, Chu et al. [33] reported that smaller graphite particles fully turned into Al_4C_3 compound and bigger ones appeared as graphite particles. Also, the SEM images show that ZrO_2 added into the matrix (light grey areas, 4. location) are particularly located on the grain boundaries. Sekar et al. [34] and Baghchesara et al. [27] stated in their studies that ZrO_2 tended to agglomerate on the grain boundaries. XRD analysis results of composite materials after the addition of AlGr and 12% ZrO_2 are given in Figure 2.

When the XRD results of AMC materials after the addition of AlGr and 12% ZrO_2 are examined, it is seen that the matrix material (AlGr) has Al (Card number: 9011602) and graphite (Card number: 00-056-0159). However, Al_4C_3 (Card number: 00-035-0799) phase, which was expected to occur in the matrix, cannot be observed. The failure to observe Al_4C_3 in the structure is attributed to the low range of XRD scan or nanosize of Al_4C_3 forming in the structure.

Table 2. EDS analysis results of AMC materials with different amounts of ZrO_2

Location	Al	C	Zr	O
1	93.22	4.64	-	2.14
2	81.23	12.15	-	6.62
3	94.14	3.73	-	1.45
4	0.71	3.73	66.59	28.97
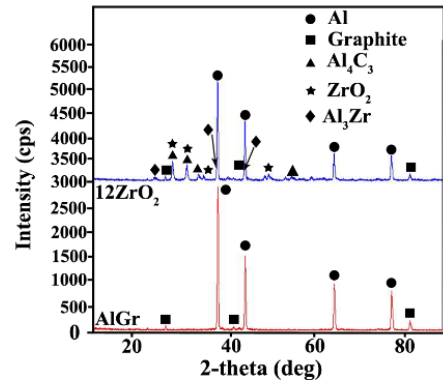
Figure 2. XRD result of the composite material produced with AlGr and 12% ZrO_2 reinforcement.
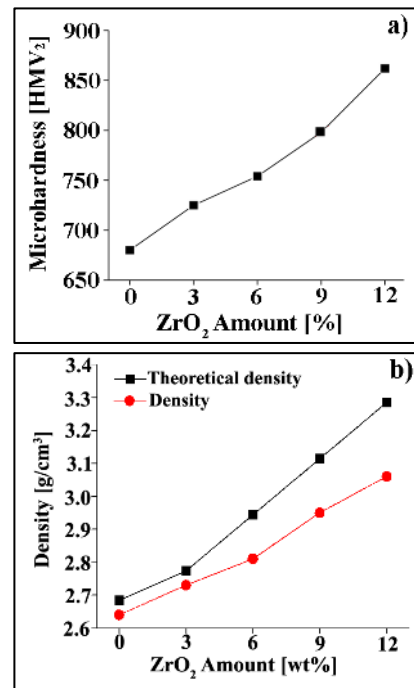
Figure 3. Changes in hardness (a) and density (b) of composite materials with different amounts of ZrO_2 reinforcement

In their study, Bostan et al. [35] reported that Al_4C_3 compounds formed at nano size in Al-C system produced with MA method. However, in the XRD results of the AMC material with 12% ZrO_2 added, it was observed that Al_3Zr (Card number: 01-074-5295) phase formed along with the expected Al_4C_3 phase. The presence of Al_4C_3 phase in the structure of AMC material after the addition of 12% ZrO_2 is due to the fact that graphite further contracts and fully dissolves in the structure with the influence of hard reinforcement particles during MA. Hardness and density results of AMC materials after the
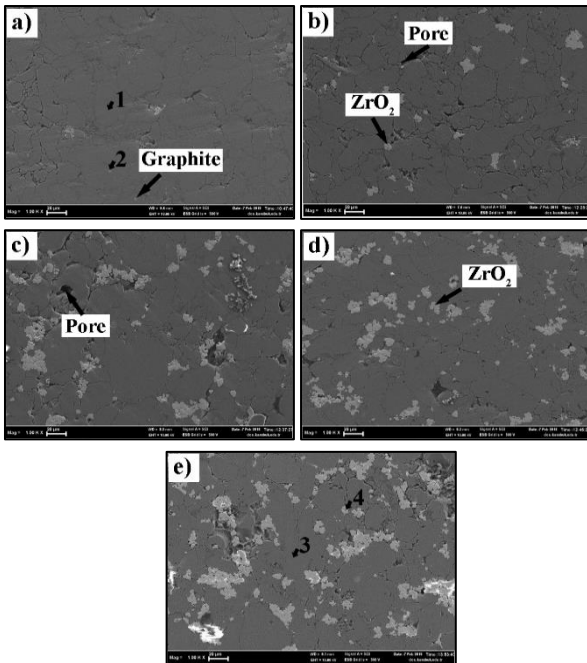

Figure 1. Microstructural SEM images of composite materials with different amounts of ZrO_2 reinforcement; AlGr (a), 3% ZrO_2 (b), 6% ZrO_2 (c), 9% ZrO_2 (d) and 12% ZrO_2 (e).

addition of different amounts of ZrO$_2$ are given in Figure 3.

When the hardness results of the AMC materials after the addition of different amounts of ZrO$_2$ as given in Figure 3.a are examined, it is seen that hardness increases as the amount of reinforcement increase. While the lowest hardness value was obtained as 680 HMV in matrix material (AlGr), the highest hardness value was obtained as 862 HMV in the AMC material with the addition of 12% ZrO$_2$. The increase in hardness is attributed to the hard secondary phase particles ex-situ added into the matrix and the dislocation accumulation occurring on the matrix interface. Das et al. [1] obtained similar results in ZrO$_2$ reinforced composite materials produced with the casting method. They reported that the hardness increased since a dislocation accumulation occurred on the matrix-reinforcement interface during cooling due to the lower coefficient of thermal expansion of the reinforcement material (ZrO$_2$) when compared to Al. Again when the density changes of the AMC materials with the addition of different amounts of ZrO$_2$ as given in Figure 3.b are examined, it is seen that density increases as the amount of reinforcement increases. While the lowest density value was obtained as 2.6 g/cm^3 in the matrix material, the highest density value was obtained as 3.06 g/cm^3 in the AMC material after the addition of 12% ZrO$_2$. Based on the results, it can be stated that the density values increased as expected. This increase in the density values results from higher density of the reinforcement material (ZrO$_2$ 5.68 g/cm^3) than the matrix material (AlGr 2.64 g/cm^3). Similar results were obtained in the previously conducted studies [27, 36]. Data related to the weight losses and wear rates of the AMC materials after the addition of different amounts of ZrO$_2$ are given in Figure 4.

When the weight losses of the AMC materials containing different amounts of ZrO$_2$ at different sliding speeds as given in Figure 4 are examined, it is seen that, as expected, weight loss decreases at all sliding speeds as the amount of ZrO$_2$ increases. The obtained results are compatible with the hardness results given in Figure 3. However, a sudden increase is observed in the weight loss results of the AMC material containing 6% ZrO$_2$ at 72 m sliding distance given in Figure 4.a. This sudden increase in the weight loss results from a large particle breaking off the material during wear [18, 37]. The wear rate results support these results, as well. What is expected in the wear test results is an increase in sliding distance and decrease in weight loss. As expected, the lowest weight loss was recorded at 0.6 ms^{-1} sliding speed. However, contrary to expectations, the highest weight loss was observed at 0.4 ms^{-1} sliding speed. The decrease in the weight loss at 0.6 ms^{-1} sliding speed results from the protective effect of the oxide layer forming on the surface. As the sliding speed increases, the increasing temperature resulting from friction leads to the formation of a more effective (protective) oxide layer on the surface. Due to the lubricating feature of the emerging oxide layer, the weight loss decreases [17, 38]. On the other hand, the highest weight loss obtained at 0.4 ms^{-1} sliding speed can be explained with the breaking of the oxide layer forming on the surface. Similar results were reported in a previously conducted study [39]. Furthermore, the friction coefficient results given in Figure 5 support these results. Friction coefficients of the AMC materials produced with the addition of different amounts of ZrO$_2$ are given in Figure 5.
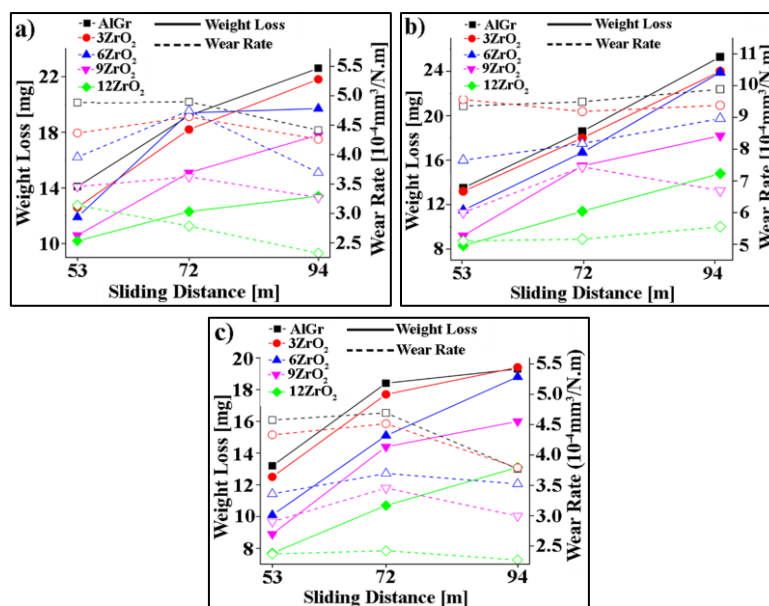

Figure 4. Weight losses and wear rates of composite materials with different amounts of ZrO$_2$ reinforced; 0.2 ms^{-1} (a), 0.4 ms^{-1} (b), and 0.6 ms^{-1} (c).
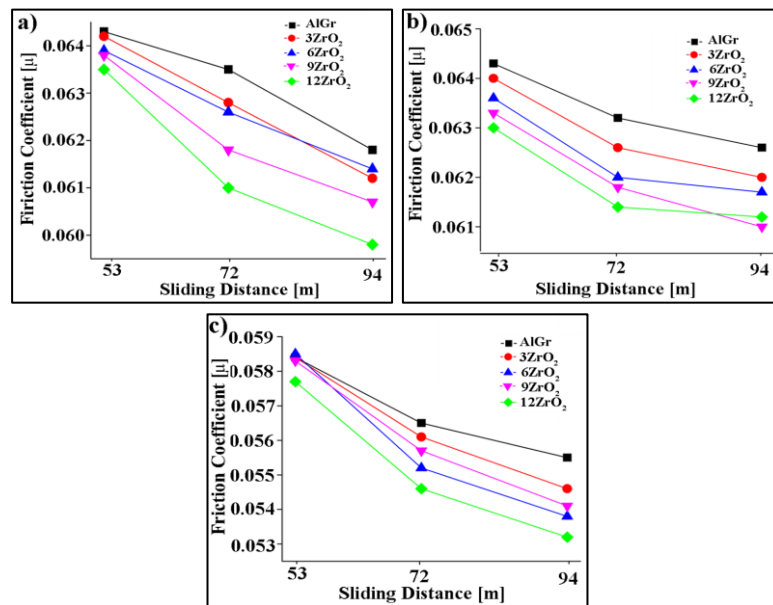
Figure 5. Friction coefficients of composite materials with different amounts of ZrO$_2$ reinforced; 0.2 ms^{-1} (a), 0.4 ms^{-1} (b), and 0.6 ms^{-1} (c).

When the friction coefficients of the AMC materials containing different amounts of ZrO$_2$ at different sliding speeds as given in Figure 5 are examined, it is seen that the friction coefficient decreases as the amount of reinforcement increases. This decrease in the friction coefficient results from the decrease in disc/sample contact surface as the amount of reinforcement into the matrix increases. On the other hand, it is expected that the friction coefficient of the material with high hardness value is low [18]. The decrease in the friction coefficient is compatible with the hardness results given in Figure 3. Also, it is seen that the friction coefficient decreases along with increasing sliding distances at all sliding speeds. Accordingly, the friction coefficient decreases due to the protective oxide layer forming on the surface and also the solid lubricating effect of the graphite within the matrix [32, 38]. On the other hand, it is expected that the friction coefficient decreases as the sliding speed increases. While these results are obtained in short sliding distances (53 m and 72 m), it is not in question in longer sliding distances (94 m). Especially after 72 m sliding distance at 0.4 ms^{-1} sliding speed, when the friction coefficients are compared to the other sliding speeds, they are found to be high. This increase in the friction coefficients is attributed to the increase in the sample surface roughness. The increase in the weight loss in the weight loss results given Figure 4.b is a clear indicator of this situation. Also, the worn surface SEM images given in Figure 6.b support this finding. The worn surface SEM images of the AMC materials containing 12% ZrO$_2$ at different sliding speeds are given in Figure 6.

When the worn surface SEM images of the AMC materials containing 12% ZrO$_2$ at different sliding speeds given in Figure 6 are examined, the spalls occurring on the worn surface at all sliding speeds can be clearly observed.

Deformation marks can be clearly observed in the worn surface obtained at 0.6 ms^{-1} sliding speed (Figure 6.c). However, when the worn surfaces with 0.6 ms^{-1} sliding speed are compared with the worn surfaces obtained at other sliding speeds, it is seen that traces of deformation disappear, and a more planar surface is formed. It is thought that the heat released by friction with increased sliding speed and the protective effect of the hard oxide layer formed on the surface are caused by the increase of wear resistance. It is stated that similar results were obtained in a previous study [37]. Also, it is understood that the fractures in sheet form observed on the worn surface obtained at 0.4 ms^{-1} sliding speed (Figure 6.b) are more apparent and abundant when compared to the worn surfaces obtained at the other speeds (0.2 ms^{-1} and 0.6 ms^{-1}). The weight loss and friction coefficient results obtained in the study support this situation, as well. The worn surface mapping images of the AMC materials containing 12% ZrO2 at different sliding speeds are given in Figure 7.
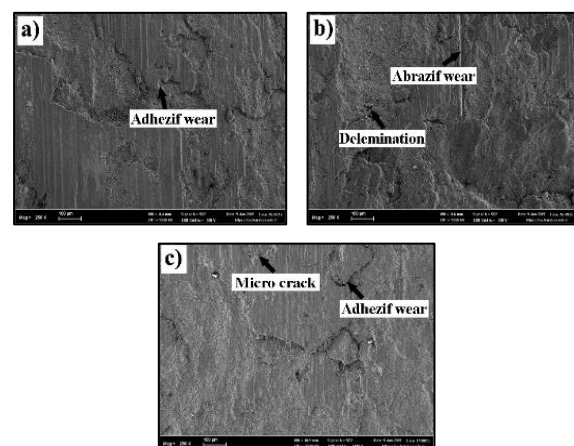

Figure 6. SEM images of worn surfaces on different sliding speed of composite materials with added 12% ZrO2
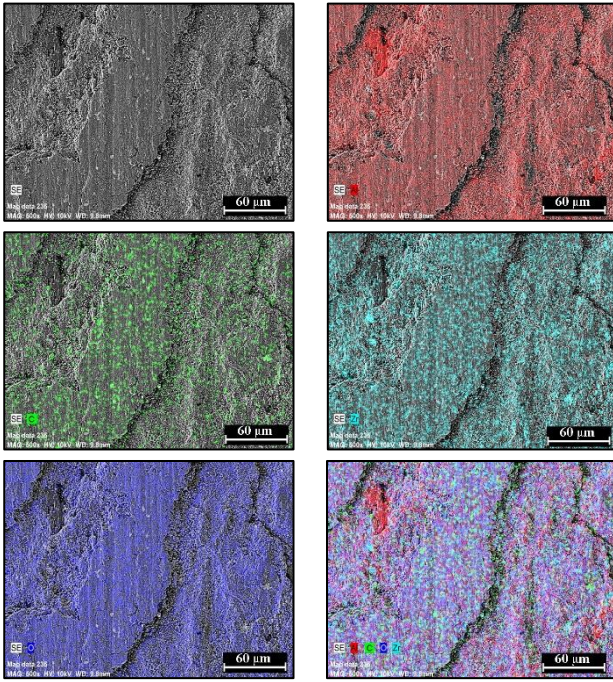a) 0.2 ms^{-1}, b) 0.4 ms^{-1}, c) 0.6ms^{-1}

Figure 7. Worn surface mapping images of different sliding speed of composite materials with added 12% ZrO_2

When the mapping images of the AMC materials containing 12% ZrO_2 at 0.6 ms^{-1} sliding speed given in Figure 6 are examined, the oxide layer formed on the surface is clearly understood. In the SEM images given in Figure 1, it is understood that the reinforcing material (ZrO_2) cluster especially on the grain boundaries is disperse on the worn surface. It is believed that ZrO_2, which is clustered at grain boundaries, is caused by re-burial on the sample surface without leaving the tribological system during wear. Due to weak particle binding, surface contamination and oxidation, micro cracks form on the sample surface as a result of a series of successive events. The formation of scaly spills, deep grooves, pits with the progression of the formed micro cracks causes delamination on the worn surface. The worn surface SEM images given in Figure 6 clearly show the delamination areas. The worn surface SEM images given in Figure 6 clearly show the delamination areas. In addition, it is observed that there are regional adhesive and abrasive wear mechanisms on the wear surfaces.

4. Conclusions

The results reached in the study where the wear behaviours of the AMC materials containing different amounts of ZrO_2 added into AlGr matrix at different sliding speeds were examined are as follows:

- ZrO_2 particles added into the matrix at different amounts get lumpy in the structure and are located on the grain boundaries, in particular.
- In XRD analysis results, Al_4C_3 phase, which was expected to form in the matrix (AlGr) material, could

not be encountered. On the other hand, the expected Al_4C_3 phase and Al_3Zr phase were observed in XRD results of the AMC material containing 12% ZrO_2.
- According to the hardness results, hardness of the AMC material increased as the amount of added reinforcement material increased, and the highest hardness value was obtained in the AMC material containing 12% ZrO_2.
- According to the density results, density of the AMC materials increased as the amount of added reinforcement material increased, and the highest density was obtained in the AMC material containing 12% ZrO_2.
- In the wear test results, lowest weight loss and wear rate were obtained at 0.6 ms^{-1}.
- According to the results related to friction coefficient, the lowest friction coefficient was obtained at 0.6 ms^{-1} sliding speed.

Declaration

References

1. Das, S., Das, S., and Das, K., *Abrasive wear of zircon sand and alumina reinforced Al–4.5 wt%Cu alloy matrix composites-A comparative study.* Composites Science and Technology, 2007. **67**(3-4): p. 746-751.

2. Idusuyi, N., and Olayinka, J. I., *Dry sliding wear characteristics of aluminium metal matrix composites: a brief overview.* Journal of Materials Research and Technology. 2019, **8**(3): p. 3338-3346.

3. Hemanth, J., *Tribological behavior of cryogenically treated B_4Cp/Al–12% Si composites.* Wear, 2005. **258**: p. 1732-1744.

4. Özyürek, D., Tekeli, S., *An investigation on wear resistance of SiCp-reinforced aluminium composites produced by mechanical alloying method.* Science and Engineering of Composite Materials, 2010. **17**(1): p. 31-38.

5. Çam, S., Demir, V., and Özyürek, D., *Wear behaviour of A356/TiAl$_3$ in situ composites produced by mechanical alloying.* Metals, 2016. **6**: p. 34-42.

6. Parvin, N., Assadifard, R., Safarzadeh, P., Sheibani, S., and Marashi, P., *Preparation and mechanical properties of SiC-reinforced Al6061 composite by mechanical alloying.* Materials Science and Engineering A, 2008. **492:** p. 134-140.

7. Sozhamannan, G.G., Yusuf, M.M., Aravind, G., Kumaresan, G., and Velmurugan, K., Venkatachalapathy, V.S.K., *Effect of applied load on the wear performance of 6061 Al/ nano TiCp/ Gr hybrid composites.* Materials Today: Proceedings, 2018. **5**: p. 6489-6496.

8. Şimşek, D., Şimşek, İ., Özyürek, D., *Production and Characterization of Al-SiC Composites by Mechanical Milling.* BEÜ Fen Bilimleri Dergisi, 2019. **8** (1): p. 227-233.

9. Zi-yang, X., Guo-qin, C., Gao-hui, W., Wen-shu, Y., and Yan-mei, L., *Effect of volume fraction on microstructure and mechanical properties of Si3N4/Al composites.* Transection of Nonferrus Metals Society of China, 2011. **21**: p. 285-289.

10. Ahamed, H., and Senthilkumar, V., *Role of nano-size reinforcement and milling on the synthesis of nano-crystalline aluminium alloy composites by mechanical alloying.* Journal of Alloys and Compounds, 2010. **505**: p. 772-782.

11. Zhu, H., Jar, C., Song, J., Zhao, J., Li, J., and Xie, Z., *High temperature dry sliding friction and wear behavior of aluminum matrix composites (Al₃Zrþa-Al₂O₃)/Al.* Tribology International, 2012. **48**: p. 78-86.

12. Özyürek, D., Tuncay, T., Evlen, H., and Çiftci, I., *Synthesis, characterization and dry sliding wear behavior of in-situ formed TiAl₃ precipitate reinforced A356 alloy produced by mechanical alloying method.* Materials Research, 2015. **18**(4): p. 813-820.

13. Torralba, J.M., da-Costa, C.E., and Velasco, F., *P/M aluminum matrix composites: an overview.* Journal of Materials Processing Technology, 2003. **133**: p. 203-206.

14. Durai, T.G., Das, K., Das, S., *Corrosion behavior of Al-Zn/Al₂O₃ and Al-Zn-X/Al₂O₃ (X=Cu, Mn) composites synthesized by mechanical–thermal treatment.* Journal of Alloys and Compounds, 2008. **462**: p. 410-415.

15. Aksoz, S., Bican, O., Calin, R., and Bostan, B., *Effect of T7 heat treatment on the dry sliding friction and wear properties of the SiC-reinforced AA 2014 aluminium matrix composites produced by vacuum infiltration.* Proceedings of the Institution of Mechanical Engineers, Part J: Journal of Engineering Tribology, 2013. **228**(3): p. 312-319

16. Özyürek, D., and Tekeli, S., *An investigation on wear resistance of SiCp-reinforced aluminum composites produced by mechanical alloying.* Science and Engineering of Composite Materials, 2010. **17**(1): p. 31-38.

17. Şimşek, İ., Şimşek, D. Özyürek, D., Investigation of the Effect of Ni Amount on the Wear Performance of A356 Cast Aluminum Alloys. Metallurgist (2020). https://doi.org/10.1007/s11015-020-00917-w

18. Özyürek, D., Tekeli, S., Güral, A., Meyveci, A., and Gürü, M., *Effect of Al₂O₃ amount on microstructure and wear properties of Al-Al₂O₃ metal matrix composites prepared using mechanical alloying method.* Powder Metallurgy and Metal Ceramics, 2010. **49**(5-6): p. 50-57.

19. Özyürek, D., and Tekeli, S., *Wear properties of titanium and Ti6Al4V titanium alloy by mechanical milling.* High Temperature Materials and Processes, 2011. **30**(1-2): p. 175-180.

20. Aydın, D.Y., Gürü, M., Ipek, D., and Özyürek, D., *Synthesis and characterization of zinc fluoroborate from zinc fluoride and boron by mechanochemical reaction.* Arabian Journal for Science and Engineering, 2017. **42**: p. 4409-4416.

21. Aztekin, H., Özyürek, D., and Çetinkaya, K., *Production of hypo-eutectic Al-Si alloy based metal matrix composite with thixomoulding processing.* High Temperature Materials and Processes, 2010. **29**(3): p 169-178.

22. Özyürek, D., *The effect of semi-solid processing parameters on microstructure in Al-7wt.%Si alloy.* Scientific Research and Essays, 2011. **6**(29): p. 6222-6226.

23. Özyürek, D., Yıldırım, M., and Çiftçi, İ., *The tribological properties of A356-SiCp metalmatrix composites fabricated by thixomoulding technique.* Science and Engineering of Composite Materials, 2012. **19**(4): p. 351-356.

24. Prabhu, B, Suryanarayana, C., An, L., and Vaidyanathan, R., *Synthesis and characterization of high volume fraction Al-Al₂O₃ nanocomposite powders by high-energy milling.* Materials Science and Engineering A, 2006. **425**: p. 192-200.

25. Wang, Y.Q., and Song, J.I., *Temperature effects on the dry sliding wear of Al₂O₃f/SiCp/Al MMCs with different fiber orientations and hybrid ratios.* Wear, 2011. **270**: p. 499-505.

26. Zhu, H.G., Ai, Y.L., Min, J., Wu, Q., and Wang, H.Z., *Dry sliding wear behavior of Al-based composites fabricated by exothermic dispersion reaction in an Al-ZrO₂-C system.* Wear, 2010. **268**: p. 1465-1471.

27. Baghchesara, M.A., Abdizadeh, H., Baharvandi, H.R., *Microstructure and mechanical properties of aluminum alloy matrix composite reinforced with ZrO₂ particles.* Asian Journal of Chemistry, 2010. **22**(5): p. 3824-3834.

28. Ramachandra, M., Abhishek, A., Siddeshwar, P., and Bharathi, V., *Hardness and wear resistance of ZrO₂ nano particle reinforced Al nanocomposites produced by powder metallurgy.* Procedia Materials Science, 2015. **10**: p. 212-219.

29. Şimşek, İ., Yıldırım, M., Özyürek, D. and Şimşek, D. *Basınçsız infiltrasyon yöntemiyle üretilen SiO2 takviyeli alüminyum kompozitlerin aşınma davranışlarının incelenmesi.* Politeknik Dergisi, 2019, **22**(1)**:** p. 81-85.

30. Şimşek, İ., Şimşek, D. and Özyürek, D. *Investigation of the Effect of Ni Amount on the Wear Performance of A356 Cast Aluminum Alloys.* Metallurgist, 2020, **63**(9-10): p. 993-1001.

31. General Directorate of Highways, "Vehicle Stopping and Transfer Times", Turkey

    http://www.kgm.gov.tr/Sayfalar/KGM/SiteTr/Trafik/Durma Intikal.aspx. (last access date:17.09.2019)

32. Simsek, I., *The effect of B₄C amount on wear behaviors of Al-Graphite/B₄C hybrid composites produced by mechanical alloying*, Journal of Boron, 2019. **4**(2): p. 100-106.

33. Chu, H.S., Liu, K.S., and Yeh, J.W., *Damping behavior of in situ Al-(graphite, Al₄C₃) composites produced by reciprocating extrusion.* Journal of Materials Research, 2001. **16**(5): p. 1372-1380.

34. Sekar, K., Jayachandra, G., and Aravindan, S., *Mechanical and welding properties of A6082-SiC-ZrO₂ hybrid composite fabricated by stir and squeeze casting.* Materials Today: Proceedings, 2018. **5**: p. 20268-20277.

35. Bostan, B., Ozdemir, A.T., and Kalkanli, A., *Microstructure characteristics in Al-C system after mechanical alloying and high temperature treatment.* Powder Metallurgy, 2004. **47**(1): p. 37-42.

36. Kumar, K.R., Pridhar, T., and Sree, V.S., *Mechanical properties and characterization of zirconium oxide (ZrO₂) and coconut shell ash(CSA) reinforced aluminium (Al 6082) matrix hybrid composite.* Journal of Alloys and Compounds, 2018. **765**: p. 171-179

37. Rao, R. N. and Das, S. *Effect of SiC content and sliding speed on the wear behaviour of aluminium matrix composites.* Materials & Design, 2011, **32**(2): p. 1066-1071.

38. Özyürek, D., Tunçay, T., and Kaya, H., *The effects of T5 and T6 heat treatments on wear behaviour of AA6063 alloy.* High Temperature Materials and Processes, 2014. **33**(3): p. 231-237.

39. Özyürek, D, Ciftci, I., and Tuncay, T., *The effect of aging and sliding speed on wear behaviour of Cu-Cr-Zr alloy.* Materials Testing, 2013. **55**(6): p. 468-471.

Research Article

Determination of the distribution of different filling materials in SBR matrix compounds by image processing

Saban Bulbul [a],* and Hasan Serdar [a]

ᵃNecmettin Erbakan University, Faculty of Seydişehir Ahmet Cengiz Engineering Faculty, Konya, 42370, Turkey

ARTICLE INFO	ABSTRACT
	In this study, the distribution of walnut shell ash and cone ash, which were used in different proportions as the filling materials of SBR rubber compounds, in the matrix were investigated by the developed image processing program. Styrene-Butadiene Rubber (SBR 1502) was employed as the main matrix material. Adhering to the same compound in the experiments, in addition to the carbon black in the compound, 5 different and 10% by mass of Walnut Shell Ash (WSA) was added to the dough, and the Cone Ash (CA) by 5% and 10% by mass, creating a total of 5 different compounds. SEM images of the rupture surfaces were taken and transferred to the developed image processing program, in which the areas covered by walnut shell ash and cone ash in the images were determined. The number of designated surface areas and the area it covers on the image were removed.

1. Introduction

Rubber materials are used in many industrial areas such as automobile wheels, windshield wipers, toys, water pipes and seals and especially shoe soles. That's why; Many scientific articles and studies on rubbers, fillers, and mechanical properties have been made [1-5].

With the increase in the use of synthetic rubbers, it also brought forward some features sought in elastomer materials. These are lightness, flexibility, dimensional stability, tensile strength, dielectric properties and wear resistance. Also, aging properties are desired. It is a known fact that synthetic rubbers have an aging feature in a long time compared to natural rubber. It is necessary to investigate the use of SBR rubber on the shoe outsole. To have the properties expected from the product to be obtained from SBR and other rubber compounds, a large number of fillers and additives are added to the compound pulps [6]. Moreover, carbon black and silicate groups are the leading materials added to the rubber paste. However, due to the unstable oil prices, it has been given importance to use organic and inorganic materials as fillers [7,8]. It is remarkable that different fillers such a

glass sphere, rice husk, wollastonite, mica powder, gum, carbon black, phosphate, nano clay, silica, calcite, blast furnace flue powder, regenerated rubber, wood ash, and nano calcium carbonate, etc. are added to the rubber compounds [9–15]. Environmental awareness is one of the primary reasons that scientists use different materials that cannot be recycled as fillers. Also, there are many studies to improve the mechanical and physical properties of the compounds and to decrease the cost.

In our previous study [16], a certain proportion of carburized hazelnut shells were added to a Nitrile-Butadiene Rubber (NBR) matrix rubber paste, and as a result, made a study to determine the effect of crosslink density on the mechanical properties. Although it causes an increase in the stiffness of the compounds with increasing crosslink density, it is advantageous in rupture strength and rupture elongation. It was also sorted out that increased nutshell ash increased density [16]. In another study, the recovery of the mechanochemical properties of Ethylene Propylene Diene (EPDM) rubber, which is a waste, was carried out as a recovery material under a specific working condition using Disulfide Oil (DSO), which is an oily waste produced in gas refineries.

* Corresponding author. Tel.: +0-332-582-6000; Fax: +0-332-582-0450
E-mail addresses: sabanbulbul42@hotmail.com (S. Bulbul), hserdar@erbakan.edu.tr (H. Serdar)
ORCID: 0000-0002-9268-1469 (S. Bulbul), 0000-0003-3253-7390 (H. Serdar)

20-80% of waste rubber was incorporated into the raw rubber. Crosslink densities sol-gel and Mooney Viscosity methods were used in the produced compounds. In the compounds up to 60% by mass, no adverse effects were observed on combustion and optimum hardening time [17].

It is known that the distribution of filling materials added to the rubber matrix significantly affects the mechanical and physical properties. It is not possible to determine the fill distributions by looking only at the SEM images. For this reason, it has become important to analyze SEM images using image processing methods. Image analysis is an approach used to obtain meaningful information from images by putting algorithms on image data or performing a series of calculations in images [18]. Image processing work generally consists of data collection, data processing and interpretation of data [19]. In recent years, the use of image analysis has become one of the very powerful analytical techniques in evaluating material images, as in every field. This is done by using pictures taken through a camera and by applying a standard procedure to evaluate the data obtained from pictures [20].

This study aims to identify the volumes occupied by the fillings in the matrix material due to the recovery on the rupture surfaces with the help of image processing on SEM images and to design a standard operating procedure that will provide comparable results in future studies. In the study carried out, SEM images were analyzed with the help of the developed image processing software. The Otsu method was used to divide images in this study into correct sections [21].

2. Material and Method

SBR, filling and additive materials used in the study were supplied by all LBS Composition and Laboratory Technologies LTD of Turkey. The properties and trade names of rubber and fillers used in the study are given in Table 1. Pine cones were collected from pine trees in the central district of Manisa in Turkey. The walnut shells were collected from the walnut tree in Inegol of Bursa in Turkey. 5 different compounds were obtained by adding walnut shells and cones of 5% and 10% to the compounds used in experimental studies. These are expressed as O (Original), WSA5, WSA10, CA5, CA10. Filling and additive ratios added to the compounds shown in Table 2 are given by mass ratios.

The dough compounds preferred in the experiment were homogenously mixed for 5 minutes at 80 ºC and 60 rpm in a laboratory-type Banbury. The mixed dough was conditioned for 24 hours under room conditions. Then, in addition to carbon black, in the SBR rubber two-cylinder open mixer (Guncanlar brand), 0 %, 5 %, 10 % walnut shell ash and cone ash were added to the compounds and mixing was continued for another 5 minutes. Finally, sulfur, process facilitators, anti-aging, vulcanizers were added and mixing was continued for another 2 minutes. In total, mixing was carried out for 12 minutes at 60 ºC and 40 rpm and the process was completed. After the mixing process, the vulcanization process was completed by holding the dough mixture under the pressure of 160 ºC and 16 MPa for 6 minutes in 180x120x3 mm hot press molds.

Table 1 Technical properties of filling materials used in the study

Filling	Trade Names	Density (g/cm^3)	Grain size (μm)
Styrene-Butadiene Rubber	SBR 1502	0.4	-
Carbon Black	HAF N330	1.8	0.028
Silica	Egesil BS 20 A	2	20
Walnut Shell Ash	-	2.2	20
Cone Ash	-	2.1	10

Table 2. Mass ratios of fillers and additives used in the compound

Filling and Additives	O	WSA5	WSA10	CA5	CA10
SBR 1502	100	100	100	100	100
Carbon Black	70	70	70	70	70
Walnut Shell Ash	0	5	10	0	0
Cone Ash	0	0	0	5	10
Zinc Active	4	4	4	4	4
Sulfur	1.5	1.5	1.5	1.5	1.5
DPG	1	1	1	1	1
DM	1	1	1	1	1
CZ	1	1	1	1	1
Stearic acid	2	2	2	2	2
PEG 4000	2	2	2	2	2
MBT	5.5	5.5	5.5	5.5	5.5

All experiments and conditioning processes were carried out by the ISO norms set for rubber-based shoe sole materials. Samples were made after 24 hours at 23 ° C (± 2 ° C Temperature tolerance) and 50% relative humidity before testing.

The tensile test was carried out on the Tinius brand H25KS model pulling device at 10 mm/s pulling speed according to ISO 37 standard. After the rupture test, the morphology of the rupture surfaces of the samples was examined by using Zeiss Ultra/Plus scanning electron microscope (SEM). The rupture surfaces of the samples are coated with 5 nm thick pure gold to increase its conductivity [22]. During the examination of the microstructure images, the operating voltage of the microscope was chosen as 20 kV.

To detect the volumes occupied by the fillings in the matrix material due to the recoveries they create on the rupture surfaces, it is necessary to check the regions where the rebounds and to perform image analysis accordingly. In computerized image and image processing, point-based, statistical, spatial filtering, Fourier transform and morphological processes can be used to highlight or characterize the images [23]. In this study, the Otsu method was used for the segmentation of SEM images in image processing. The grassy algorithm divides pixels into two classes, as foreground and background, and calculates them based on a single density threshold. Thus, the variance between classes is maximized.

Otsu Algorithm:
1. Calculation of all point densities
2. Calculation of the probability of the initial weights $w_i(0)$ and their mean $\mu_i(0)$
3. Weights of all possible threshold values (t = 1,…) are updated for maximum intensity w_i and averages μ_i
4. Class variance $\sigma_b^2(t)$ is calculated
5. Desired threshold reaches maximum

Each of the recovery created by the fillers in the matrix material on the rupture surfaces was found separately on the SEM image and the volume it occupied on the image was given in percentage. In this study, SEM images were analyzed with the help of developed image processing software.

3. Evaluating Experimental Studies

SEM images of the compounds formed by adding 0, 5% and 10% cone ash and walnut shell ash to the original mixture are given in Figures 1-5.
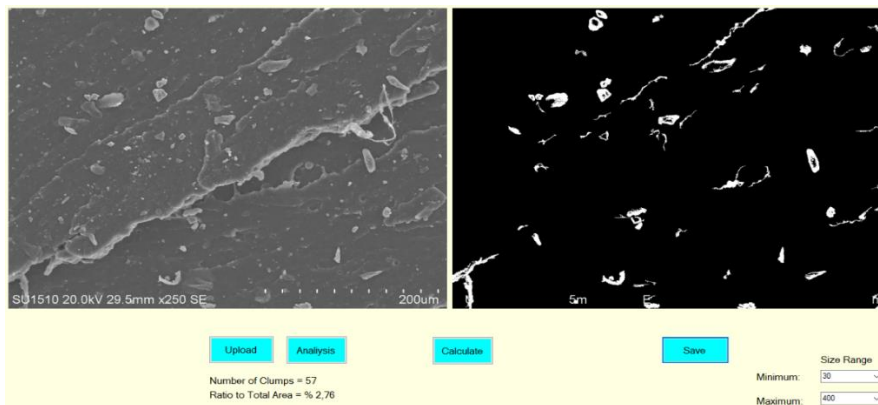

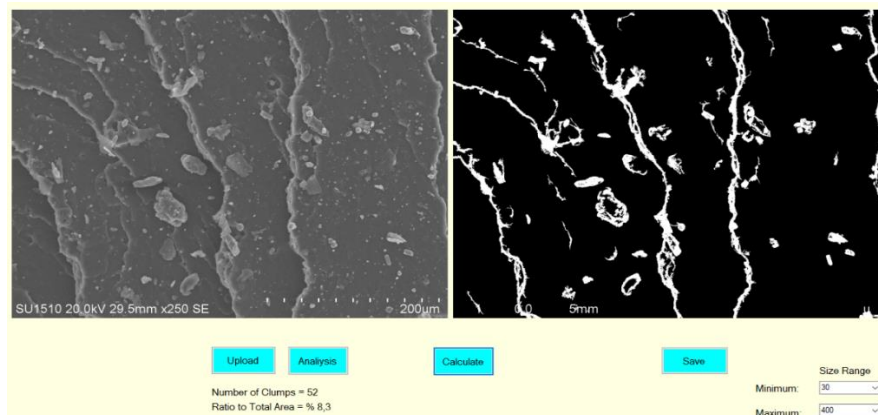Figure 1. SEM and analysis results of the rupture surface of the O compound.

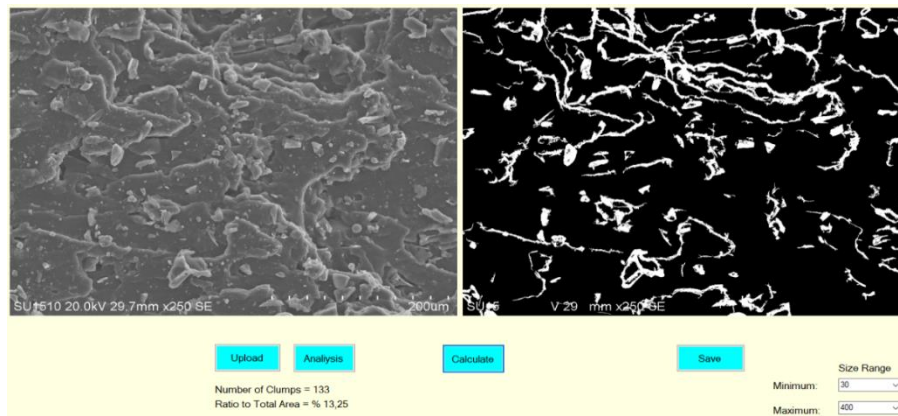Figure 2. SEM and analysis results of the rupture surface of CA5 compound

Figure 3. SEM and analysis results of the rupture surface of CA10 compound
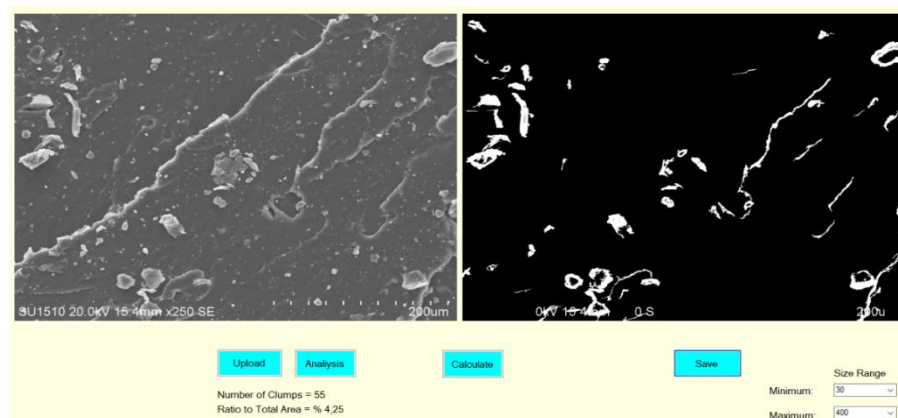
Figure 4. SEM and analysis image of the rupture surface of WSA5 compound
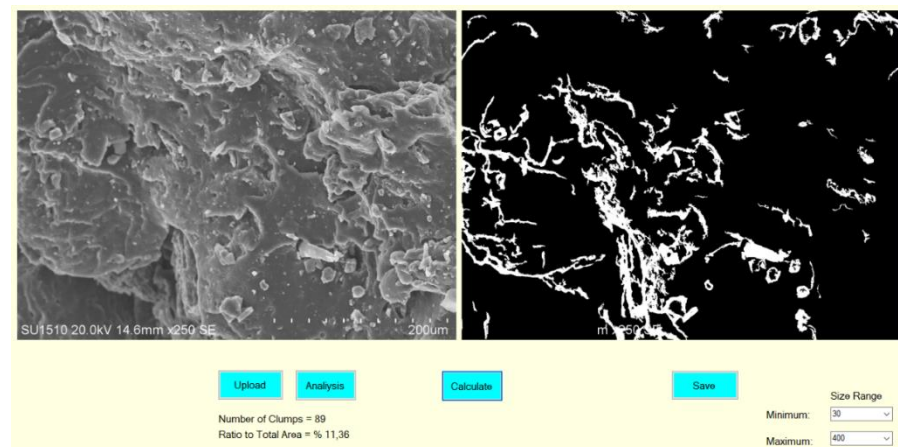
Figure 5. SEM and analysis results of the rupture surface of WSA10 compound

When the rupture surfaces were analyzed as shown in Figures 1-5 with the help of the developed image processing software, it was observed that the fillings were detached from the material during drawing and as a result, deep gaps were formed on the sample surfaces. It is understood from the SEM images and image processing software results that the filling density increases as the ratio of cones ash and walnut shell ash added to the compounds increases. When Figures 1-5 are examined, it is seen that as the rate of addition of walnut shell ash and cone ash in the compounds increases, the fillings are distributed heterogeneously in the main matrix and grouped by agglomerating among themselves. It seems that the hollow structure has increased with the increase in the amount of CA and WSA. It was observed that the grain sizes of the fillers added to the compounds are not homogeneous and their geometric shapes are different from each other. In Figure 6, the results of the clumping number and density analysis are presented graphically with the help of the image processing software of the SEM images of the compounds.

Figure 6. Clumping analysis results with the help of image processing software developed SEM images of the compounds

It has been understood from the results of image processing software developed that the increase in filling rates in the compounds increases the number and density of recovery in the compounds. The highest clumping density occurred i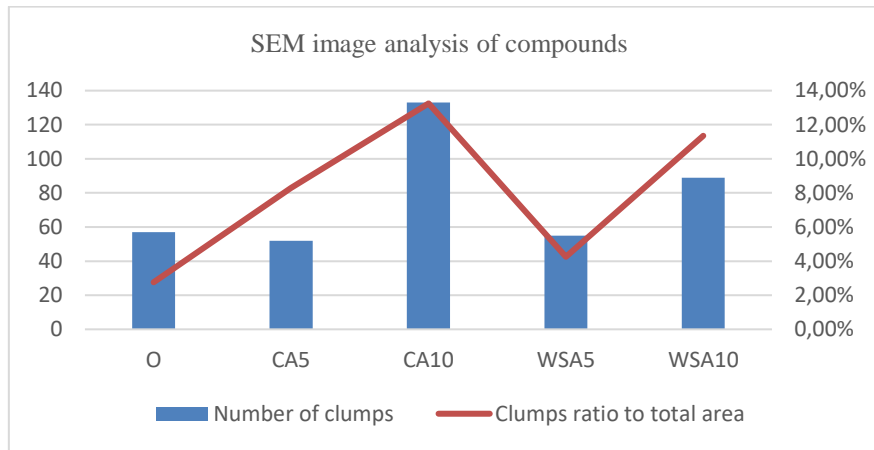n the compound CA10. The lump rate in CA10 compound increased by 583.7% compared to that of compound O. The lowest aggregation amount was observed in 5% walnut shell ash added compound, namely WSA5 compound (153.98%). It is understood from the graph that there is an increase in other compounds compared to the O compound. It can be understood from the results that the clumping density of SEM images also increases. Although the number of agglomeration seems to be high in unfilled material, the fact that the percentage rate in the material is low indicating that the area covered by the agglomeration is low. In similar studies, it was found that with the increasing amount of fillers, especially recycling materials used in the compounds may cause lumps in the rubber matrix [16, 24].

4. Conclusions

With the developed image processing software, in this study, the aggregation density of SEM images was determined by visually trying to predict the agglomeration density of SEM images before detecting clumps on SEM images. Thanks to this method, more accurate information has been revealed based on numerical data. It was observed that lumps increased with an increasing amount of filling added to the compounds. It was determined that the number of clumping fell. The utility of the method presented in this study has been proved in similar studies.

Declaration

The author(s) declared no potential conflicts of interest with respect to the research, authorship, and/or publication of this article. The author(s) also declared that this article is original, was prepared in accordance with international publication and research ethics, and ethical committee permission or any special permission is not required.

References

1. Bülbül, Ş., M. Yaşar, and N. Akçakale, *Effect of changing of filling materials in NR-SBR type elastomer-based rubber materials on mechanical properties.* Polymer(Korea), 2014. **38**(5): p. 664-670.

2. Hedayatollah, S.G. and J.A. Azam, N*anocomposites based on natural rubber, organic nano clay and nano-calcium carbonate: a study on the structure, cure behavior, static and dynamic-mechanical properties.* Applied Clay Science, 2016. **119**: p. 348–357.

3. De, D., P.K. Panda, M. Roy and S. Bhunia, *Reinforcing Effect of Reclaim Rubber on Natural Rubber/Polybutadiene Rubber Blends.* Materials and Design, 2013. **46**: p. 142-150.

4. Malas, A., P. Pal and C.K. Das, *Effect of expanded graphite and modified graphite flakes and the physical and thermo-mechanical properties of Styrene Butadiene Rubber/Polybutadiene Rubber (SBR/BR) blends.* Materials and Design, 2014. **55,** p. 664-673.

5. Mohan, T.P., J. Kuriakose and K. Kanny, *Water up Take and mechanical properties of Natural Rubber–Styrene Butadine Rubber (NR-SBR) – nanoclay composites.* J. of Industrial and Engineering Chemistry, 2012. **18:** p. 979-985.

6. Akçakale, N. and Ş. Bülbül, *The effect of mica powder and wollastonit fillings on the mechanical properties of NR/SBR type elastomer compounds.* J. Rubb. Res., 2017. p. **20**(3): p.157-167.

7. Furtado, C.R.G., J.L. Leblanc and R.C.R. Nunes, *Fatigue resistance of mica-carbon black Styrene Butadiene Rubber (SBR) compounds.* Eur. Polymer J., 1999. **35**: p. 1319–1325.

8. Furtado, C.R.G., J.L. Leblanc and R.C.R. Nunes, *Mica as additional filler in SBR-Silica compounds.* Eur. Polymer J., 2000. **36:** p.1717–1723.

9. Saramolee, P., K. Sahakaro, N. Lopattananon, .K. and J.W.M. Noordermeer, *Compatibilisation of silica-filled natural rubber compounds by functionalised low molecular weight polymer.* J. of Rubber Research, 2016. **19**(1): p. 28–42.

10. Alfaro, E.F., D.B. Dias and L.G.A. Silva, *The study of ionizing radiation effects on polypropylene and rice husk ash composite.* Radiation Physics and Chemistry, 2013. **84**: p.163–165.

11. Kim, S.M. and K.J. Kim, *Effects of accelerators on the vulcanization properties of silica vs. carbon black filled*

natural rubber compounds. Polymer (Korea), 2013. **37**(3): p. 269-275.

12. Ge, X., M.C. Le and U.R. Cho, *Fabrication of EPDM rubber/organo-bentonite composites, influence of hydrochloric acid on the characteristics of modified bentonite and final products*. Polymer (Korea), 2014. **38**(1): p. 62-68.

13. Prasertsri, S., F. Lagarde, N., Rattanasom, C. Sirisinha and P. Daniel, *Raman spectroscopy and Thermal Analysis of Gum and Silica-Filled NR/SBR Blends Prepared from Latex System*. Polymer Testing, 2013. **32**: 852–861.

14. Yan, G., Z. Junchi, Y. Xin, H. Dongli, X. Meimei and Z. Liqun, *Preparation and performance of silica/sbr master batches with high silica loading by latex compounding method*. Composites Part B, 2016. **85**: p. 130–139.

15. Bülbül, Ş. *The effect of various inorganic and organic fillers on the mechanical properties of NR-SBR type elastomer materials* [dissertation] Karabük (TR): Karabük University; 2014.

16. Bülbül, Ş. *Doğal atık malzemelerle yeni NBR bazli bileşiklerin hazirlanmasi ve karakterizasyonu.* BSEU Journal of Science, 2019. **6** (Prof. Dr. Fuat SEZGİN Bilim Yılı Özel Sayısı) p. 42-49.

17. Sabzekar, M., M.P. Chenar, G. Zohuri, and S.M. Mortazavi, *Investigation of mechanical, thermal, and morphological properties of EPDM compounds containing reclaimed rubber*. Rubber Chemistry and Technology, 2017. **90:** p. 765–776.

18. Sastry, S.S., B. Rao, K.B. Mahalakshmi, K. MALLİKA, C.N. Rao and, H.S. Tiong, *Image analysis studies for phase transitions of ferroelectric liquid crystals*. ISRN Condensed Matter Physics, 2012, p. 1-8.

19. Sudheer, K. P. and R.K. Panda, *Digital image processing for determining drop sizes from irrigation spray nozzles.* Agricultural Water Management, 2000. p. **45**(2): 159-167.

20. Sastry, S.S., M. Sailaja, S. Lakshminarayana and S.T. Ha, *Computation of Liquid Crystal Display Device Parameters Through Image Analysis,* Int. Journal of Engineering Research and Application, 2017. **7**(7): p. 24-31.

21. Fan, H., F. Xie, Y. Li, Z. Jiang, and J. Liu, *Automatic segmentation of dermoscopy images using saliency combined with Otsu threshold.* Computers in biology and Medicine, 2017. **85**: p.75-85.

22. Flegler, S.L., J.W. Heckman and K.L. Klomparens, *Scanning and transmission electron microscopy*. England: Oxford University Press, ISBN 0-19-510751-9, 1993.

23. Sezgin M. and B. Sankur, *Survey over image thresholding techniques and quantitative performance evaluation*. Journal of Electronic Imaging, 2004. **13**(1): 146–165.

24. N. Akcakale, *Effects of carburized rice husk powders on physical properties of elastomer based materials*, KGK-Kautschuk Gummi Kunststoffe, (2017) **70** (10-17): p. 49–54.

Research Article

Taguchi method for investigation of the effect of TBC coatings on NiCr bond-coated diesel engine on exhaust gas emissions

Serkan Özel [a],* ID, Erdinç Vural [b] ID and Murat Binici [a] ID

[a] *Bitlis Eren University, Bitlis, 13000, Turkey*
[b] *Aydın Adnan Menderes University, Aydın, 09000, Turkey*

ABSTRACT

The NiCr bond coated piston and valve surfaces were coated with Cr_2O_3, Cr_2O_3 + 50% Al_2O_3, Cr_2O_3 + 75% Al_2O_3 powders by thermal barrier coating (TBC). The influence of the coating layers on CO, CO_2, HC and NOx was examined both statistically and experimentally. The statistical investigation was carried out by using Taguchi analysis. According to the experimental test results obtained at different engine speeds, the sample with the highest CO_2 value was found at 2600 rpm in the Cr_2O_3 + 75% Al_2O_3 coated diesel engine and the sample with the lowest CO value was found at 2600 rpm in the Cr_2O_3 + 75% Al_2O_3 coated diesel engine. Also, the sample with the lowest NO_x value was found at 1400 rpm in the standard diesel engine and the sample with the lowest HC value was found at 2600 rpm in the Cr_2O_3 + 75% Al_2O_3 coated diesel engine. Experimental results were analyzed by Taguchi optimization method according to L16 (4^2) orthogonal array. According to the statistical results obtained from ANOVA test, factor levels affecting the exhaust emission values best were found. In general, better emission values have been determined in diesel engines with bond coated ceramic layers.

1. Introduction

In internal combustion engines, deformation and chemical wear on the piston surfaces decrease the service life of the material after a while, resulting in a gradual decrease in performance, an increase in fuel consumption and an increase in emission values. Preventing these surface deformations, which are likely to occur, can be achieved by preventing the high temperature, pressure and chemical wear (corrosion) occurring during the combustion event from directly touching the main material surface. One of the most suitable methods to provide this protection is to cover the surface of the material with a ceramic material, that is, to create a thermal and physical interface on the main material. By coating the combustion chamber elements with ceramic material, temperatures in the cylinders rise and play a vital role in reducing emissions while improving engine efficiency, heat emission rate, specific fuel consumption [1-3].

The combustion chamber is the place where power and energy occur in internal combustion engines. Fuel burning in the combustion chamber causes sudden temperature and pressure changes in the cylinders. Piston is the most exposed part to these suddenly changing loads. During that the engine is operating, the piston's pressure can get to 8 MPa, while the gas temperature is up to 2500 ^0C [4].

Thermal barrier coatings (TBCs) are implemented on the surface of these parts to increase the reliability, durability and engine performance of metal parts operating in hot regions in advanced engines [5].

There are some benefits of utilizing TBC in engines working with diesel fuel. Firstly, heat can be kept inside the engine. Secondly, thermal shocks and fatigue can be prevented. Thirdly, it can decrease hydrocarbon and carbon monoxide emission levels. Moreover, in the case of using low quality fuels, TBC engines have the ability to retain heat within the engine although fuel quality is low [6].

Taguchi analysis is a successful method used in the solution of optimization problems with less cost and fewer experiments. Applying the analysis, the quantity of tests is significantly reduced, thus saving time and money spent on experiments. Moreover, the Taguchi method helps the development of high-quality processes and products in every respect. It has minimum sensitivity against uncontrollable factors that may occur in products and production conditions. For this reason, the costs that may arise due to the necessary tolerances can be reduced and the quality process can have a new understanding with the help of the Taguchi loss function [7-9]. Taguchi analysis has been previously applied in various studies regarding the design of experiments [10-13].

In this work, the bond-coated (NiCr) piston and valve surfaces in the internal combustion engine were coated with Cr_2O_3, $Cr_2O_3 + 50\% Al_2O_3$, $Cr_2O_3 + 75\% Al_2O_3$ powders by thermal barrier coating (TBC) method, and the influence of the coating layer on CO, CO_2, HC and NOx emissions was optimized by the Taguchi analysis.

2. Material and Method

2.1 Coating Materials

Coating materials and NiCr bond-coated layer were covered with plasma spray method on the piston and valve. The ceramic coating powders and substrates used are given in Table 1. To compare and better understand the results of these three different ceramic powders, measurements were also obtained from a standard diesel engine.

2.2 Engine Tests Method

The combustion chamber elements (piston and valve) of the single-cylinder, four-stroke air-cooled diesel engine were coated with NiCr bond-coated layer and Cr_2O_3, $Cr_2O_3 + 50\% Al_2O_3$, $Cr_2O_3 + 75\% Al_2O_3$ powders using the plasma spray coating method. Emission measurement values of standard engine and coated engines were measured with the test setup shown in Figure 1 in the experimental setup. The test engine's technical characteristics used in the experimental setup are given in Table 2.

There was not any modification to the original injection system of the test engine, the engine was operated at the original injection advance of 31 CA and the original injection pressure of 200 bar. The engine was run for 10 minutes for engine test measurements and the engine was brought to operating temperature. Engine test measurements were performed at 4 different engine speeds (1400rpm, 2000rpm, 2600rpm and 3200rpm) at the engine full throttle position.

Table 1. Coating materials used on NiCr bond-coated valve and piston surfaces

Coating Material	Substrates
Standard Engine	
Cr_2O_3	Valve and Piston
$Cr_2O_3 + 50\% Al_2O_3$	
$Cr_2O_3 + 75\% Al_2O_3$	

1. Diesel Test Engine   3. Diesel Fuel Tank   5. Control Panel Recording Computer NF Software
2. Dynamometer   4. Dynamometer Control Panel   6. Exhaust Gas Analyzer
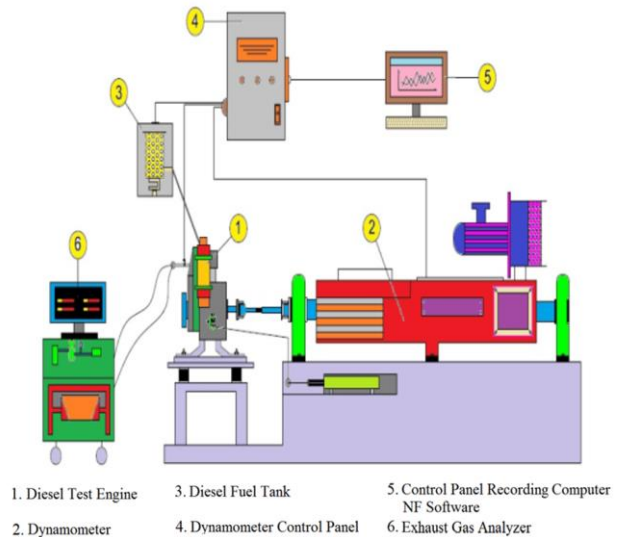
Figure 1. Schematic representation of the test setup.

Table 2. The test engine's technical features.

Features	Values
Number of Cylinders	1
Cylinder diameter (mm)	78
Stroke (mm)	62
Cylinder Volume (cc)	296
Compression Ratio	20/1
Maximum power (kW)	4.0
Maximum Engine Speed (rpm)	3600
Tank Volume (L)	3.5
Fuel consumption ratio (g (ml) /kW.h)	3600rpm:285(339)
Crank Angle (CA)	31^0
Injection Pressure (bar)	200

2.3 Statistical Method

The Taguchi analysis is beneficial way of the design of experiments. The results of experimental studies can be achieved utilizing the signal to noise ratio (S/N) [14, 15]. Concepts that can be used to analyze data in a Taguchi study;

- Larger is better
- Nominal is better
- Smaller is better

The information of each parameter used in the experiment can be accessed by performing variance analysis (ANOVA) [14].

This analysis uses L_{16} (4^2) orthogonal array to make the design of the experiments robust. Parameters that might affect the gas emissions are ''engine speed'' and ''coating material''. Table 3 gives the control parameters and levels of 1400 rpm, 2000 rpm, 2600 rpm and 3200 rpm engine speeds with standard diesel engine, NiCr bond-coated diesel engines coated with Cr_2O_3, Cr_2O_3+ 50% Al_2O_3 ve Cr_2O_3+ 75% Al_2O_3 powders.

The models used in the experimental stage of this study are "smaller is better" for CO, HC and NOx emissions while it is "larger is better" for CO_2. The reason is that CO, HC, and NOx emissions are expected to decrease during the engine working, while CO_2 is to increase. Signal noise (S/N) ratios is found applying the formulas below.

''Larger is better'': $S/N = -10 \ x \ log_{10} \left(\frac{1}{n}\sum_{i-1}^{n}\frac{1}{Y_i^2}\right)$ (1)

''Nominal is better'': $S/N = -10 \ x \ log_{10} (s^2)$ (2)

''Smaller is better'': $S/N = -10 \ x \ log_{10} \left(\frac{1}{n}\sum_{i-1}^{n}Y_i^2\right)$ (3)

S/N: Signal to noise ratio, Y_i : Result of experiment, i = The quantity of repeats

3. Experimental and Statistical Findings

3.1 Analysis of Test Outcomes

In Figure 2, graphs of the rates of CO, CO_2, HC and NOx gases in different speeds of diesel engines coated with different powders and uncoated diesel engine are given.

In Figure 2.a., Changes in carbon monoxide (CO) value are given according to the engine speed obtained from experimental data. When the graphic is analyzed, it is seen that the CO values obtained from the standard diesel engine are at higher rates than all the coated engines. The engine with the lowest CO emission is observed to be Cr_2O_3 + 75% Al_2O_3 coated engine. Another remarkable factor in this graph is that while all the speeds, there is a downward release of CO gas, the rate of CO increases in all engines at 3200 rpm. This may be the reason for the high frequency of closing of the valves at high speeds and the insufficient amount of air entering the engine [16].

Table 3. Levels and control parameters.

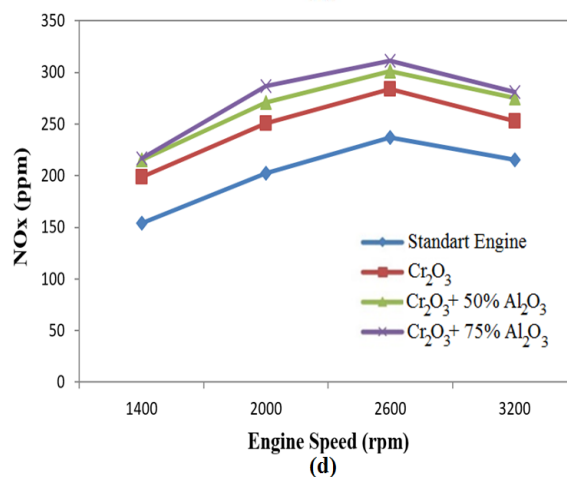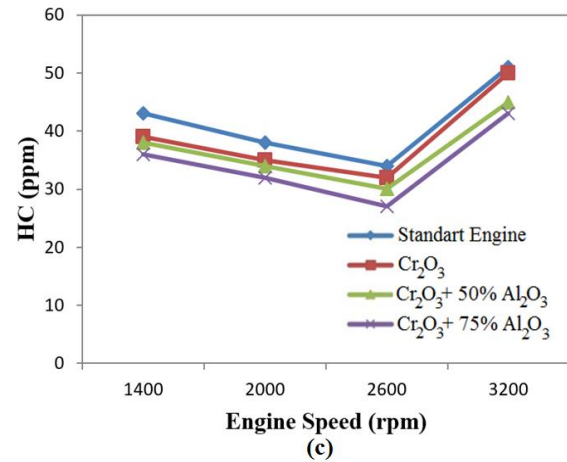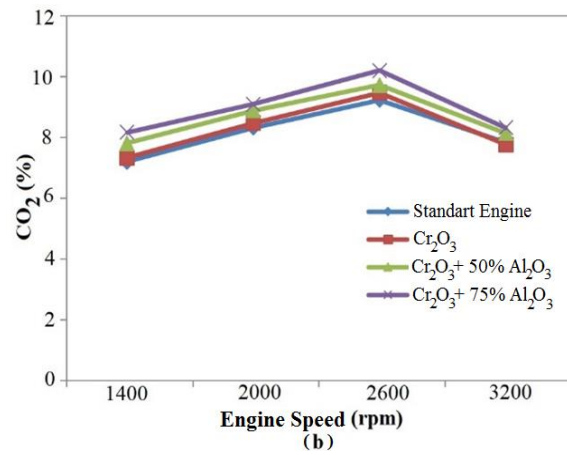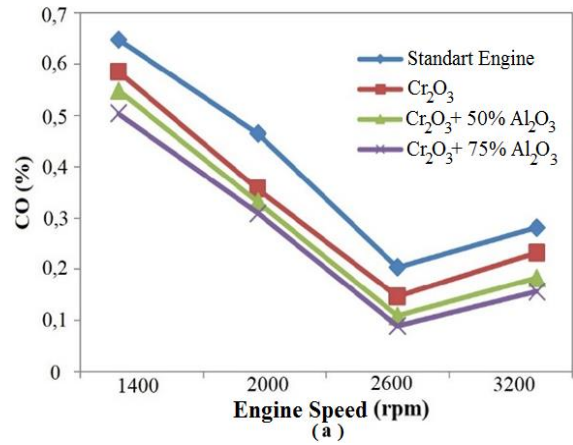| Control parameters	Level 1	Level 2	Level 3	Level 4
Coating Material	Standard engine	Cr_2O_3	Cr_2O_3+ 50% Al_2O_3	Cr_2O_3+ 75% Al_2O_3
Engine Speed	1400 rpm	2000 rpm	2600 rpm	3200 rpm

Figure 2. Exhaust emission values

In Figure 2.b., changes in carbon dioxide (CO_2) value are given according to the engine speed obtained from experimental data. In this graph, it is seen that CO_2 emission has the highest value in engines coated with Cr_2O_3 + 75% Al_2O_3 powders and the lowest value in standard diesel engines. It is also seen that CO_2 emissions increase at 1400 rpm, 2000 rpm and 2600 rpm speeds, but CO_2 rate decreases from 2600 rpm to 3200 rpm. When the speed is low, the CO_2 ratio is lower than the fuel, but when the speed is increased, the momentum increases to the maximum point and improves combustion. In addition, the increase in the amount of fuel and the reduction of the combustion time due to the increase in the engine speed at higher revs can not fully perform the combustion process and this causes the CO_2 emission to decrease [17-18].

A striking situation revealed by both the CO and CO_2 graphs is that the proportions of these gases are almost opposite, meaning that CO_2 emissions are decreasing while CO_2 emissions are decreasing or vice versa [19-20].

In Figure 2.c, the graph shows the change of Hydrocarbon (HC) emissions according to engine speed. It is the main component of hydrogen and carbon fuels. Hydrocarbon emissions are the amount of unburned fuel as a result of partial combustion in the combustion chamber [21]. With ceramic coated engines, there has been a decrease in HC emissions in all engine speeds compared to the standard engine. The main source of HC formation is around the reaction zone where the mixture in the combustion chamber is too poor to ignite. It is thought that, with the increase of the end–burn temperature in coated engines, there is a better combustion in the cylinder and it causes a decrease in HC emissions, as well as the decrease in ignition delay time with the increase in the temperature of the cylinder, and the shortening of the ignition delay, causing the fuel to emerge with the sudden combustion of the fuel.

In Figure 2.d, the graph shows the change of Nitrogen Oxide (NOx) emissions by engine speed. Factors affecting NOx emission in diesel engines are end of combustion temperature, reaction temperature, heat dissipation rate, stoichiometric combustion, ignition delay time, mixture from previous engine cycles and excess oxygen rate. The increase of NOx emission depends on the temperatures inside the cylinder and increases in direct proportion to the temperature increase. With the use of coated pistons, the end of combustion temperature obtained in the cylinder increases. Because the heat generated at the end of combustion by coating the piston surface remains in the cylinder. Thus, the temperature value at the end of combustion increases partially. This situation causes a good combustion start

with the increase of the temperature of the gas in the cylinder in each cycle.

Since the thermal conductivity coefficients of Cr_2O_3 and Al_2O_3 materials are lower than that of AlSi, which is the coating material of the standard combustion chamber of the engine, the temperatures inside the cylinder are trapped, and hence, the end-burn temperature in the cylinder increases [22]. All ceramic coated engines show higher NOx emissions than the standard engine. Ceramic-coated engines create a better thermal barrier coating, thereby raising the temperature inside the cylinder, thus increasing NOx emissions.

3.2 Statistical Results and Taguchi Analysis

The experimental results mentioned in the previous section will also be interpreted in this section with the Taguchi and ANOVA test results.

In this part of the study, emission values of CO, CO_2, HC and NOx exhaust gases will be analyzed. It is desired that the ratios of CO, HC and NOx are minimum since these emissions are toxic and dangerous. Although CO_2 emission is actually dangerous, it is desired to be maximum in this study. The reason for this is that, as mentioned in section 3.1, CO_2 has the opposite action with CO, HC, and NOx. During the experimental design phase, CO, HC, and NOx were evaluated as "smaller is better" but CO_2 as "larger is better".

3.2.1 Carbon monoxide (CO)

Table 4 gives the S/N ratios of CO obtained by using control parameters. These values are expressed graphically in Figure 3. Also, in Table 5, there is a statistical analysis (ANOVA) of S/N ratios obtained as a result of Taguchi analysis using experimental results.

The two parameters are statistically significant on CO values since P values in Table 5 are less than 0.05.

When the values given in Table 4 and Figure 3 are evaluated together, coating material parameter gives S/N ratios minimizing CO ratios in Level 4 and engine speed parameter Level 3.

3.2.2 Carbon dioxide (CO_2)

S/N ratios of CO_2 are given in Table 6. In Figure 4, there is a graphic obtained using these values. In Table 7, there is a statistical analysis (ANOVA) of S/N ratios obtained as a result of the Taguchi analysis using experimental results.

According to the statistical data in Table 7, it can be concluded that independent parameters are statistically significant in explaining CO_2 values since the P value is less than 0.05.

When the values given in Table 6 and Figure 4 are evaluated together, it is seen that the coating material

parameter at the 4th level and the engine speed parameter at the 3rd level make the CO_2 ratios maximum.

Table 4. CO Signal to Noise ratios.

	CO			
Control Parameters	Level 1	Level 2	Level 3	Level 4
Coating Material	7,8	9,223	10,188	10,889*
Engine Speed	4,714	7,962	13,965*	11,459

* Levels that minimize results

Table 5. Variance analysis of CO S/N ratios (ANOVA)

Source	DF	Seq SS	Adj SS	Adj MS	F	P
Coating Material	3	21,458	21,458	7,1526	29,92	0
Engine Speed	3	196,18	196,18	65,393	273,6	0
Residual Error	9	2,151	2,151	0,2390		
Total	15	219,79				

Table 6. CO_2 Signal to Noise ratios.

	CO_2			
Control Parameters	Level 1	Level 2	Level 3	Level 4
Coating Material	7,8	9,223	10,188	10,889*
Engine Speed	4,714	7,962	13,965*	11,459

Table 7. Variance analysis of CO_2 S/N ratios (ANOVA)

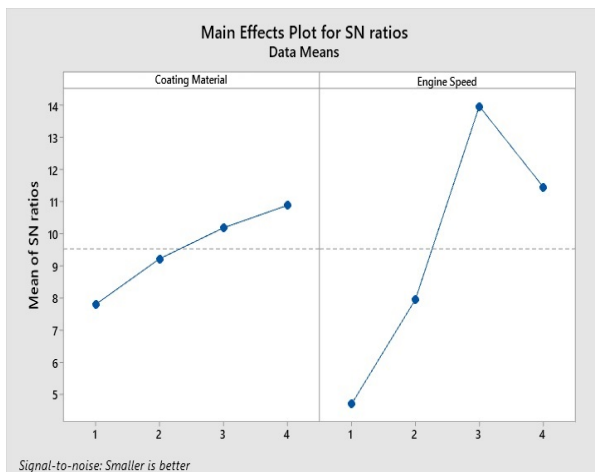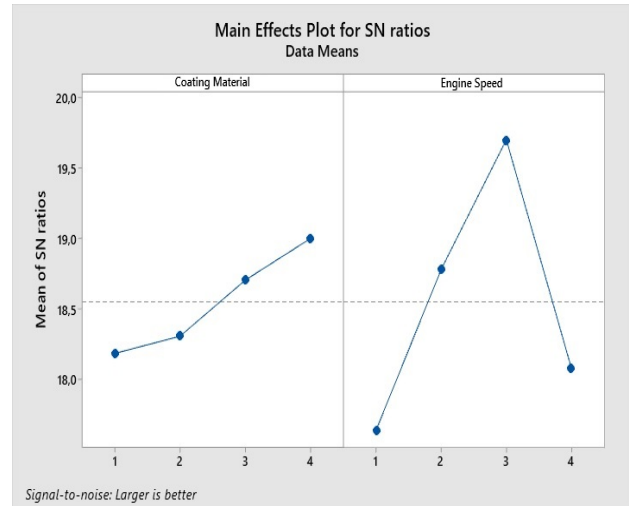| Source	DF	Seq SS	Adj SS	Adj MS	F	P
Coating Material	3	21,458	21,458	7,1526	29,92	0
Engine Speed	3	196,179	196,18	65,393	273,6	0
Residual Error	9	2,151	2,151	0,2390		
Total	15	219,788				

Figure 3. CO Signal to Noise graphic

Figure 4. CO_2 Signal to Noise graphic

3.2.3 Nitrogen Oxide (NOx)

Table 8 gives the Signal / Noise (S/N) ratios of NOx obtained using the control parameters mentioned earlier. The values in this table represent the values that give the effect of test parameters on the results. In addition, these values are reflected graphically in Figure 5 to show the effects of coating material and engine speeds on NOx.

These parameters are statistically significant on NOx values according to the statistical results (P <0.05) in Table 9 obtained by using the independent coating materials and engine speeds.

Table 8. NOx Signal to Noise ratios

	NOx			
Control Parameters	Level 1	Level 2	Level 3	Level 4
Coating Material	**-46.00***	-47.77	-48.42	-48.68
Engine Speed	**-45.78***	-47.98	-49.00	-48.12

* Levels that minimize results

Table 9. Variance analysis of NOx S/N ratios (ANOVA)

Source	DF	Seq SS	Adj SS	Adj MS	F	P
Coating Material	3	17,4612	17,4612	5,82039	138,5	0
Engine Speed	3	22,5361	22,5361	7,51205	178,75	0
Residual Error	9	0,3782	0,3782	0,04203		
Total	15	40,3755				

S / N ratios of NOx are given in Table 8, and they are also graphical in Figure 5. Accordingly, both Coating Material and Engine Speed parameters have the highest values in Level 1. The lowest values are at Level 4 in Coating Material parameter, while at Level 3 in Engine Speed parameter.

3.2.4 Hydrocarbon (HC)

In this section, S / N ratios of HC gas are given in Table 10 and Figure 6. In Table 11, there are statistical data of Coating Material and Engine Speed parameters on HC gas ratios.

When Table 11 is examined, it is seen that both Coating Material data and Engine Speed data are statistically significant on HC data (P <0.05).

Based on the data in Table 10 and the graph in Figure 6, it is seen that the values that minimize the results are at Level 4 of the Coating Material parameter and Level 3 of the Engine Speed parameter.

Table 10. HC Signal to Noise ratios

Control Parameters	HC			
	Level 1	Level 2	Level 3	Level 4
Coating Material	-32,26	-31,70	-31,21	**-30,63***
Engine Speed	-31,80	-30,80	**-29,73***	-33,47

* Levels that minimize results

Table 11. Variance analysis of HC S/N ratios (ANOVA)

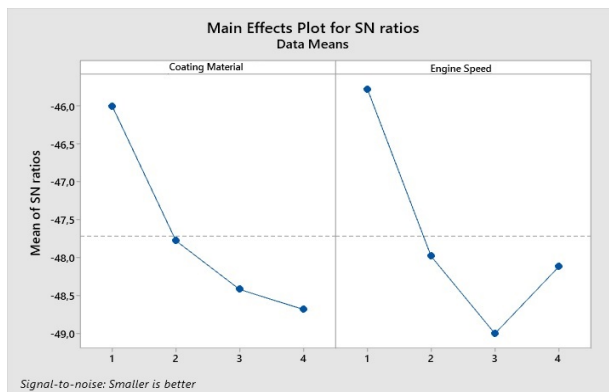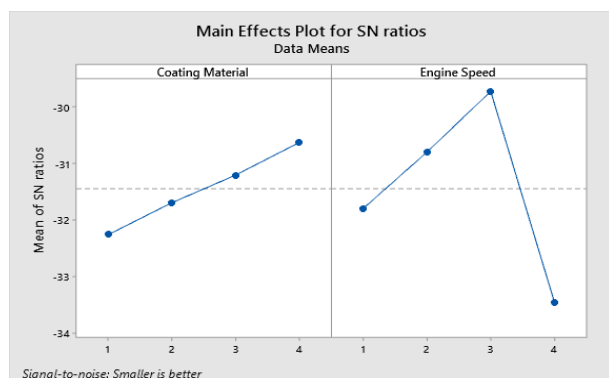| Source	DF	Seq SS	Adj SS	Adj MS	F	P
Coating Material	3	5,7913	5,7913	1,9304	50,47	0
Engine Speed	3	30,3296	30,3296	10,1099	264,29	0
Residual Error	9	0,3443	0,3443	0,0383		
Total	15	36,4652				

Figure 5. NOx Signal to Noise graphic

Figure 6. HC Signal to Noise graphic

4. Conclusion

The following results were obtained by looking at the experimental, statistical and Taguchi analysis results.

- While carbon monoxide (CO) and hydrocarbon (HC) emissions are lower in Cr_2O_3, Cr_2O_3 + 50% Al_2O_3 and Cr_2O_3 + 75% Al_2O_3 ceramic coated diesel engines compared to standard diesel engine, nitrogen oxide (NOx) emission is lower in standard diesel engine compared to the other coated diesel engines.
- Carbon dioxide (CO_2) emission is higher in Cr_2O_3, Cr_2O_3 + 50% Al_2O_3 ve Cr_2O_3 + 75% Al_2O_3 ceramic coated diesel engines compared to standard diesel engines.
- The control parameters give statistically significant results (P <0.05) on CO, CO_2, HC and NO_x results.
- While the Taguchi analysis of CO, CO_2 and HC gives the best results in Cr_2O_3 + 75% Al_2O_3 coated diesel engine at 2600 rpm, that of NO_x is best in standard diesel engine at the 1400 rpm.
- According to the experimental and taguchi analyses, CO, CO_2 and HC emissions in ceramic coated diesel engines with NiCr bond-coated layer have better performance than standard diesel engine although standard engine is the best for NO_x emission.

Declaration

The author(s) declared no potential conflicts of interest with respect to the research, authorship, and/or publication of this article. The author(s) also declared that this article is original, was prepared in accordance with international publication and research ethics, and ethical committee permission or any special permission is not required.

Acknowledgment

References

1. Masera, K., A.K. Hossain, *Biofuels and thermal barrier: A review on compression ignition engine performance, combustion and exhaust gas emission*, Journal of the Energy Institute, 2019. **92**(3): p. 783-801.
2. Karthikayan, S., S. Ganesan, P. Vasanthakumar, G. Sankaranarayanan, M. Dinakar., *Innovative Research Trends in the Application of Thermal Barrier Metal Coating in Internal Combustion Engines*, Materials Today: Proceedings, 2017. **4**(8): p. 9004-9012.

3. Çolak N.Y. ve D. Şimşek, *Emisyon Kontrol Uygulamalarında Saf Ponza Taşı Kullanılabilirliğini Deneysel Olarak Araştırılması*, Bitlis Eren Üniversitesi Fen Bilimleri Dergisi, 2017. **6**(1): p. 31-41.

4. Heywood, J.B., *Internal Combustion Engine Fundamentals. 1988*, USA:McGraw-Hill Education.

5. Zhou, H., D. Yi, Z. Yu, L. Xiao, *Preparation and thermophysical properties of CeO2 doped La2Zr2O7 ceramic for thermal barrier coatings*, Journal of Alloys Compounds, 2007. **438**: p.217–221.

6. Özel, S., E. Vural, M. Binici, *Optimization of effect of thermal barrier coating (TBC) on diesel engine torque by taguchi method*, in FCE2019: Antalya. p. 393-399.

7. Şirin, E., Ş. Şirin, Y. Turgut, and İ. Korkut, *Optimization of surface roughness using the Taguchi method in milling of AISI D2 cold work tool steel*, Düzce Üniversitesi Bilim ve Teknoloji Dergisi, 2015. **3**(1): p. 132-144.

8. Naik, A.B. and A. C. Reddy, *Optimization of tensile strength in TIG welding using the Taguchi method and analysis of variance (ANOVA)*, Thermal Science and Engineering Progress, 2018. **8**: p. 327-339.

9. Özel, S., H. Turhan, and E. Gönel, *Optimization of effect of production parameters on wear resistance of coated layer on the surface of copper alloy by taguchi method*, Internation Journal of Advance Research and Innovative Ideas in Education, 2017. **3**(4): p. 1517-1523.

10. Park, I. C. and S. J. Kim, *Cavitation erosion behavior in seawater of electroless Ni-P coating and process optimization using Taguchi method*, Applied Surface Science, 2018. **477**: p. 37-43.

11. Tabaraki, R. and A. Nateghi, *Application of taguchi L16 orthogonal array design to optimize hydrazine biosorption by Sargassum ilicifolium*, Environmental Progress & Sustainable Energy, 2016. **35**(5): p. 1450-1457.

12. Moganapriya, C., R. Rajasekar, K. Ponappa, R. Venkatesh and S. Jerome, *Influence of coating material and cutting parameters on surface roughness and material removal rate in turning process using taguchi method*, Materials Today: Proceedings, 2018. **5** (2): p. 8532-8538.

13. Trivedi, H.K. and D.V. Bhatt, *An experimental investigation on friction and wear test parameters of cylinder liner and piston ring pair using Taguchi technique*, Industrial Lubrication and Tribology, 2018. **70**(9): p. 1721-1728.

14. Montgomery, D.C., *Design and Analysis of Experiments. 2017*, USA: John Wiley & Sons, Inc.

15. Maghsoodloo, S., G. Ozdemir, V. Jordan, and C. H. Huang, *Strengths and limitations of Taguchi's contributions to quality, manufacturing, and process engineering*, Journal of Manufacturing systems, 2004. **23**(2): p. 73-126.

16. Ciniviz, M., *Türboşarjlı bir dizel motorunun yanma odasi yüzeylerinin Y2O3 – ZrO2 ile kaplanmasının performans ve emisyonlara etkileri*, in *Mechanical Engineering* 2005, Selçuk University:Turkey.

17. Vural, E., and S. Özel, *Dizel Bir Motorda Al2O3 İlaveli Cr2O3 Termal Bariyer Kaplamaların Egzoz Emisyonlarına Etkisi*, Bitlis Eren Üniversitesi Fen Bilimleri Dergisi, 2019. **8**(1): p. 308-318.

18. Akçay M. And S. Özer, *Experimental investigation on performance and emission characteristics of a CI diesel engine fueled with fusel oil/diesel fuel blends*, Energy Sources, Part A: Recovery, Utilization, and Environmental Effects, 2019. Published online, in press.

19. Vural, E., S. Özel, *İçten yanmalı dizel motorda Cr2O3 termal bariyer kaplamaların motor performansı üzerine etkisi*, in INCOS2018: Karabük. p. 374-378.

20. Celik, M. B., *Experimental determination of suitable ethanol–gasoline blend rate at high compression ratio for gasoline engine*, Applied Thermal Engineering, 2008. **28**(5-6): p. 396-404.

21. Goga, G., B. S. Chauhan, S. K. Mahla, H. M. Cho, *Performance and emission characteristics of diesel engine fueled with rice bran biodiesel and n-butanol*, Energy Reports, 2019. **5**: p. 78–83.

22. Vural E. And S. Ozer, *Thermal Analysis of a Piston Coated with SiC and MgOZrO2 Thermal Barrier Materials,* International Journal of Scientific and Technological Research, 2015. **1**(7): p. 43-51.

Research Article

Application of reverse engineering approach on a damaged mechanical part

Özgür Verim [a,*] [iD] *and Mehmet Yumurtacı* [b] [iD]

[a]*Afyon Kocatepe University, Faculty of Technology, Department of Mechanical Engineering, Afyonkarahisar and 03200, Turkey*
[b]*Afyon Kocatepe University, Faculty of Technology, Department of Electrics and Electronics Engineering, Afyonkarahisar and 03200, Turkey*

ARTICLE INFO	ABSTRACT
	Reverse engineering methods are important for remodeling or measuring damaged or non-damaged parts. Reverse engineering also enables the design of complex components, reducing actual product production time and prototype production time. With this method, damaged gear wheels can be modeled in a short time due to the regular geometry and symmetrical properties of the teeth and it is real models can be produced. In this study, the damaged motor cam gear was scanned with a three dimensional (3D) scanner and a mesh model was formed. Then, solid model of part was created and genuine prototype was produced with 3D printer. The deviations of geometric dimensions between the mesh model and the solid model were analyzed and the levels of convergence were determined. The three-dimensional prototyping method provides great convenience for the designer due to it gives quick feedback in product development process. At the end of the study, geometric values between solid model and prototype model were compared and deviations from actual value were determined.

1. Introduction

Reverse engineering is a field that is continuously expanding in recent years and interested in computer-aided geometric design [1]. It is used in many fields of industry to create geometric models of objects that do not have existing models. Reverse engineering is also used in engineering, medical sciences, restoration processes for the conservation of cultural heritage, and many other fields [1]. When engineering applications are taken into consideration, the main purpose of the reverse engineering is to create a 3D parametric solid model, which is best suited to the original of the object, by using raw data obtained from a 3D scanner. As another definition, reverse engineering is defined as a method of creating data of engineering design and documentation from existing parts and their assemblies in the fields of mechanical engineering and industrial production [2]. Whereas in the traditional engineering approach, engineering concepts and models are converted into real parts [3], in the reverse engineering approach, real parts are converted into engineering concepts and models [4]. In the

field of mechanical engineering, the reverse engineering allows the re-creation of surface or geometric data of an existing part by using contact or non-contact measuring devices. With some exceptions, most of the techniques available in reverse engineering literature have specific steps [1, 5-7]. These are scanning the part with a 3D scanner, data collection, processing of original data, segmentation of point clouds/meshes, classification of regions defined in the segmentation step, generation of analytical surfaces and properties applied to generally classified surfaces, finishing operations (e.g. joining adjacent surfaces), reconstruction of the computer-aided design (CAD) model, and prototype creation (Figure 1). This framework is also used by commercial software systems where each step is performed using a specific tool or function.

Over time, automatic mesh algorithms used for 3D surfaces have become valuable tools in analysis and design processes. After the algorithm is applied, the resulting elements are used as input to the automatic triangle or quadrilateral mesh algorithm.

* Corresponding author. Tel.: +90 272 218 2510 - 2546
E-mail addresses: ozgurverim@hotmail.com *(Ö. Verim),* mehmetyumurtaci@aku.edu.tr *(M. Yumurtacı)*
ORCID: 0000-0002-1575-2630 *(Ö. Verim),* 0000-0001-8528-9672 *(M. Yumurtacı)*
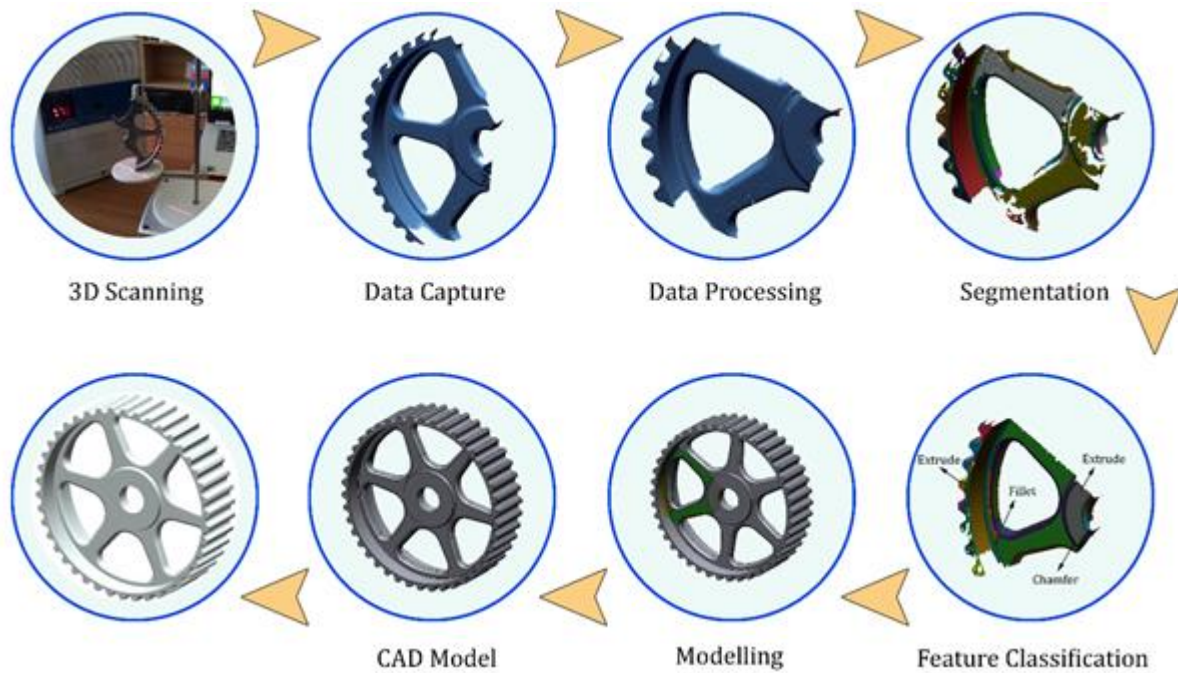
Figure 1. Flow chart of general reverse engineering approach prototype

Since triangular mesh algorithms have simple, easy and provable mathematical features, they are widely used in the literature. Despite this, many researchers prefer quadrilateral elements, drawing attention to their superior features [8]. Simplifying quadrilateral networks create additional challenges. Because quadrilateral elements are less compatible and more sensitive structures than triangles, simplifying them leads to additional challenges [9]. In industrial applications, free-form surfaces of models are often represented by the B-spline surface. In the creation of the B-spline, first, many connected triangular surfaces are selected within the freehand drawing sections and these triangular surfaces are made compatible with the B-spline surface. The proper B-spline surface is taken as an input and the region is enlarged by adding corners that are not included but adjacent to the existing region [7]. Bicubic B-Spline surface is defined as follows;

$$S(u,v) = \sum_{i=0}^{m} \sum_{j=0}^{n} d_{i,j} N_{i,3}(u) N_{j,3}(v) \qquad (1)$$

$$0 \leq u, v \leq 1 \qquad (2)$$

$d_{i,j}$ indicates control points, and $N_{(i,3)}(u), N_{(j,3)}(v)$ represent the 3rd order univariate B-Spline basic functions in the u, v direction defined on the $U = \{u_0, u_1, \ldots, u_{(m+4)}\}$, $V = \{v_0, v_1, \ldots, v_{(n+4)}\}$ node vectors respectively [10]. It is developing day by day by modeling of machine parts and especially gear wheels with the reverse engineering method as parametric or non-parametric and then by producing with rapid prototype process [11-13]. The general purpose of these studies is to fill the damaged areas of parts in a virtual environment and obtain the whole part. The realization of these processes is targeted with the lowest precision and different modeling features are used. In our study, a damaged automobile cam gear was remodeled as 3D by the reverse engineering method, and then it was produced with the Fused Deposition Modeling (FDM) method, which is one of the rapid prototyping processes. The current aspect of our study is that the damage size of the cam gear is large and the modeling feature is carried out according to the polar duplication feature. In addition, in our study, it was aimed to produce the cam gear modeled by reverse engineering method in different scales with FDM method and to compare their deviation analysis.

2. Materials and Methods

The cam gear, which takes its movement from the crankshaft by the help of the timing belt, transfers its motion to the camshaft. The purpose of the camshaft is to determine the opening and closing time of the valves. In this study, it was aimed to perform 3D modeling of the damaged cam gear that was taken from the industry and to reproduce it with the help of the rapid prototyping method. For this purpose, the cam gear was modeled primarily as 3D by the reverse engineering method. In general, a specific plan should be created for the part in the reverse engineering process. Within the framework of this plan, the part was first cleaned with the help of certain liquid solutions, markers were placed in certain places on the part, and then powdering was done to make the part surface matte (Figure 2)

Figure 2. Schematic representation and preparation of the cam gear for 3D scanning
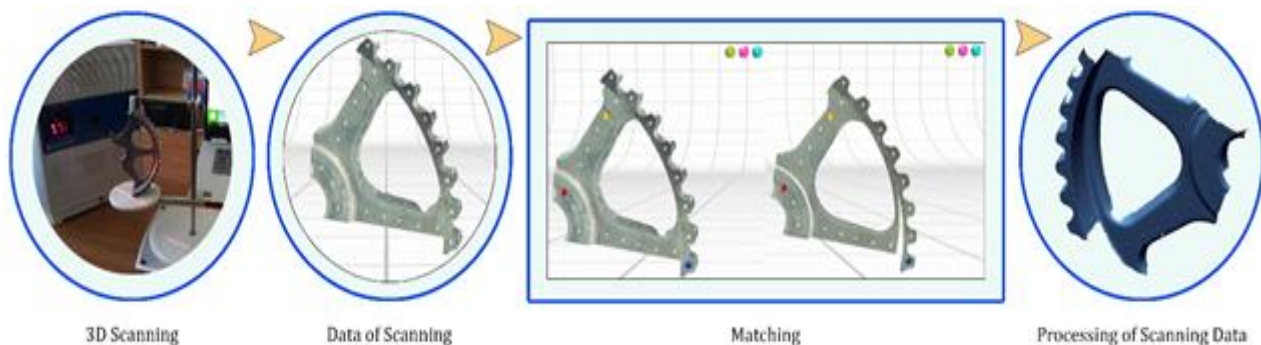

Figure 3. Data processing stages of 3D scanning data

The part surface cleaning process involves removing unnecessary small particles on the part surface during 3D scanning. At the end of this process, the part was left to dry and then marking was performed to create a reference on the important regions of the surface. When multiple scans are performed, the marking process ensures that the scan data overlaps. The finishing of these processes is powdering. In this finishing, the surface was matted to prevent laser beams from reflecting off the part surface during scanning. The level of delustering varies based on the person performing the 3D scanning process and the scanning data generated.

2.1 3D Scanning, Data Capture and Data Processing

3D data collection methods used for 3D modeling of objects are performed by many devices such as Computed Tomography (CT), Magnetic Resonance Imaging (MRI), Ultrasonic Imaging, Photogrammetry, Computerized Coordinate Measuring Device (CMM), and Laser Scanner. These devices are used also assertively in the field of reverse engineering as well as their own functions. Each of these devices has advantages and disadvantages over each other. These devices can be separated into two as contact and non-contact depending on the data obtained [14]. In the contact method, an object is contacted with the help of a physical sensor and the data of the point of contact is received. In the noncontact method, images acquired previously with the help of digital cameras are processed. Surfaces formed with the help of data obtained through

data capture and data processing are smoothed, the number of data is optimized, and unnecessary data is eliminated. In this study, the NextEngine (NextEngine Inc.) device, which performed noncontact scanning, was used. The processes from 3D scanning to data processing are shown in Figure 3. A good strategy should be determined at the beginning of the 3D scanning process. Although doing too many scanning processes may seem like an advantage, the processing speed of the computer may decrease due to the excess data. Therefore, a good planning is needed to complete these processes in a short time. The processes described in this study were optimally completed.

On the data images of the cam gear scanned from different angles, the matching process is performed by determining a minimum of three points on both images. As a result of the matchings, real scanning data is obtained. The hierarchy of the 3D-scanned data in Geomagic Design X software (3D Systems, Inc.) used in this study is shown in Figure 4. Sections considered as noise in the data obtained from the scan device are corrected in the mesh improvement section. If there are missing corrections, correction can be made again in the next steps, the existing triangular edge length determined in the global re-mesh assignment section can be changed, and open meshes can be closed. In this section, when the surface properties are desired to be more specific, it is desired that the triangular edge length is below the current length value. As a result of these processes, the mesh number can increase and it can slow down the computer used.
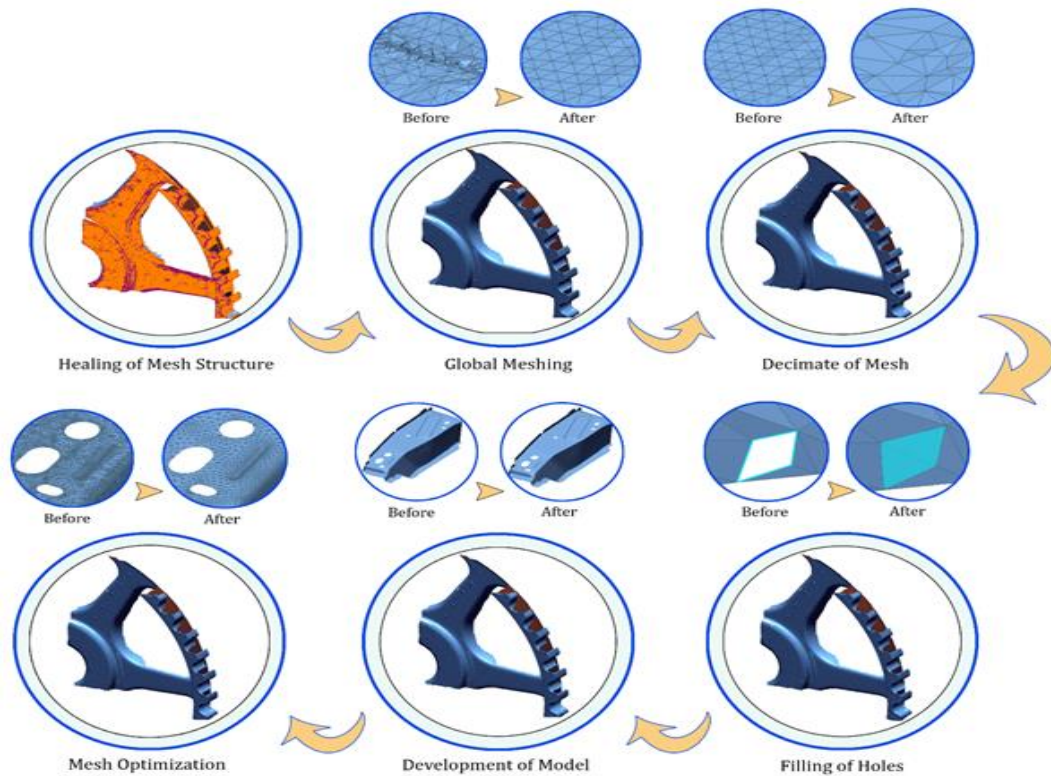
Figure 4. Flow chart of data processing section in reverse engineering

To reduce the increasing number of mesh, the mesh editing process uses algorithms that contain multiple surface counts or allowable deviation parameters. Filling the gaps ensures that the gaps in the mesh surface sections of the part are filled. These gaps may be in straight or curved forms. In terms of filling the gaps, a healthy process can be realized by taking into consideration the gap curvature. The shape developing process is used to increase the overall smoothness and clarity of the mesh structure. In the mesh optimization section, it is ensured that the uniform mesh structure with desired size is created on the part. This part should be analyzed well and the most ideal mesh structure should be created for the part.

2.2 Segmentation and Feature Classification

The segmentation process searches the nearest neighbors with a fast algorithm by using the received data and it includes the prediction of first and second order surface properties [15]. As a result of this process, the surfaces are divided into separate regions. The segmentation process is an important factor in the healthy creation of CAD reconstruction. The segmentation process regulates the parameters that affect the type and size of the defined regions [16]. There are many studies on segmentation processes in the literature. In the most comprehensive study, the segmentation process was examined in 10 steps (clustering, region growing, surface fitting, topology, spatial subdivision, spectral analysis, boundary detection, motion characteristics, probabilistic models, and co-

segmentation) [17]. Since the feature classification process is used as a result of the segmentation method and depends on the segmentation features, it should be considered with it. In our study, after the data processing section, the segmentation process was applied on the cam gear (Figure 5). In the data processing section, part surfaces were stabilized and smooth regions were created. Based on the modeling strategy, the formation of suitable surfaces (segmentation) and their modeling properties (feature classification) were determined (Figure 5). It was thought that it would be appropriate to model the hub of cam gear with the Extrude feature and the diameter parts of the hub with the Chamfer feature. In addition, the Fillet feature was used in the corners of the support parts used in the gear and the Extrude feature was also used in the thickening of the gear parts.
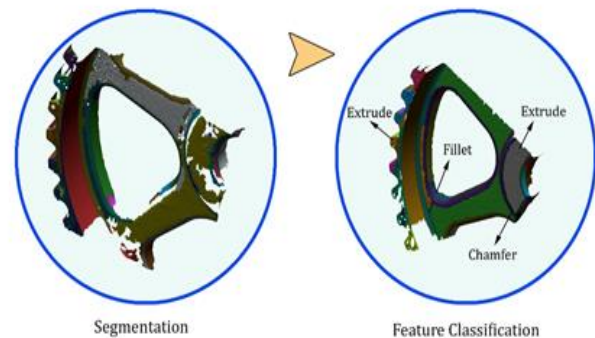

Figure 5. Application of Segmentation and feature classification processers cam gear
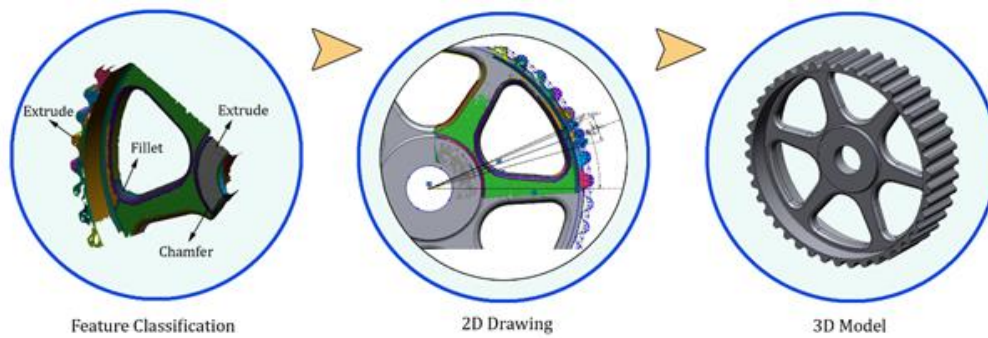
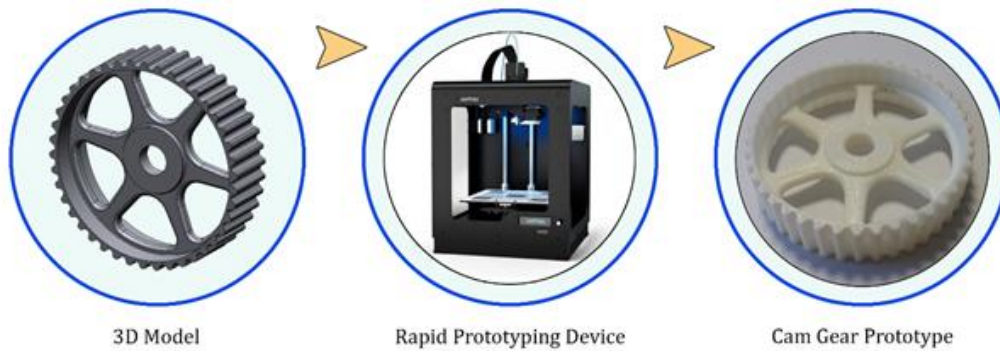Figure 6. Modelling operation in reverse engineering

Figure 7. Reverse engineering process of the cam gear

2.3 Modelling

In this section, as a result of determining the mesh model features, a plane is created by using these features and geometric drawings are made. In order to make this process healthy, the feature classification process should be performed optimally. In our study, modeling features were determined, plane and 2D drawings were created and modeling operations were carried out (Figure 6).

2.4 CAD Modelling and Rapid Prototyping

In this section, before the rapid prototyping process, the final state of the model created by using the feature classification process is created. By considering subsequent processes, the formation of the CAD model can be performed as parametric or non-parametric. With the help of the features used in the model section, the geometry of the part can be in surface or solid form. Clamping of adjacent surfaces, forming of radius and chamfers, and performing geometric constraints can be shown as the other operations of this section [18]. The prototype of the occurred 3D modeling can be created according to the desired rapid prototyping method, the desired material and mechanical characterization. Many processes related to rapid prototyping have been developed and introduced in the last few decades. These process types are gradually developing and their variety increases with the develoing technology. There are some rapid prototyping processes that are generally known in the literature [19-21]. These are known as Stereolithography (SLA), Electron Beam Melting (EBM), Direct Metal Laser

Sintering (DMLS), Fused Deposition Modelling (FDM), Melting (SLS/SLM) or Selective Laser Sintering, Three Dimensional Printing (3DP), Laminated Object Modelling (LOM). In our study, the prototype model of the cam gear which was created with the help of reverse engineering, was carried out using the FDM method (Figure 7). In this method, many parameters affect the surface roughness and mechanical characteristics of the part.

3.   Results and Discussion

In this study, a damaged cam gear was scanned with a 3D laser scanner and converted into a mesh form, and then a CAD model and prototype were created with the help of certain reverse engineering and rapid prototyping processes. Reverse engineering processing time and difficulty vary according to the damage level of the part. If the damage is only at the tooth region of the cam gear, the processing time will be slightly shorter. However, in our study, the large damage on the cam gear part increased both the processing time and the processing difficulty level. In the reverse engineering process, since backward modeling is performed, the dimensional accuracy of the geometrical parts becomes important. The combination of errors emerging due to the device, software or operator used in each stage gives us the total error in the resulting model. Therefore, a detailed examination is required for each stage. Accuracy analysis between the mesh model and the solid model created in reverse engineering is given in Figure 8.
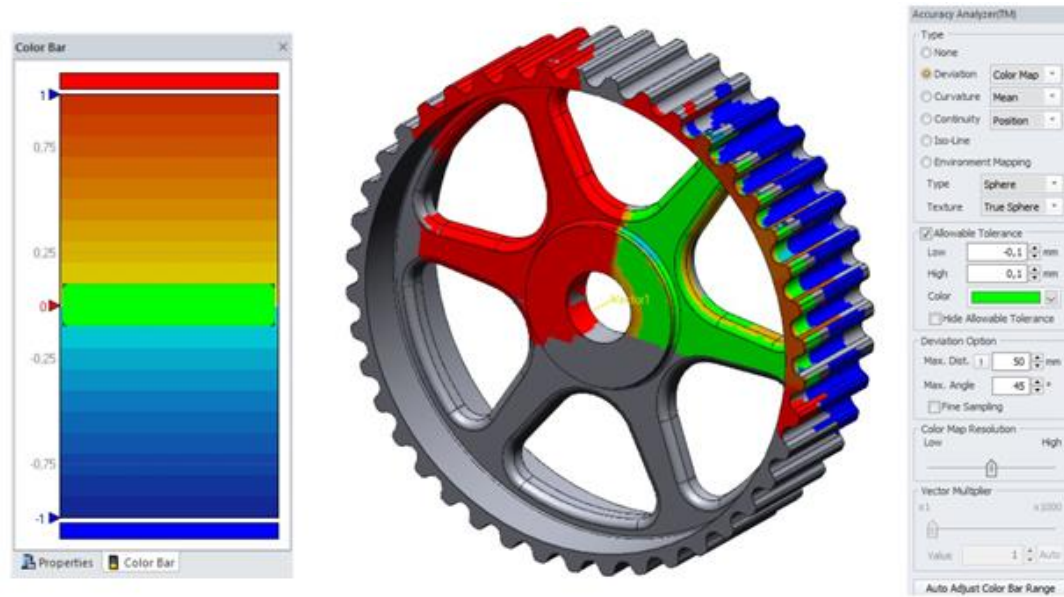
Figure 8. Accuracy analysis between mesh and solid model

Table 1. Dimensional comparisons between the damaged gear and the rapid prototype gear.

Dimension Name	Specimen (mm)	Prototype Sample 1 (1/1)) (mm)	Prototype Sample 2 (1/2) (mm)	Prototype Sample 3 (1/4) (mm)	Deviation 1 (1/1) (%)	Deviation 2 (1/2) (%)	Deviation 3 (1/4) (%)
d	123.31	123.25	61.82	30.97	0.999513	1.002676	1.004866
d1	116.48	116.35	58.37	29.25	0.998884	1.002232	1.004636
d2	39.17	39.47	19.89	10.05	1.007659	1.015573	1.026551
d3	17.49	17.32	8.86	4.48	0.99028	1.01315	1.025157
R1	12.05	11.94	6.17	3.11	0.990871	1.024066	1.033195
R2	5.6	5.54	2.87	1.45	0.989286	1.025	1.039286
			Average Accuracy		99.60823	98.64831	97.83683

In the accuracy analysis, the average deviation values between mesh surfaces and solid surfaces were obtained by the help of the algorithm in the Geomagic Design X software (3D Systems). When we look at the color scale shown in the figure, it is seen that most of the solid model we obtained from the mesh model is shown in green color (average deviation: ± 0.1 mm). Although slightly different colors (average deviation ≈ 0.1-0.2 mm) may appear in the radius regions of the gear part, it was understood that the deviation is not too much. Because the mesh model is small and the solid model created with the help of the mesh model is large, a large region of the part does not contact with each other. Therefore, the regions where mesh and solid model do not overlap are the regions where blue and red colors dominate.

There are two important strategies for creating a 3D model in reverse engineering applications. These are solid feature-based and surface feature-based methods [2,7,22-24]. They are also divided into many stages within themselves. In this study, the cam gear was modeled by using the features in the solid feature-based modeling content. It is important to choose a solid feature-based strategy for modeling mechanical or non-mechanical parts with the regular geometry. With this strategy, since fewer elements are used in the modeling process, both the file size will be reduced and the smoothness of the part

surfaces will be ensured. In the surface feature-based modeling, the number of elements should be high in order to define the surfaces in detail. This increases file size and surface irregularity. In defining these surfaces, it will be appropriate to use NURBS (Non-uniform rational B-spline) surface elements used to define irregular surfaces in detail [21]. Based on the FDM method, which is one of the rapid prototyping methods, the gear, created with the help of solid feature-based modeling, was produced in three different scales (1/1, 1/2 and 1/3) (Table 1). The size comparison of the gear was made with the variables of d (major diameter), d1 (minor diameter), d2 (hub diameter), d3 (bore diameter), R1, and R2. The deviation of all three prototype parts from the real models and average accuracy values between models are given in Table 1. Dimensional measurements of the parameters determined on the prototype models were carried out with the help of an Insize (Insize Co.) trademark digital caliper with an accuracy of 0.01 mm. According to the results given in Table 1, considering the 1/1 scale, the average accuracy value between the real model and the prototype model was found to be 99.60%. Considering the 1/2 scale and the 1/4 scale, this value was found as 98.64% and 97.83%, respectively.

4. Conclusions

When we look at the reverse engineering hierarchy in general, we see that each stage has its own process steps and specific details. Here, the knowledge and experience history of the person performing this operation is important. The person performing the modeling process must initially determine a modeling strategy for the part. According to this strategy, he/she should analyze each step in detail and complete the sections in a healthy way. In addition, the variation of the method used in 3D printers, the material used, the temperature of the environment during production in the 3D printer, and the sensitivity of the electronic and mechanical system affect the results of deviation analysis.

As a result of modeling processes, considering the average accuracy values between the real model and the prototype model, it was seen that 1/1 scale production was more accurate. It is observed that the average accuracy rate gradually decreases as the scale factor value decreases. While the results are being evaluated, it will be also appropriate to evaluate the other methods in the production of parts considering the roughness created by the FDM method, which is one of the rapid prototype methods.

Declaration

The author(s) declared no potential conflicts of interest with respect to the research, authorship, and/or publication of this article. The author(s) also declared that this article is original, was prepared in accordance with international publication and research ethics, and ethical committee permission or any special permission is not required.

References

1. Kovács, I., T. Várady, and P. Salvi, *Applying geometric constraints for perfecting CAD models in reverse engineering.* Graphical Models, 2015. **82**: p. 44-57.

2. Kumar, A., P.K. Jain, and P.M. Pathak, *Reverse engineering in product manufacturing: an overview.* Daaam International Scientific Book, 2013. p. 665-678.

3. Arslan, M., İ. Kacar, T. Yadigaroğlu, and M .Muhsuroğlu, *Design and production of a fixed anode x-ray tube.* International Advanced Researches and Engineering Journal, 2018. **2**(2): p 153-158.

4. Buonamici, F., M. Carfagni, R. Furferi, L. Governi, A. Lapini, and Y. Volpe, *Reverse engineering of mechanical parts: A template-based approach.* Journal of computational design and engineering, 2018. **5**(2): p 145-159.

5. Shashank, A., *A Review of 3D Design Parameterization using Reverse Engineering.* International Journal of Emerging Technology and Advanced Engineering, 2013. **3**(10): p 171-179.

6. Wang, J., D. Gu, Z. Gao, Z. Yu, C. Tan, and L., Zhou, *Feature-based solid model reconstruction.* Journal of Computing and Information Science in Engineering, 2013. **13**(1): 011004.

7. Wang, J., D. Gu, Z. Yu, C. Tan, and L., Zhou, *A framework for 3D model reconstruction in reverse engineering.* Computers & Industrial Engineering, 2012. **63**: p 1189-1200.

8. Owen, S.J., M.L. Staten, S.A. Canann, and S. Saigal, *Q-Morph: an indirect approach to advancing front quad meshing.* International Journal for Numerical Methods in Engineering, 1999. **44**: p 1317-1340.

9. Tarini, M., N. Pietroni, P. Cignoni, D. Panozzo, and E. Puppo, *Practical quad mesh simplification.* In Computer Graphics Forum, 2010. **29**: p 407-418.

10. Wang, J. and Z. Yu, *Surface feature based mesh segmentation.* Computers & Graphics, 2011. **35**: p 661-667.

11. Tut, V., A. Tulcan, C. Cosma, and I. Serban, *Application of CAD/CAM/FEA, reverse engineering and rapid prototyping in manufacturing industry.* International Journal of Mechanics, 2010. **4**: p 79-86.

12. Paulic, M., T. Irgolic, J. Balic, F. Cus, A. Cupar, T. Brajlih, and I. Drstvensek, *Reverse engineering of parts with optical scanning and additive manufacturing.* Procedia Engineering, 2014. **69**: p 795-803.

13. Dúbravčík, M. and Š. Kender, *Application of reverse engineering techniques in mechanics system services.* Procedia Engineering, 2012. **48**: p 96-104.

14. Varady, T., R.R. Martin, and J. Cox, *Reverse engineering of geometric models—an introduction.* Computer Aided Design, 1997. **29**: p 255-268.

15. 3D Systems, [cited 2019 01 October]; Available from: https://uk.3dsystems.com/our-story

16. Buonamici, F., M. Carfagni, R. Furferi, L. Governi, A. Lapini, and Y. Volpe, *Reverse engineering modeling methods and tools: a survey.* Computer-Aided Design and Applications, 2018. **15:** p 443-464.

17. Theologou, P., I. Pratikakis, and T. Theoharis, *A comprehensive overview of methodologies and*

performance evaluation frameworks in 3D mesh segmentation. Computer Vision and Image Understanding, 2015. **135**: p 49-82.

18. Benkő, P., R. R. Martin, and T. Várady, *Algorithms for reverse engineering boundary representation models.* Computer-Aided Design, 2001. **33**: p 839-851.

19. Dudek, P. and A. Rapacz-Kmita, *Rapid prototyping: Technologies, materials and advances*. Archives of Metallurgy and Materials, 2016. **61**: p 891-896.

20. Campbell, I., D. Bourell, and I. Gibson, *Additive manufacturing: rapid prototyping comes of age.* Rapid Prototyping Journal, 2012. **18**: p 255-258.

21. Gibson, I., D. W. Rosen, and B. Stucker, *Additive manufacturing technologies: Rapid prototyping to direct digital manufacturing*, Published by Springer 2010. US, p 1-459.

22. Günpınar, E., *Tersine mühendislik yoluyla üç boyutlu geometrik modelin oluşturulması ve gemi yapım endüstrisindeki bazı uygulamaları*. Dokuz Eylül Üniversitesi Mühendislik Fakültesi Fen ve Mühendislik Dergisi, 2016. **18**: p 624-639.

23. Anwer, N. and L. Mathieu, *From reverse engineering to shape engineering in mechanical design*. CIRP Annals, 2016. **65**: p 165-168.

24. Ke, Y., S. Fan, W. Zhu, A. Li, F. Liu, and X. Shi, *Feature-based reverse modeling strategies.* Computer Aided Design, 2006. **38**: p 485-506.

Research Article

Band-stop filter design based on split ring resonators loaded on the microstrip transmission line for GSM-900 and 2.4 GHz ISM band

Alparslan Cinar [a],* [ID] *and Sinan Bicer [a]* [ID]

[a]Akdeniz University, Elmali Vocational School, Antalya 0770, Turkey

ARTICLE INFO	ABSTRACT
	Split-ring resonator is a popular research topic in literature. As known, it may be used in the design of electromagnetic metamaterials. Additionally, these structures can be preferred in microwave filter devices. In this study, a band-stop filter was designed for GSM-900 and 2.4 GHz ISM band by using split-ring resonators. Two split-ring arrays (sizes of one of these arrays were larger than the other) were loaded on the transmission line and each array consisted of four identical rings. Thus, a dual-band pass filter was obtained and this filter covered the frequency of 0.91 (GSM) and 2.43 (ISM) GHz. Then, this proposed design was fabricated and measured. According to the measurement results, the fabricated structure operated at 0.93 GHz and 2.47. The experimental results were consistent with the simulation results. As a result, thanks to the proposed structure, two frequencies can be stopped at the same time. There is no need to design a different filter structure for each frequency.

1. Introduction

Metamaterials are artificial materials and in desired frequency, they may exhibit extraordinary electromagnetic properties (e.g., negative permeability, negative permittivity, reverse Doppler Effect and negative refractive) [1, 2]. Due to these features, it takes place in many applications such as filters [3-22], antenna [23, 24], absorbers [25, 26] and sensors [4, 5, 13, 14, 16, 18, 21, 22, 27, 28]. Split ring resonators (SRR) are one of the most preferred structures for electromagnetic metamaterials design [2-5, 8, 14, 18].

One of the applications in which metamaterials are widely used is filters [3-22]. In this study, it was aimed to design a band-stop filter for GSM-900 and 2.4 GHz ISM band. A lot of SRR-based dual/multi-band stop filter designs are available in the literature [4-10,14,17]. According to some of these studies, dual/multi-band filters can be obtained when two or more SRR structures with different resonance frequencies load the microstrip transmission line [4-6]. Also, resonance magnitude can be increased by increasing the number of rings having the same resonance frequency [6,12].

In this study, two resonator arrays were placed on the transmission line. Each array consisted of four identical rings and sizes of one of these arrays were smaller than the other. To enhance the transmission coefficients $|S_{21}|$ magnitude of the filter structure in operation frequency, the number of resonators was increased without changing their size. Thus, a dual band stop filter was achieved that operated at frequencies of 0.91/2.43 GHz and 0.93/2.47 GHz in simulation and measurement, respectively.

In the context of this study, a filter that stopped two different frequency bands was designed, fabricated and measured. Thus, thanks to this design, there is no need to design two-filter structures for two different frequencies. In addition, frequency tuning can also be made by changing the dimensions of the split ring resonators.

2. Simulation and Measurement

A 50 Ω microstrip transmission line was designed. Schematic view of the proposed transmission line with its design parameters is given in Figure 1. The structure consists of a line at the top, dielectric layer in the middle and ground plane at the bottom. FR4, which had thickness

of 1.6 mm, permittivity (ε_r) of 4.3, and loss tangent (tanδ) of 0.025, was used as the dielectric substrate layer. Line and ground plane were built using copper having a conductivity of 5.8 × 10^7 S/m and thickness of 0.035 mm. Design and analysis of the microstrip transmission line were performed using the CST microwave studio based on frequency domain solver. The proposed structure was excited by using a waveguide port. In addition, boundaries were selected as open for x, y and z axes. S-parameter results of the transmission line obtained from simulation were plotted in Figure 2.

Firstly, 1 SRR was loaded on the proposed transmission line in order for that the structure would behave like a band stop filter in 2.43 GHz. However, $|S_{21}|$ magnitude of the filter was not satisfactory in resonance frequency. Therefore, one more from the same SRR was placed again on this structure. Since it was observed that this was useful, the SRR placement process continued until the number of SRR was 4. The design parameters and schematic views of these structures (design 1 — design 4) are given in Figure 3. The transmission coefficients $|S_{21}|$ obtained from the simulation software are shown in Figure 4.
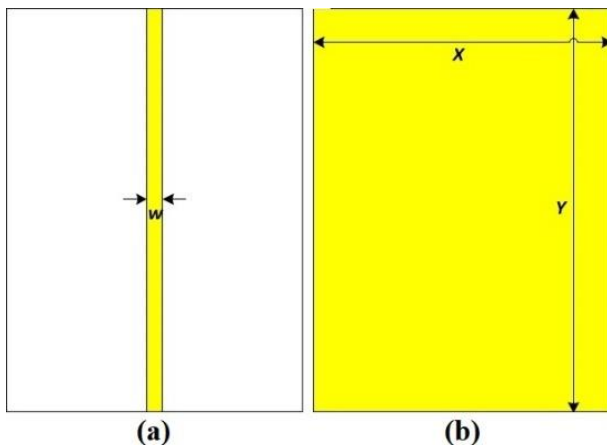
Figure 1. Schematic views of the transmission line a) front, b) back; $w = 2.87$, $X = 80$ and $Y = 110$ (all in mm)
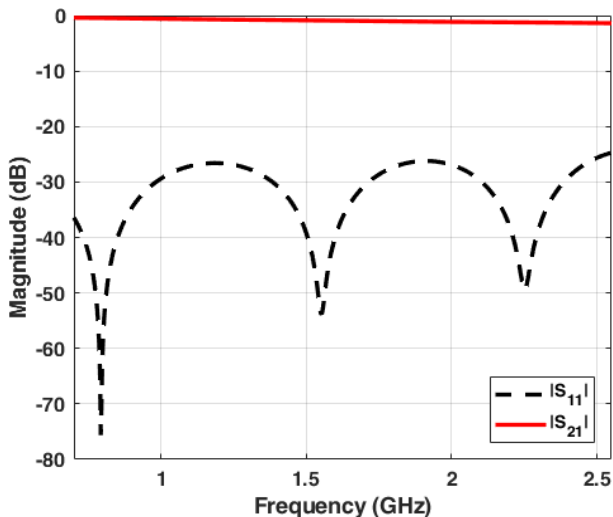
Figure 2. S-parameter simulation results of the transmission line
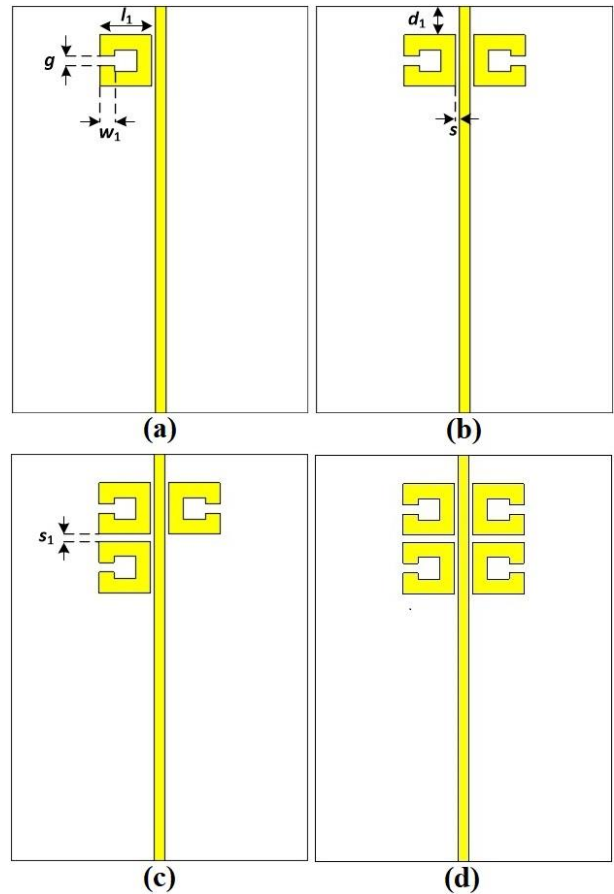
Figure 3. SRR loaded transmission line a) design 1, b) design 2, c) design 3, d) design 4; $l_1 = 13.9$, $w_1 = 4$, $g = 2.5$, $d_1 = 7.7$, $s = 1$ and $s_1 = 2$ (all in mm)
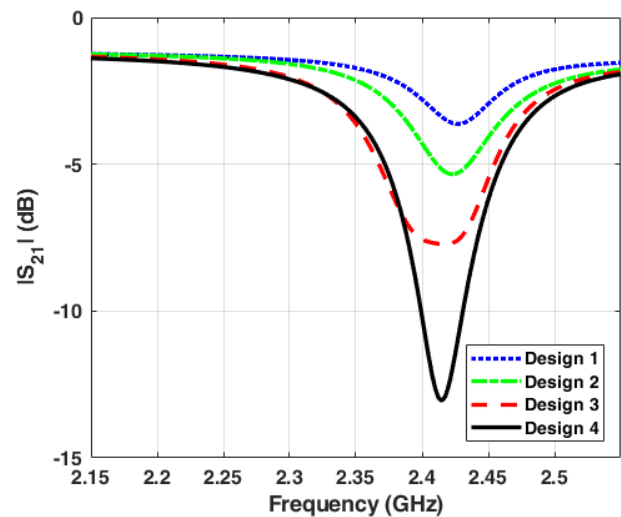
Figure 4. Simulation results of the transmission coefficients $|S_{21}|$ for design 1, design 2, design 3 and design 4

Secondly, 1 SRR was added again to the transmission line shown in Figure 1. However, size of this newly added ring was larger than the SRRs shown in Figure 3. The operation frequency decreases as the size of the resonator length increases. This structure behaves as a band stop filter and operates at 0.91 GHz. In order to enhance $|S_{21}|$ magnitude of the filter, SRR loading continued until the number of the SRR was 4. Schematic view of these

structures are given in Figure 5. The transmission coefficients $|S_{21}|$ of the designed structures (design 5 — design 8) are shown in the figure 6.

Finally, design 4 and design 8 were combined; thus, two resonator arrays were loaded on the microstrip transmission line. Although each array consisted of 4 SRRs, the sizes of one of these arrays were larger than the other. In this way, a dual-band operation was achieved at 0.91 GHz and 2.43. Then, the proposed structure was fabricated and the ends of the transmission line were terminated with 50 Ω SMAs. Schematic and fabricated views of the proposed dual band stop filter are shown in Figure 7. The transmission coefficient $|S_{21}|$ of the fabricated filter was measured using the Anritsu MS4624B vector network analyzer operating in the frequency range of 10 MHz — 9 GHz. The fabricated structure operates at 0.93 GHz and 2.47. As seen in Figure 8, the experimental results are consistent with the simulation results.

Surface current distributions obtained from the simulation are demonstrated in Figure 9. As seen, the surface current behaviors are circular at resonance frequencies. In addition, it is seen that whereas the low frequency (0.91 GHz) is caused by large rings, the high frequency (2.43 GHz) is caused by small rings.

Figure 6. Simulation results of the transmission coefficients $|S_{21}|$ for design 5, design 6, design 7, and design 8
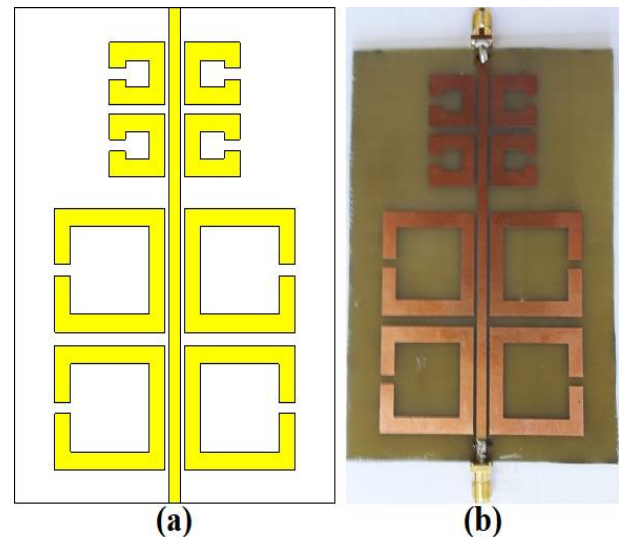
Figure 7. Views of the proposed dual band stop filter
a) schematic, b) fabricated

Figure 5. SRR loaded transmission line a) design 5, b) design 6, c) design 7, d) design 8; $l_2 = 27.6$, $w_1 = 4$, $g = 2.5$, $d_2 = 7.7$, $s = 1$ and $s_2 = 3$ (all in mm)
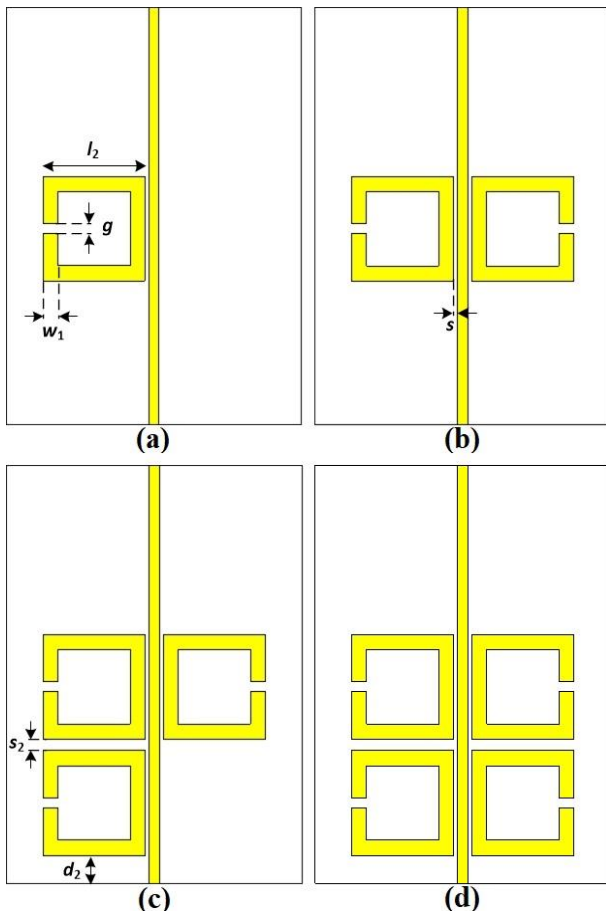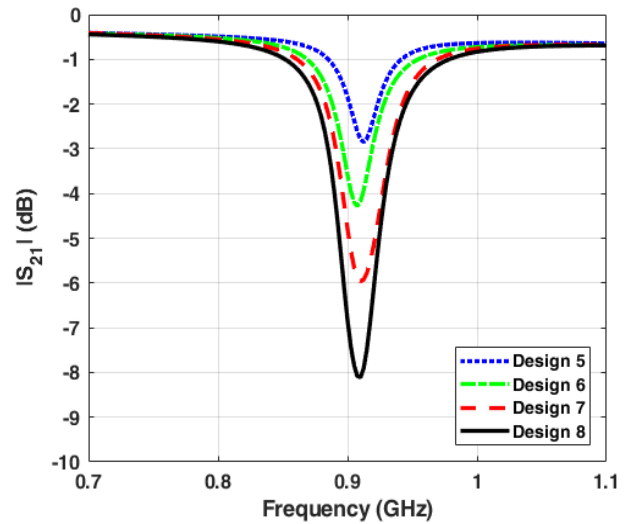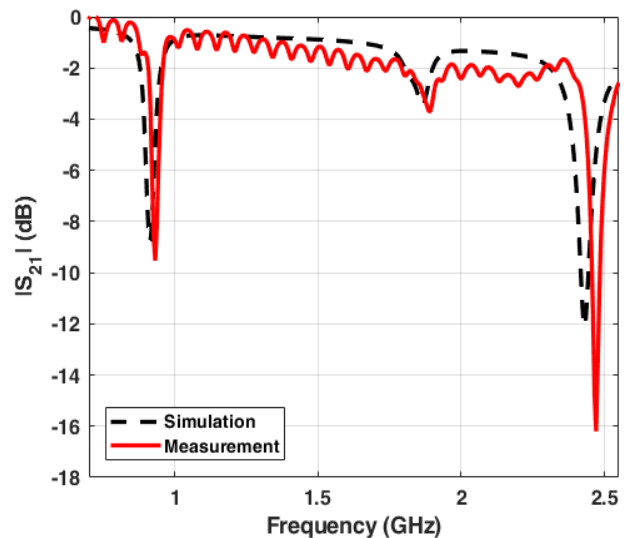

Figure 8. Simulation and measurement results of the transmission coefficients $|S_{21}|$ for the proposed dual band stop filter
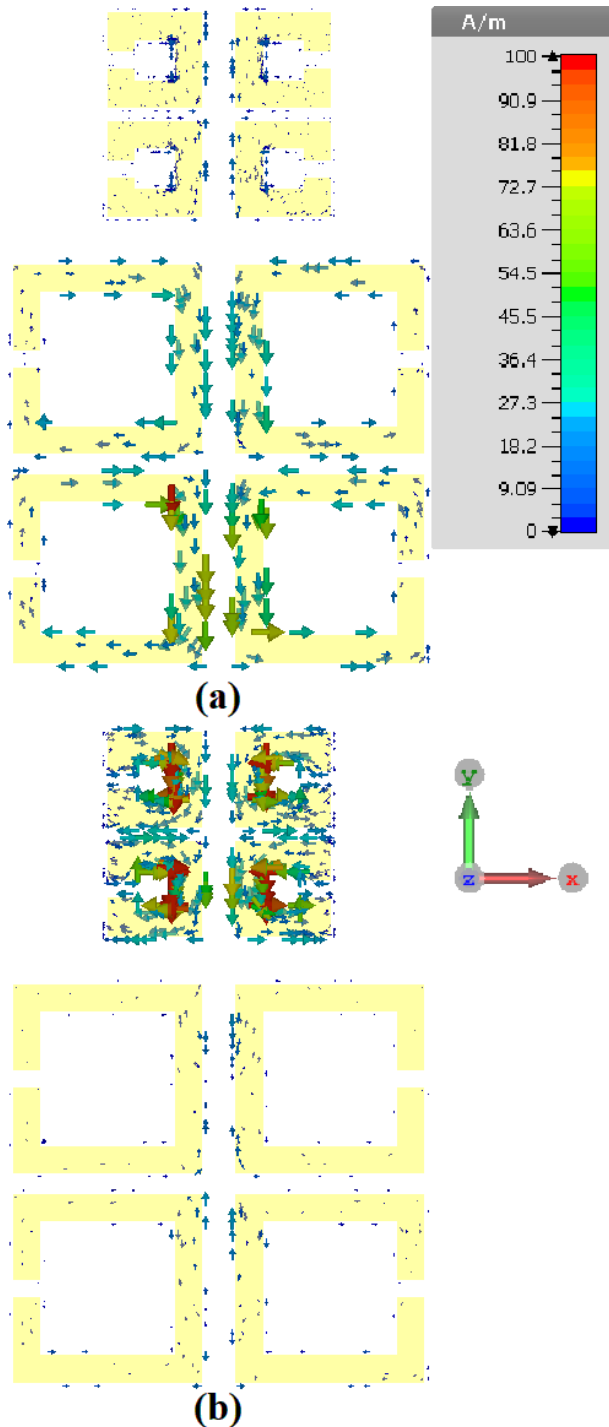
Figure 9. Surface current distributions obtained from the simulation at 0° phase angle a) 0.91 GHz, b) 2.43 GHz.

3. Conclusions

In this paper, a band-stop filter based on split ring resonators loaded on the microstrip transmission line for GSM-900 and 2.4 GHz ISM band was introduced. Two resonator arrays, which had different sizes, were placed on the transmission line. Sizes of one of these arrays were larger than the other and each array consisted of four identical rings. When the simulation and measurement results were examined, the dual-band operation was seen at 0.91/2.43 GHz and 0.93/2.47 GHz in simulation and measurement, respectively. The measured transmission coefficient $|S_{21}|$ of the fabricated filter proved good agreement with the simulated data obtained from simulation software. Finally, it can be said that the proposed structure can stop two frequencies at the same time and there is no need to design a different filter structure for each frequency.

Declaration

The author(s) declared no potential conflicts of interest with respect to the research, authorship, and/or publication of this article. The author(s) also declared that this article is original, was prepared in accordance with international publication and research ethics, and ethical committee permission or any special permission is not required.

References

1. Veselago, V.G., *The Electrodynamics of Substances With Simultaneously Negative Values of ε and µ*. Physics-Uspekhi, 1968. **10**(4): p. 509-514.

2. Caloz C. and T. Itoh, *Electromagnetic Metamaterials, Transmission Line Theory and Microwave Applications*. 2006, USA: John Wiley & Sons.

3. García-García, J., F. Martín, F. Falcone, J. Bonache, J.D. Baena, I. Gil, E. Amat, T. Lopetegi, M.A.G. Laso, J.A.M. Iturmendi, M. Sorolla and R. Marqués, *Microwave filters with improved stopband based on sub-wavelength resonators*. IEEE Transactions on Microwave theory and techniques, 2005. **53**(6): p. 1997-2006.

4. Puentes, M., M. Maasch, M. Schüßler and R. Jakoby, *Frequency multiplexed 2-dimensional sensor array based on split-ring resonators for organic tissue analysis*. IEEE Transactions on Microwave Theory and Techniques, 2012. **60**(6): p. 1720-1727.

5. Withayachumnankul, W., K. Jaruwongrungsee, C. Fumeaux and D. Abbott, *Metamaterial-inspired multichannel thin-film sensor*. IEEE Sensors Journal, 2012. **12**(5): p. 1455-1458.

6. Korucu H.D. and E. Ekmekçi, *Metamalzeme Tabanlı ve İki Bantlı Mikroşerit Bant Durduran Filtre Tasarımı Araştırmaları*, in İlk Bildiriler Konferansı 2013, Turkey. p. 64-67.

7. Hussain, S., J.M. Woo and J.H. Jang, *Dual-band terahertz metamaterials based on nested split ring resonators*. Applied Physics Letters, 2012. **101**(9): p. 091103.

8. Ali, W.A.E. and M.Z.M. Hamdalla, *Compact triple band-stop filter using novel epsilon-shaped metamaterial with lumped capacitor*. Journal of Instrumentation, 2018. **13**(04): p. P04007.

9. Kamma, A. and J. Mukherjee, *Multiple band notch and Dual-Band filter using concentric and contiguous split ring resonators (CCSRR)*. Journal of Electromagnetic Waves and Applications, 2017. **31**(1): p. 57-71.

10. Hu, X., Q. Zhang and S. He, *Dual-band-rejection filter based on split ring resonator (SRR) and complimentary SRR*. Microwave and Optical Technology Letters, 2009. **51**(10): p. 2519-2522.

11. Disken, G., F. Pala, E. Demir, H.D. Korucu and E. Ekmekci, *Electromagnetic Behavior of SRR Loaded Microstrip Transmission Lines: Investigation for Different SRR Types and Array Topologies*, in *PIERS Proceedings*

2013, Sweden. p. 1796-1799.

12. Çınar, A., U. Köse, Ö. Ertan, N. Karacan, C. Başer and E. Ekmekçi, *Ayrık Halkalı Rezonatör Tabanlı Bağlaşım Değeri Ayarlanabilir Mikroşerit Yönlü Bağlaç Tasarımı ve Benzetimleri*, in *8. URSI-Türkiye Bilimsel Kongresi 2016*, Turkey.

13. Çınar, A. and E. Ekmekçi, *Ayrık Halkalı Rezonatör Tabanlı Dönme Sensörü Tasarımı ve Nümerik Olarak İncelenmesi*, in *8. URSI-Türkiye Bilimsel Kongresi 2016*, Turkey.

14. Memon, M.U., H. Jeong and S. Lim, *Metamaterial-inspired radio frequency based touchpad sensor system*. IEEE Transactions on Instrumentation and Measurement, 2019.

15. Moradi, B., R. Fernández-García and I. Gil, *Effect of smart textile metamaterials on electromagnetic performance for wireless body area network systems*. Textile research journal, 2019. **89**(14): p. 2892-2899.

16. Liu, W., H. Sun and L. Xu, *A microwave method for dielectric characterization measurement of small liquids using a metamaterial-based sensor*. Sensors, 2018. **18**(5): p. 1438.

17. Asci, C., A. Sadeqi, W. Wang, H.R. Nejad and S. Sonkusale, *Design and implementation of magnetically–tunable quad–band filter utilizing split–ring resonators at microwave frequencies*. Scientific Reports, 2020. **10**(1): p. 1-8.

18. Tiwari, N.K., S.P. Singh and M.J. Akhtar, *Metamaterial inspired contactless angular displacement sensor with wide dynamic range and bandwidth*, in *2019 URSI Asia-Pacific Radio Science Conference (AP-RASC) IEEE,* India. p. 1-4.

19. Ahmed, B.A., H. Klaina, O. Aghzout, A.V. Alejos, A. Naghar and F. Falcone, *Miniaturization, Selectivity and Rejection Bandwidth Improvements of a Multi-Band Stopband Filter Based on Circular Split Ring Resonator*, in *2019 13th European Conference on Antennas and Propagation (EuCAP) IEEE*, Poland. p. 1-4.

20. Horestani, A.K., N. Varmazyar, F. Sadeghikia, M.T. Noghani, Z. Shaterian and F. Martín, *On the Applications of S-Shaped Split Ring Resonators (S-SRR) in Sensors, Filters, and Antennas*, in *2019 International Conference on Electromagnetics in Advanced Applications (ICEAA) IEEE*, Spain. p. 0485-0488.

21. Horestani, A.K., Z. Shaterian and F. Martín, *Detection Modalities of Displacement Sensors Based on Split Ring Resonators: Pros and Cons*, in *2019 International Conference on Electromagnetics in Advanced Applications (ICEAA) IEEE*, Spain. p. 0479-0484.

22. Albishi, A.M. and O.M. Ramahi, *Highly Sensitive Planar Microwaves Sensor*, in *2019 IEEE International Symposium on Antennas and Propagation and USNC-URSI Radio Science Meeting IEEE*, USA. p. 339-340.

23. Alici, K.B. and E. Ozbay, *Electrically small split ring resonator antennas*. Journal of applied physics, 2007. **101**(8): p. 083104.

24. Ekmekçi, E., A. Çınar, A. Ayan, H.D. Korucu and E. Demir, *Enine Kuplajlı ve AHR Tabanlı Anten Yapıları İçin Elektriksel Boyut ve Kazanç Analizi*, in *7. URSI-Türkiye Bilimsel Kongresi 2014*, Turkey. p. 379-381.

25. Landy, N.I., S. Sajuyigbe, J.J. Mock, D.R. Smith and W.J. Padilla, *Perfect metamaterial absorber*. Physical review letters, 2008. **100**(20): p. 207402.

26. Al-Badri, K.S., A. Cinar, U. Kose, O. Ertan and E. Ekmekci, *Monochromatic tuning of absorption strength based on angle-dependent closed-ring resonator-type metamaterial absorber*. IEEE Antennas and Wireless Propagation Letters, 2016. **16**: p. 1060-1063.

27. Ekmekci, E., U. Kose, A. Cinar, O. Ertan and Z. Ekmekci, *The use of metamaterial type double-sided resonator structures in humidity and concentration sensing applications*. Sensors and Actuators A: Physical, 2019. **297**: p. 111559.

28. Ertan, Ö., U. Köse, A. Çınar and E. Ekmekçi, *Sensitivity analysis of different resonator structure for sensor applications in microwave region*, in *2016 National Conference on Electrical, Electronics and Biomedical Engineering (ELECO) IEEE*, Turkey. p. 550-553.

Research Article

Electronic and mechanical design of a hexapod land searching robot

Talha Boz [a] (iD)*, İsmail Aras* [a] (iD)*, Samet Kıkıcı* [a] (iD) *and Sezgin Ersoy* [a,*] (iD)

[a]Marmara University Technology Faculty Mechatronics Engineering Department, Istanbul.34752, Turkey

ARTICLE INFO	ABSTRACT
	In this study, it is aimed to design a robot that can be used in fields such as land exploration, mine search, ammunition transportation, search and rescue activities in natural disasters. For this purpose, a six-legged robot was designed. The robot can move evenly in uneven terrain conditions, stop, accelerate and overcome the obstacle when it sees an obstacle. The mechanical and electronic design of the robot was realized, and a prototype was manufactured. The flexibility of the legs used in the design ensures that the robot can move more easily in field conditions. The synchronous speed and direction of the motors are controlled, and the robot moves in a balanced way. With the IP camera mounted on a Raspberry Pi, snapshots were taken from the robot. Mechanical and electronic design of six-legged robot capable of moving on uneven ground was realized. The six-legged robot was placed with three legs on the right and three legs on the left. The motors were operated simultaneously to allow the robot to move evenly. Thanks to its leg structure, it was aimed to travel in land conditions. Image control was provided on the computer with the camera placed on the robot. In this study, the program written into the electronic cards run the motors simultaneously.

1. Introduction

In recent years, autonomous robots have been utilized in many areas such as search and rescue, mapping, reconnaissance, mine detection, packaging and geolocation [1-3]. Mobile robots have been designed with different modes of transportation such as wheel and leg structures. With the advancement of the sensors, robots can interact with the environment and autonomously carry a task using machine learning methods [4].

Positioning, mapping, road planning, road planning avoiding obstacles are among the most popular autonomous robot topics in literature [5-7]. In most of the studies, the robot is in a closed area and moves on a flat surface. The most important reason for this is that the signals received by the sensors are required to be noise-free and the control of the robot to be stable. These mobile robots generally use wheels. However, when it was desired to move the mobile robots in an uneven ground, there was a need to develop robots with different structures and number of legs [4], [8]. Although these robots can perform difficult tasks such as moving on rough terrain and

climbing stairs, moving them in a stable and balanced way is one of the biggest problems.

Lauron II [9] of FZI (Forschungszentrum Informatik) group and Genghis robots improved by MIT (Massachusetts Institute of Technology) may exemplify six-legged robots. Each leg of Lauron II robot has 2 degrees of freedom (2-DoF) mechanism. Robot was monitored by 12 actuators in total. Each leg of Genghis robot has 1-DoF mechanism and the system was monitored by 6 motors in total.

In their study, mechanical, electronic and software design of a six-legged robot that can move in uneven surfaces was carried out. The robot designed in this study was inspired by the Rhex [8] robot, which was previously designed at the Code Laboratory at the University of Pennsylvania.

The RHex project first came out of the Darpa CBS / CBBS program in 1998. This project, which was carried out with the participation of many universities, provided 5m USD funding for 5 years. The first prototype was built in 1999 by Uluç Saranlı. Many revisions and improvements have been made on platform design and

algorithms [10]. Throughout its development, it is an autonomous hexapod robot that has developed behavioral algorithms. It is due to a number of principles underlying its design and a significant amount of inspiration from biological systems [11]. It is the first documented autonomous leg machine that exhibits general mobility on a terrain. It can move over a wide range of uneven terrain with speeds exceeding 2.7 m/s, climbing slopes exceeding 45 degrees, swimming and climbing stairs [12].

The materials used in the design was chosen to satisfy the desired properties while being economical. In this way, the robot is intended to be more economical than similar robots. Samples of the robots developed in Aqua Rhex and Wheel Rhex types which are movable in water were also examined [2]. Different multipurpose mobile robots can be seen Figure 1.

The design of the robot was realized in three stages:

- Mechanical Design: design of the chassis and leg structure of the robot.
- Electronic Design: control of six motors simultaneously and stably and remote controller design that will enable wireless data exchange.
- Computer Image Acquisition: design of a camera system on the robot that sends the image to the control station.

In this paper, mechanical and electronic design of the robot and image acquisition via computer are explained in detail. In the third unit, experimental results with robot are given. In the last section, the results and future works are discussed.

2. Method

There are six design components for the hexapod land searching robot, namely mechanical, leg, software, electronic and communication. These stages have been realized in parallel to each other. The designs of both shell and flexible leg structure of the robot were completed and first prototype has been manufactured. The essential control cards' design and the programming requirements were addressed to enable simultaneous movement of more than one motor.

2.1 Mechanical Design

Six stepper motors with a working voltage of 12V and a current of 1000 mA have been selected, which will allow
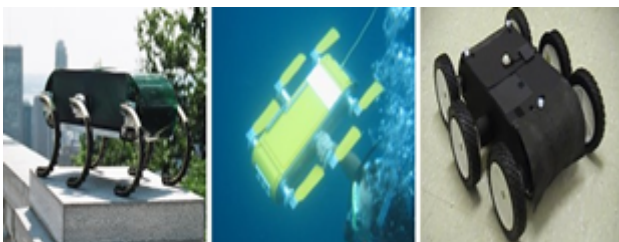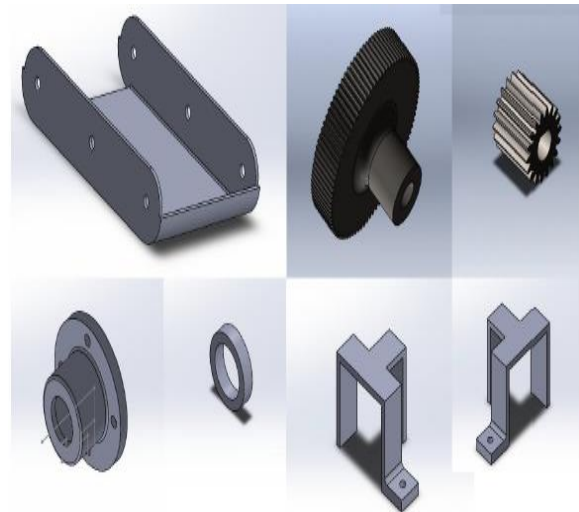

Figure 1. Multipurpose mobile robots [18]

Figure 2. Designs of the components of the robot

the robot to move on uneven surfaces and carry the weight of the robot. A plate was designed for the lower body. Arduino Mega, Arduino Uno, Raspberry Pi, Servo motor, Step motors and gears are placed on this plate. The size of the plate is 25.6 x 19 cm and the wall thickness is 0.5 cm. The design of the components was created in Solid Works and Figure 2 show the images of the components.

The holes on the components were created with a laser cutter. The total weight to be placed on the body was calculated to be approximately 3 kg with motors, electronic cards, gears and shafts.

The completed mechanical design of the robot is shown in Figure 3. The legs are 7 cm in diameter and 1.2 cm in width, and the distance between each leg is 12.8 cm. The middle legs are 1 cm out of line from the front and rear legs. Thus, the legs can perform the movement without interfering each other. The feet are fixed to the 0.8 cm diameter shafts by drilling 0.4 cm holes. 4mm bolts, nuts and washers were used to fix the legs.

A gear system was designed to transfer the power from the motors to the legs as it did not directly produce the needed force for movement. For this reason, the force transferred from motor shaft to the legs was increased quintuple using a 1:5 gear design. Gears were illustrated at Solid Works and printed via 3D printer. Small gear used on motor shaft was tuned-up in accordance with the following criteria: gear tooth 18, module 0.6 and diameter 1 cm. Bigger gear was tuned-up in accordance with the following criteria: gear tooth 90, module 0.6 and diameter 5.2 cm. Shrink fit to the motor shaft was achieved with 5 mm bore diameter. Similarly, shrink fit to the shaft transferring force to the legs was achieved with 5 mm bore diameter.

A tab from main gear was attached to the shaft with a bolt for attaching bigger gear to the shaft firmly. The length of journal connecting bigger gear to the shaft is 15 mm while bore diameter was designed as 4 mm to be in the same size with the shaft hole.
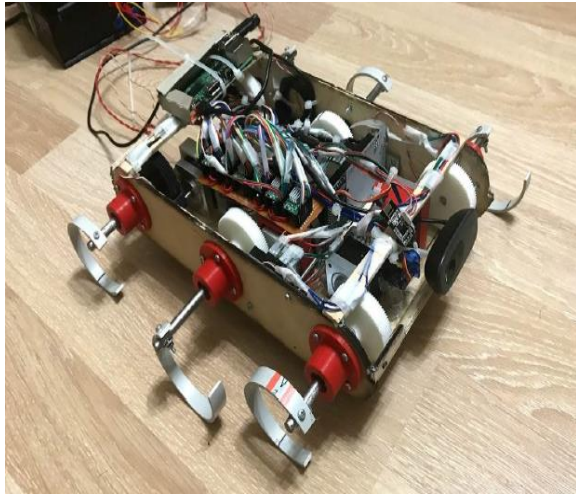
Figure 3. Mechanical design of the robot

Figure 4. Lifting and pulling forces of the leg Geometry

The shaft should move properly and periodically in order for a proper transfer of force to the legs. As the shaft is within the bearing, shaft should be fixed from outside firmly. That is why, it was designed a bearing retainer. Two bearings in 1.5 cm from each other are placed in a retainer and a distance piece is used within the retainer to prevent the contact of bearings. Bearing retainer's outside diameter is 4.9 cm and bearing hole diameter is 22 mm. Shrink fit is ensured by setting internal hole to the same degree of outside diameter of bearing. Distance between two bearings is set by extending 15 mm retainer piece from internal bore diameter of main body. Through this way, the shaft becomes more solid as it is supported from two points. In order to keep the shaft inside, bore diameter at the outmost part of retainer is measured 16 mm. Lastly, 4 mm diameter bolt holes are made to bolt down outside part of retainer to the robot's side walls.

Finally, a clamp was designed to attach the motors to the main body to enable the steadiness of motors on the main body. Motor is screwed to the main body with three-leg clamp while other two legs prevent the motor's skidding. The design of clamp was made via Solid Works and printed with 3D printer.

2.2 Leg Design

A different foot design has been considered for mobility in terrain and unfavorable environmental conditions. This design is inspired by six-legged insects that provide flexible movement across various terrains. The foot design can be highly useful to provide the robot's ability to move [13]. This foot design ensures reliable and robust operation. Stable and highly maneuverable feet work in a coordinated manner on the move as seen in Figure 4. It can be recognized that the C-shaped leg has more effective lifting and pulling forces than the other two. The circular shape of the leg is the one that performs the mobility most efficiently.
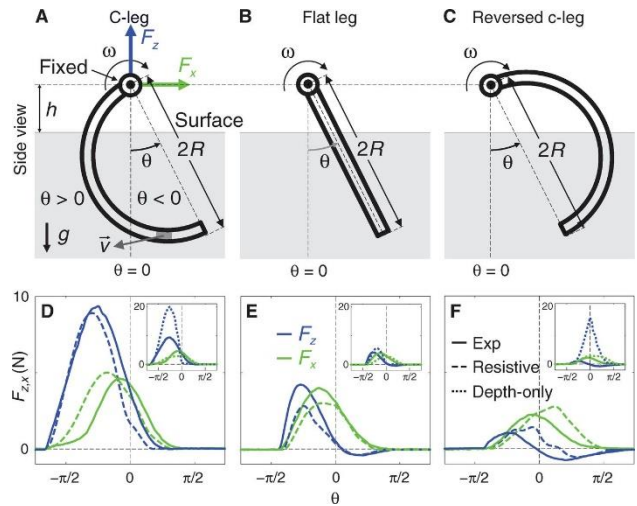
The straight leg has the optimal lift only at the start of contact and the optimal drag in the vertical position. In this paper, the vehicle consists of six C-shaped legs. The vehicle is always in contact with the ground for three feet during the movement [14].

In order to prevent the vehicle from tipping during movement, it is necessary to have 3 legs on the ground during the movement. This is because a plane passes through three points. Six legs of the vehicle were divided into two groups. The numbering of legs has been presented with Figure 5.

The movement of the legs from the first point to the second point moves the vehicle forward. In order to continue the movement of the vehicle on rough terrain, the operation mode of the engine is determined as Step 16 during the movement of the legs from the first point to the second point. Since the time from the first point to the second point must be equal to the time from the second point to the first point, the mode of operation of the motors must be selected for the second point to the first point.
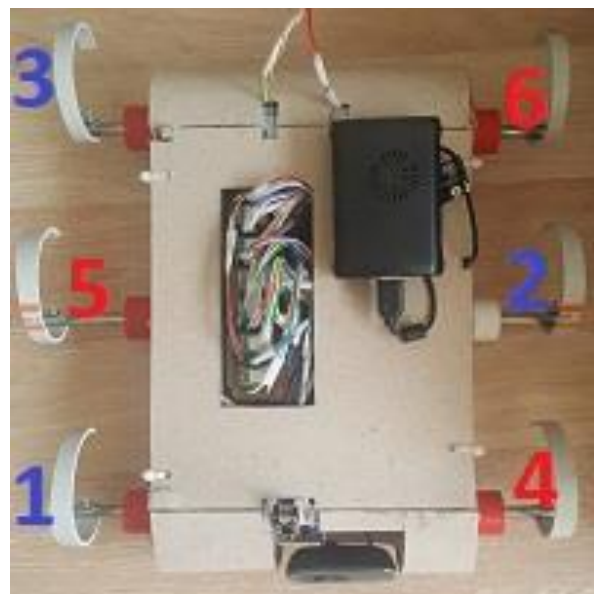
Figure 5. Numbering of legs

Table 1. Features of Step Motor Operation Modes

Micro Resolution	Pulse Required for a Tour	Speed
Full Step	200	16V
Half Step	400	8V
Quarter Step	800	4V
Eight Step	1600	2V
Sixteen Step	3200	V

As seen in Figure 6 and Figure 7, the movement of leg from one point to another moves the vehicle forward. For a continued movement of vehicle on a rough terrain, the operating mode of motor was determined to be 16th step during the legs' movement from one point to another point. Operating mode features of step motor are presented at Table 1.

Since the arrival duration from point 1 to point 2 must be equal to the arrival duration from point 2 to point 1, operating mode of motors has been set as quarter step for the move from point 2 to point 1. This means the duration of the legs' A and B movement in Figure 6 is same. The angle of these movements can be calculated as in Equation (1), (2), (3) and (4).

$$A = V * t \rightarrow X = K \tag{1}$$

$$A = 4V * t \rightarrow Y = 4K \tag{2}$$

$$X + Y = 360° \rightarrow 5K = 360° \rightarrow K = 72° \tag{3}$$

$$X = 72° , Y = 228° \tag{4}$$

The duration 't' can be calculated by the pulse required for a tour in Table 1. Equation (5), (6) and (7) shows the calculation of the movement duration.

$$1 \ pulse = 1ms \tag{5}$$

$$A = \frac{3200}{5} pulse = 640 \ pulse \tag{6}$$

$$640 \ pulse = 0.64 \ s \rightarrow t = 0.64s \tag{7}$$

Displacement of the leg of the can be calculated with radius of the leg as in Equation (8) and (9).

$$r = 7 \ cm, \qquad A + B = 2 * \pi * r \tag{8}$$

$$A + B = 0.2512 \ m \tag{9}$$

The velocity of the movement can be calculated with duration and the displacement as in Equation (10), (11) and (12).

$$A = V * t , B = 4V * t \tag{10}$$

$$A + B = 5V * t = 0.2512 \ m \tag{11}$$

$$V = 0.0785 \ m/s \tag{12}$$

The robot operates two groups of legs synchronized with each other so that the height of the trunk can remain constant while moving.

Figure 6. Angle of step

Figure 7. Angle of step motion
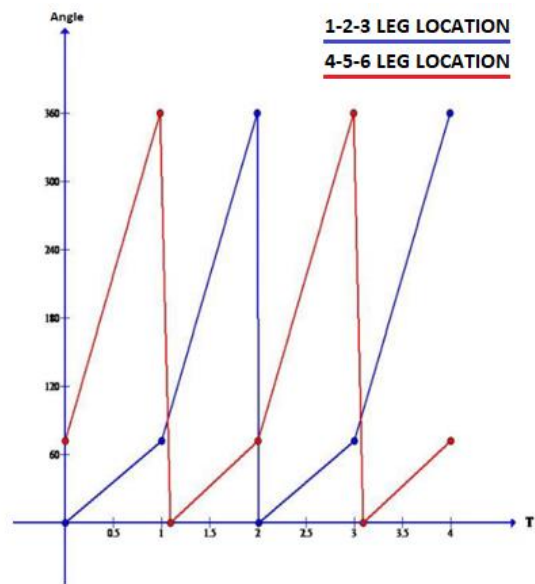
Figure 8. Leg angle position vs Time
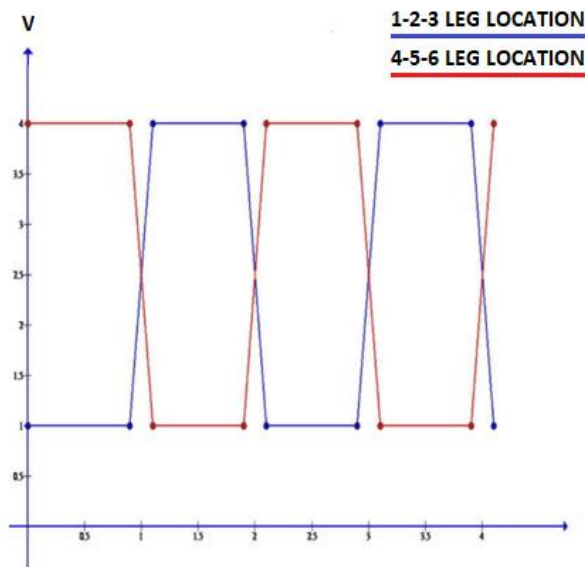
Figure 9. Speed vs Time

The first group consists of legs 1, 2 and 3, the second group consists of legs 4, 5 and 6. Initially, the position of the legs in the first group is 0 degrees and the position of the legs in the second group is 72 degrees.

As shown in Figure 8, while first group of legs move from 0 degrees to 72 degrees, second group of legs move from 72 degrees to 360 degrees at the same time.

Figure 9 shows the speed of the leg groups. While first group of legs moves with 0.0785 m/s, the second group of legs moves with 0.314 m/s. In the second part of the motion, while first group of legs moves with 0.314 m/s, the second group of legs moves with 0.0785 m/s. During the 0 - 2t (1.28s) duration, all the legs of the vehicle take a full turn.

2.3 Software Design

By pressing any button on the control, information is entered to the previously selected pin of Arduino-Nano. With this incoming information, Arduino-Nano generates 8-bit data due to previously installed program. This generated data is sent to the robot unit via the transmitter NRF24101 connected to Arduino-Nano. This data is received by the receiver NRF24101, which is connected to Arduino Uno in the robot unit. The received data is converted to three-bit data by previously installed program in Arduino Uno. Arduino Uno transmits these three bits of data to Arduino Mega via serial communication. If one of the step motor movement buttons on the controller is pressed, program in the Arduino Mega processes the incoming data and sends the direction and speed information to the drivers. If one of the camera position buttons on the controller is pressed, program sends the angle information to the servo motor. This provides control of the camera motion.

2.4 Electronic Design

In this paper, Arduino Mega, Arduino Uno, Arduino Nano, NRF24101, Raspberry Pi 3, A4988 driver card were used electronically. The layout of the electronical components and wiring diagram are shown in Figure 10.

2.5 Communication Design

The communication between Arduino Nano and Arduino Uno is provided by NRF24101 module. In the transmitter section, first a channel is selected to send data and communicate. Once the channel is defined, NRF24101 module is set to transmit. After making the adjustments, data is sent to the receiver on the other side with NRF24101 module when the button is pressed.

In the receiver section, the channel is selected same as the transmitter part. After defining the channel, the NRF module on the receiver is set to read. The module constantly checks to see if any data has been received. When a data arrives, it checks whether the incoming data is received beforehand. After the mechanical, electronic and software design of the robot was completed, experiments were carried out to move the robot steadily. In these experiments, it was aimed to move the robot legs at different speeds simultaneously and move the robot without falling and damaging itself.

The calculated speed values are sent from the microcontroller via analog input to ensure that the motor goes at the desired speed. The microcontroller can be supplied as predictive and sliding [15-17]. Before the robot started to move, an initial position was determined to ensure the simultaneous movement of the motors and the measurement of the positions of the motors.

These start positions were reported to the microcontroller via limit switches. Figure 11 shows the position of the robot before moving on the ground. As the robot started to move, it stands up on six legs as in Figure 12 and waits for the speed information to be applied to the motors in a position ready to walk.

Experiments were carried out at different speeds in order to ensure a stable movement of the robot. While three motors were programmed to complete its revolution, the other three motors completed their revolution slowly. In this way, the robot's feet were never cut off from the ground, remained stable and smooth movement was ensured.

The simultaneous operation of the motors was the most challenging problem during the experiments. Other encountered problems were very slow movement of the system in low speed and motor's inability to provide enough torque at high speeds. Despite these situations, the robot can move in a balanced way.

After the installation of the system, the test drive was carried out. Forward-backward, right-left movements were

carried out. The robot fulfilled its functions without any problems. Image acquisition and control of the camera were tested instantaneously. System process is presented at Figure 13 in detail.
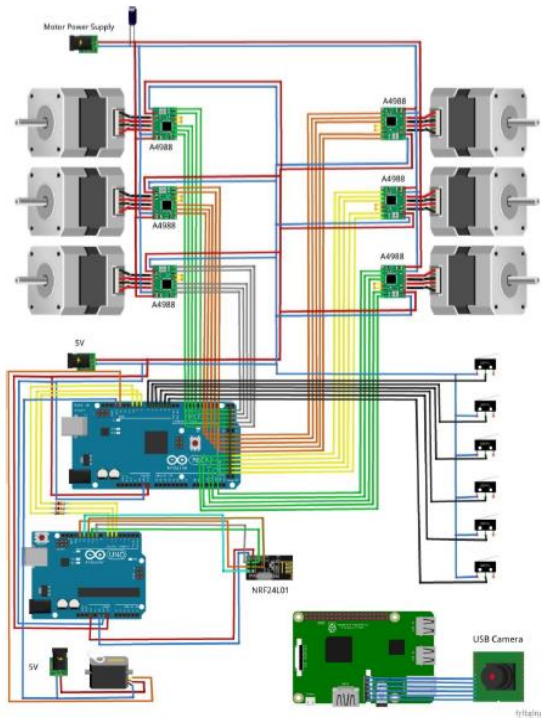
Figure 10. The layout and the wiring diagram of the electronic components
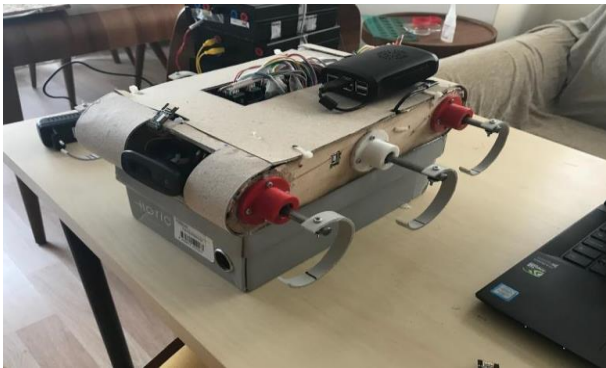
Figure 11. Position of the robot
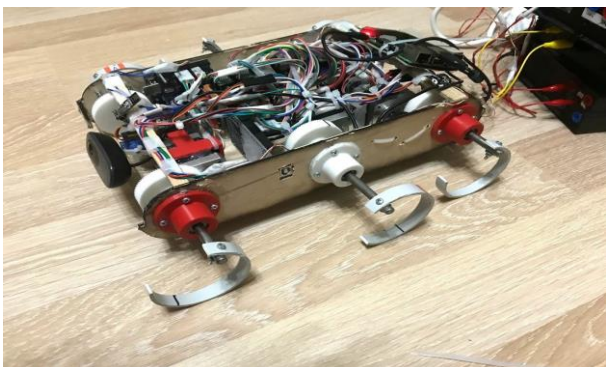
Figure 12. The motors in a position ready to walk
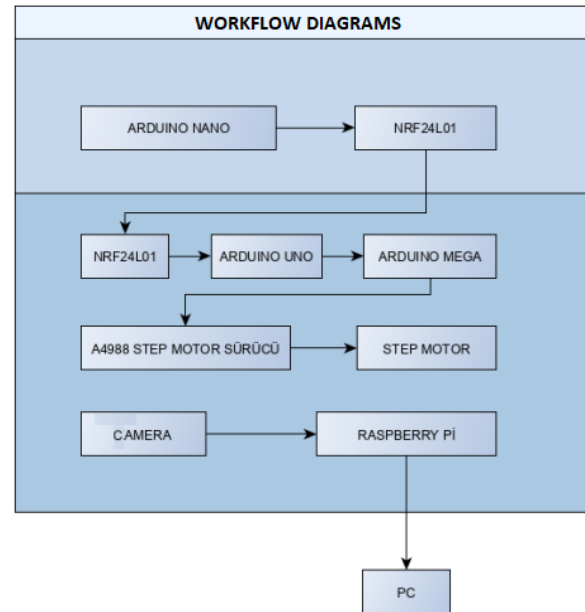
Figure 13. System Process

3. Conclusions

Robots have been a strategic element of today's technology. Multiple-leg robots and mechanisms that could perceive, ratiocinate, decide and move in line with that decision are fundamental tools of contemporary automation technology that are used for different purposes such as spatial studies, detecting the information of living creatures as a result of natural catastrophes (i.e. earthquake), explosive ordnance disposal, fight against terrorism as well as in various fields such as mining, defense industry and medicine. The most important of all is the successful implementation of the commanded functions by robots. This success depends on designing a mechanism to facilitate the control of the robot as well as a model to minimize energy consumption and with a self-evaluation capacity.

In this study, mechanical and electronic design of six-legged robot capable of moving on uneven ground was realized. The six-legged robot was placed with three legs on the right and three legs on the left. The motors were operated simultaneously to allow the robot to move evenly. Thanks to its leg structure, it was aimed to travel in land conditions. Image control was provided on the computer with the camera placed on the robot. In this study, the program written into the electronic cards run the motors simultaneously.

The control circuit designed for the project is controlled by the vehicle. Arduino Uno collects and sends the commands sent from the control circuit to the Arduino Mega for the vehicle to perform the required commands.

The program written in Arduino IDE sends direction and step information to the stepper motor driver in response to the corresponding commands. Via a defined IP

address, the image obtained by the camera on the vehicle is transferred to the computer instantly by computer or telephone.

In future work, it is aimed for the robot to perform tasks such as climbing stairs and overcoming obstacles with the development of power unit and motor capacity. In addition, the vehicle is intended to be coated with carbon fiber in order to increase the strength.

Declaration

The author(s) declared no potential conflicts of interest with respect to the research, authorship, and/or publication of this article. The author(s) also declared that this article is original, was prepared in accordance with international publication and research ethics, and ethical committee permission or any special permission is not required.

References

1. Jennings, J., S. Whelan, G. Evans, W., F. *Cooperative search and rescue with a team of mobile robots.* IEEE 8th Int. Conf. on Advanced Robotics, Monterey, 1997, California, U.S.A., p. 93.

2. Galloway, K., C. Haynes G., C. Ilhan, B., D. Johnson A., M. Knoph, R. Lynch, G., A., Plotnick B., N. White, M. and Kodistchek D., E. *X-RHex: A highly mobile hexapedal robot for sensorimotor tasks.* University of Pennsylvania - Technical Reports, U.S.A. 2010, p. 3-7.

3. Ersoy S., Görgülü S. *Computer Based Education and Progress Alternative For Electro Mechanics Lesson.* Acta Mechanica et Automatica, 2009, p. 6-32.

4. Glasius, R. Andrzej, K. and Stan, G. *Neural network dynamics for path planning and obstacle avoidance.* Neural Networks, 1995, **8**(1): p. 125-133.

5. Ma Z., Q. and Yuan, Z., R. *Real-time navigation and obstacle avoidance based on grids method for fast mobile robot.*,2014. Seul, Korea, p. 91-95.

6. Henry, P. Krainin, M. Herbst, E. Ren, X. and Fox, D. *RGB-D mapping: Using depth cameras for dense 3D modeling of indoor environments.*2014. Delhi, India, p. 477-491.

7. Yalcin, M.K., Ersoy, E. *Designing autopilot system for fixed-wing flight mode of a tilt-rotor UAV in a virtual environment: X-Plane.* International Advanced Researches and Engineering Journal, 2018. **2**(1): p. 33-42.

8. Saranli, U. Buehler, M. and Koditschek, D.,E. *Rhex: A simple and highly mobile hexapod robot.* The Int. Journal of Robotics Research, 2001. **20**: p. 616-631.

9. Berns, K. Kepplin, V. Ilg, W. and Dillmann, R. Experiments with a stereo camera head for the local navigation of LAURON II, Forschungszentrum Informatik Karlsruhe, Germany, 1993.

10. RHex Robot Platform. [cited 2019 June 19]; Available from: http://www.rhex.web.tr/.

11. Altendorfer, R. Moore, N. Komsuoğlu, H. Buehler, M. Brown Jr. H., B., McMordie, D. Saranlı, U. Full R., J.and D. E. Koditschek. RHex: *A biologically inspired hexapod runner. Autonomous Robots,* 2001. **11**(3): p. 207-213.

12. Greenfield, A. Saranli, U. and Rizzi, A., A. *Solving models of controlled dynamic planar rigid-body systems with frictional contact.* International Journal of Robotics Research, 2005. **24**(11): p. 911-931.

13. Skaff, S. Rizzi, A. Choset, H. Lin. P., C. *Context-Based State Estimation Technique for Hybrid Systems.* Barcelona, Spain 2005. p 3935-3940.

14. Li, C. Zhang, T. and Goldman, D., I. *A Terradynamics of Legged Locomotion on Granular Media*, Science, 2013. **339** (6126) p. 1408-1412.

15. Jacko P. Kravets, O. *Spectral Analysis by STM32 Microcontroller of the Mixed Signal.* IEEE International Conference on Modern Electrical and Energy Systems. Kremenchuk, Ukraine, 2019. p 342-345.

16. Mao WL. Liu G.R. Chu C.T. Hung CW. *Microcontroller-Based Speed Control Using Sliding Mode Control in Synchronize Reluctance Motor.* Advances in Intelligent Systems and Computing, 2019

17. Chaber P. Ławryńczuk, M. *Fast Analytical Model Predictive Controllers and Their Implementation for STM32 ARM Microcontroller.* IEEE Transactions on Industrial Informatics, 2019. p. 4580-4590.

18. Summary of the RHex robot platform. [cited 2019 10 June]; Available from: https://www.rhex.web.tr.

Research Article

Thermodynamic performance analysis of geothermal and solar energy assisted power generation and residential cooling system

Ozan Sen [a],* and Ceyhun Yilmaz [a]

[a]Department of Mechanical Engineering, Afyon Kocatepe University, Technology Faculty, Afyonkarahisar, Turkey

ARTICLE INFO	ABSTRACT
	In this study, geothermal and solar assisted cogeneration system is modeled to the supply of electricity and cooling. The energy requirements of Afyon Kocatepe University, Faculty of Technology building, are investigated. The building cooling system is performed by using heat energy provided from geothermal and solar energy in an absorption cooling system. Subsequently, it is aimed to generate electricity in the Organic Rankine Cycle (ORC) with geothermal water and waste heat leaving the cycle. It is planned that the electricity produced in the power cycle is supplied to the grid system according to the requirement. The cooling load of the faculty building is calculated by considering the working conditions of the faculty building. The ideal thermodynamic analysis and performance evaluation of the system has been performed by using Engineering Equation Solver (EES) software into consideration by considering the cooling season, geothermal and solar energy data of Afyon in the summer season. The parametric study of the system is performed by considering different geothermal water temperature and solar radiation. The reversible COP of the absorption cooling system is calculated to be 3.18. The maximum heat energy value obtained from solar energy is calculated to be 74.97 kW in June. The highest ideal cooling capacity and maximum power provided from geothermal and solar assisted cogeneration energy systems are calculated to be 40,222 kW and 4688 kW, respectively, in June. These results are sufficient to supply the electrical and cooling requirements of the faculty building.

1. Introduction

In the industrial application, energy is the most important material to solve the problem of requirements. Especially developing counties need too much energy consumption that machines work with consumed in industrial applications. For that reason, this problem should be solved by alternative energy resources. Currently, the most commonly used energy resources are the fossil-based energy sources in the world. These conditions bring with some problems. Some of these are the depletion of fossil fuels, the harmful effect on the environment, and human health. Two methods are used to reduce the harmful effects of fossil fuel emissions. One is to improve the technology of energy conversion systems and fuels better combustion occurs, and fewer emissions are produced. The second method is the alternative energy resources. For instance, this issue has led us to

alternative energy sources, which are renewable and sustainable energies. Today, the best-known alternative energy sources are renewable energy sources in which wind, solar, hydro, geothermal, and biomass are the most common. Produced renewable electricity must be economically competitive level with against fossil-based energy resources [1].

Renewable energies are currently the fastest-growing energy source in the world. Depletion and emission concerns over fossil fuel use and increasing government incentives can cause even higher growth in the use of renewable sources in the coming decades. An energy source is called renewable if it can be renewed and sustained without any depletion and any significant effect on the environment. It is also called alternative, sustainable, or a green energy source. Fossil fuels such as coal, oil, and natural gas, on the other hand, are not

renewable, and they are depleted by use. They also emit harmful pollutants and greenhouse gases. Primary renewable energy sources include solar, wind, hydro, biomass, and geothermal. Energies from the ocean, including wave and tidal energies, are also renewable sources, but they are currently not economical, and the technologies are still in the experimental and developmental stages [2].

The best-known renewable source is solar energy. Although solar energy is sufficient to meet the entire energy needs of the world, currently, it is not used as extensively as fossil fuels because of the low concentration of solar energy on earth and the relatively high capital cost of harnessing it. Another most popular renewable energy source is geothermal energy. Geothermal energy refers to the heat of the earth. High temperature underground geothermal fluid found in some locations is extracted, and the energy of the geothermal fluid is converted to electricity or heat. Geothermal energy conversion is one of the most mature renewable energy technologies. Geothermal energy is mostly used for electricity generation and district heating. Especially Afyon province has great potential in terms of geothermal and solar energy sources. In this study, the potential for efficient use and alternative methods will be investigated [3].

There are many studies in the literature on the use of renewable energy sources such as solar and wind indirect electricity generation or the production of electricity and cooling using geothermal energy. However, studies on the use of geothermal or solar energy in cogeneration energy systems for electricity generation and cooling are limited. In this section, some of the most important of these studies, and some studies about the method to be followed will be mentioned. Zhou et al. [4] of the hybrid solar-geothermal power plant, to increase electricity production and to reduce the effect of daily temperature are researched. For this purpose, they compared the performance of hybrid systems in terms of power output and electricity cost to independent solar and geothermal power plants. As a result of thermodynamic analysis of 120°C source temperature and 50 kg/h geothermal water, they stated that a hybrid plant performs better than a geothermal plant alone. Ezzat et al. [5] have designed a multi-generation energy system supported by geothermal energy and solar energy. In this system, they designed, they aimed to produce electricity, cooling for industry, heating for houses, and hot water for domestic use. They calculated the energy and exergy COP values of the absorption refrigerant and heat pump and the maximum exergy loss in the solar collectors. As a result of their research, they stated that the energy efficiency of the multi-generation energy system is about five times better than the energy efficiency of the basic geothermal

system. Astolfi et al. [6] performed performance and cost analysis of a hybrid solar-geothermal power plant based on the Organic Rankine Cycle (ORC). They performed their research for the regions located in four different cities and estimated the annual net power obtained from the hybrid system with hourly simulation they created in MATLAB program for each region. As a result of their studies, they emphasized that the hybrid solar-geothermal energy system can generate electricity at a lower cost than an independent solar power plant. Yılmaz et al. [7] performed thermodynamic modeling and analysis of the geothermal energy-assisted ammonia-water absorption cooling system. They investigated the coefficient of performance (COP) and exergy efficiency of the modeled system, and they examined the effect of geothermal source temperature change on these important parameters. They calculated the lowest cooling temperature and cooling heat load of the system. Also, they observed how the performance parameters of the system changed with the change of the temperature of the geothermal resource used by performing parametric studies. Yakut et al. [8] investigated to air-condition a meeting room for 30 people in Isparta with an absorption system using LiBr-water as a fluid pair. They calculated the working conditions and cooling loads of the air conditioning system according to months. They calculated the useful temperatures and collector efficiencies obtained in planar solar collectors for each month. As a result of their research, they have reached the number of the solar collector to provide the necessary heat energy. Kuyumcu et al. [9] proposed to cool an apartment using an absorption cooling machine using a single-acting solar-assisted H2O-LiBr mixture. The cooling energy requirement that they calculate in order to maintain the desired constant indoor temperature in the rooms, they supplied from solar energy through the collectors of absorption the cooling system. They calculated the required collector surface area by considering different types of collectors according to the cooling energy demand of the apartment. Bilgic et al. [10] have performed an artificial neural network using temperature and mass flow data from an experimental Organic Rankine Cycle (ORC). They compared the experimental results and the forecasting results by making power estimation with artificial neural networks (ANN) trained for a 10 kW Organic Rankine Cycle (ORC). As a result of the study, they compared the estimation values obtained from artificial neural networks with the experimental data and calculated the correlation coefficient indicating the performance of the prediction as 0.99124. As a result, they emphasized that power parameters can be calculated by adjusting system parameters according to artificial neural networks. Yagli et al. [11] designed a subcritical and supercritical Organic

Rankine Cycle (ORC) to recover the exhaust gas waste heat of biogas fuelled combined heat and power (CHP) engine. They improved the system parameters as net power, mass flow rate, pump total power consumption, thermal efficiency, and exergy efficiency by changing turbine inlet temperature and pressure. They stated that compared with subcritical ORC, supercritical ORC better performance. Beneta et al. [12] proposed a new combined cooling, heating, and power system (CCHP) driven by solar energy. They worked on a system of Organic Rankine Cycle (ORC) to generate electricity, cooling, and heating, respectively. In their study, they examined the effects of some critical thermodynamic parameters on the performance of the cycle. Yılmaz [13] designed a system to produce clean hydrogen, power, heating, cooling, and freshwater as a multigenerational purpose. Its system consisted of a solar heliostat, a Brayton cycle driven by solar energy, a Rankine cycle, an Organic Rankine Cycle, an absorption cooling and heating system, a flash desalting unit, and a PEM electrolyzer. In his study carried out parametric studies to investigate the effects of different parameters such as turbine inlet pressure, solar radiation, an isentropic efficiency of the compressor, and reference temperature on system efficiency. Zhao et al. [14] worked on a system driven by solar energy consisting of an Organic Rankine Cycle (ORC) and a parabolic trough collector to generate power, cooling, and heating. In their work, they conducted a comprehensive analysis of the influence of configurations of solar-driven ORC based CCHP systems. They stated that, under reasonable thermodynamic boundary conditions, optimal operational

parameters were obtained with ORC 200 kW.

In this study, modeling geothermal and solar assisted cogeneration systems to supply the electricity and cooling requirements of buildings is investigated. Residential cooling is performed by using heat provided from geothermal and solar energy in an absorption cooling system. Subsequently, it is provided to generate electricity in the Organic Rankine Cycle (ORC) with geothermal water and waste heat leaving the cycle. It is objected that the electricity produced in the power cycle is supplied to the grid according to the requirement. The cogeneration system can be supplied to the cooling and electricity requirements of the buildings.

2. Material and Method

2.1 Description of System

In this study, geothermal and solar energy assisted cogeneration energy system has been modeled to supply the electricity and cooling requirements of Afyon Kocatepe University, Faculty of Technology building with 1000 m^2 area. The overview of the multi-power generation plant system is given in Fig. 1.

The working principle of the system modeled to supply the electricity and cooling requirements of the faculty building is as follows; beneficial heat energy provided from geothermal and solar energy by using in the absorption cooling cycle has cooled the building. Geothermal fluid and waste heat energy leaving the cycle is used to generate electricity in the Organic Rankine Cycle (ORC). The electricity generated in the power cycle is supplied to the grid according to the requirement.
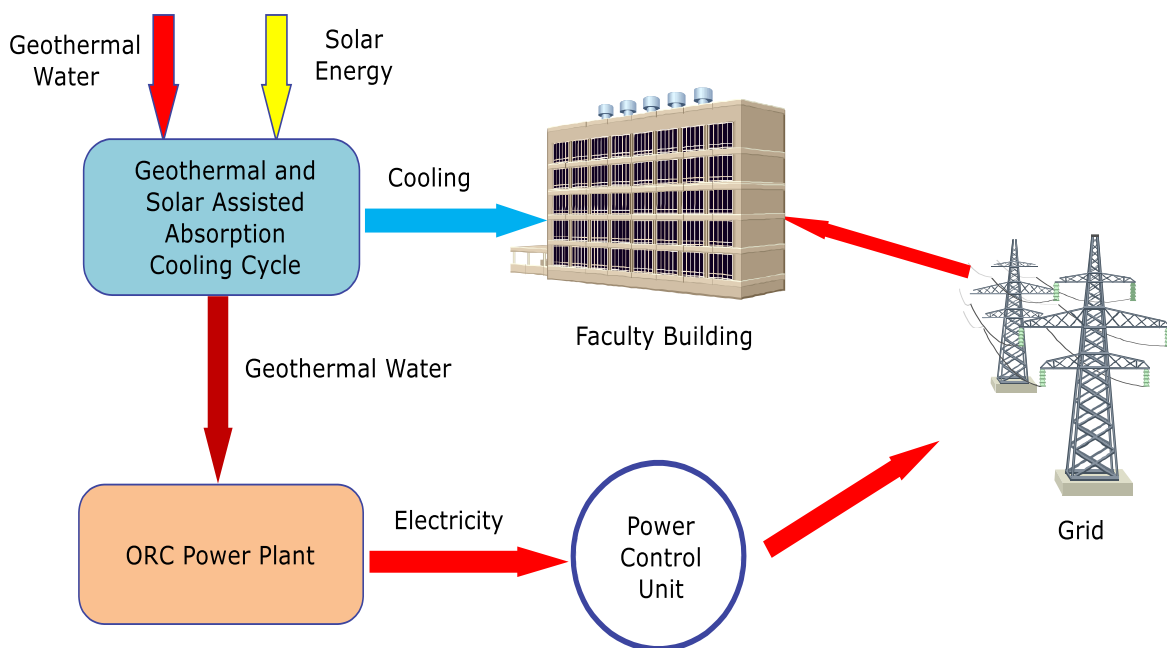

Figure 1. Geothermal and solar energy assisted cogeneration system

2.2 Modeling of System

The geothermal and solar energy assisted cogeneration energy system is modeled in this section. The cooling load of a building represents the heat that must be removed from the interior of a building to maintain it at the desired conditions. The cooling load is determined with a steady-state analysis using the design conditions for the indoors and the outdoors to size the cooling system [15]. In order to supply the total cooling load demanded the building, firstly, the ideal cooling capacity of a single geothermal energy-assisted absorption cooling cycle is calculated. In the geothermal and solar energy assisted absorption cooling cycle, geothermal water enters the cycle at 110ºC at a rate of 150 kg/s and leaves the cycle at 90ºC.

A flat-plate solar collector is considered for solar energy, the other primary source of the system. The objective of a flat-plate solar collector is to produce useful heat from solar energy. The flat-plate solar collector consists of glazing, an absorber plate, flow tubes, insulation, glazing frame, and a box enclosure. The efficiency of the flat plate solar collector is supposed as %60 [16]. For June, July, and August, where the space cooling is planned, the amount of solar radiation and the required collector surface areas are calculated, and the thermal energies generated by the solar energy are obtained. With the addition of the amount of thermal energy supplied from the solar energy, the ideal cooling loads of the cogeneration energy system are calculated in the summer months. When solar energy is included in the system, changes in the ideal cooling capacities of the cogeneration system are examined. The Organic Rankine Cycle (ORC) is selected for the power plant because the geothermal field of the region has low-temperature scale fields. In the Organic Rankine Cycle, geothermal water enters the cycle at 90ºC at a rate of 150 kg/s and leaves the cycle at 70ºC. R134a as the working fluid is selected.

2.3 Thermodynamic Analysis of System

In order to maintain the desired ambient temperature constant for each room in the faculty building, the total cooling thermal load of the building must be supplied in summer conditions. Considering the desired design conditions for the rooms, the total cooling thermal load of the building can be determined by the following equation [15].

$$Q_{building} = Q_{room} \times Z + Q_s + Q_{human} + Q_{device} \quad (1)$$

Here Q_{room} is the non-incremental heat gain for the rooms, Z is the combined increment coefficient, Q_s is the air leak heat gain, Q_{human} is the heat gain from humans, and Q_{device} is the heat gain from the devices.

The thermal energy provided from geothermal energy is calculated as follows [16].

$$Q_{geo} = \dot{m}(h_1 - h_2) \quad (2)$$

Where $\dot{m}$ the mass is flow of the geothermal fluid, h_1 and h_2 are the enthalpy values of the inlet and outlet temperatures of the geothermal fluid.

The ideal efficiency coefficient of the geothermal energy assisted absorption cooling system is as follows [16].

$$COP_{abs,rev} = \left(1 - \frac{T_0}{T_S}\right)\left(\frac{T_L}{T_0 - T_L}\right) \quad (3)$$

Here T_0 is the environmental temperature, T_S is the resource temperature and T_L is the desired ambient temperature [16].

$$COP_{abs,rev} = \frac{Q_L}{Q_{geo}} \quad (4)$$

Here Q_L is the ideal cooling capacity of the system.

The maximum work that can be obtained from a liquid geothermal source with a temperature T_S is calculated by the following equation [16].

$$w_{rev,out,geo} = c(T_S - T_0) - T_0 c \ln\left(\frac{T_S}{T_0}\right) \quad (5)$$

The surface area of the collector is calculated as follows [15].

$$A_c = \frac{Q_{required}}{Q_{useful}} \quad (6)$$

Here the useful heat obtained for the unit collector surface area Q_{useful} is the thermal load required for the hot water required $Q_{required}$.

Useful heat is calculated as follows [15].

$$Q_{useful} = H_T \times \eta_{col} \times \eta_m \quad (7)$$

Here H_T is the average monthly solar radiation per collector unit area, η_{col} is collector efficiency and η_m is collector system efficiency.

The required thermal load is determined as follows [15].

$$Q_{required} = \dot{m}c_p(T_w - T_m) \quad (8)$$

Here, $\dot{m}$ is the amount of hot water, c_p is the specific heat of the water, T_w is the desired minimum water temperature, T_m and is the mains water temperature.

The total solar radiation falling on the horizontal surface is calculated as follows [15].

$$I = r_t \times H \quad (9)$$

Here r_t is the ratio of the instantaneous total solar radiation falling on the horizontal surface I to the total daily solar radiation falling on the horizontal surface H. The thermal energy provided from solar energy is calculated as follows [15].

$$Q_{sol} = I \times A_c \qquad (10)$$

3. Result and Discussion

In this study, the geothermal and solar assisted cogeneration energy system of a faculty building is investigated by considering geothermal and solar data of Afyon province. The necessary calculations for the electricity and cooling requirements of the building are obtained by using the EES program. The average outside air temperatures of Afyon province for the 3 months planned to cool the faculty building is shown in Table 1. Sunlight intensity of Afyon province for three months is shown in Table 2. In other months, it is considered that the faculty building is not require cooling. As seen in Table 3, the maximum instantaneous solar radiation intensity is calculated as 640.44 W/m^2 in July.

After the determination of these values, the heat energy values produced by solar energy are obtained. The comparison of the heat energy provided from the solar energy and the total solar radiation values for the 3-month period in which the space cooling is performed is shown in Fig. 2. As shown in Fig. 2, although the maximum instantaneous solar radiation is calculated in July (640.44 W/m2), the heat energy provided from solar energy (71.04 kW) is calculated to be a lower value than the heat energy obtained in other months. The main reason for this situation is that the collector area required in July is less than the other months. In Fig. 3 is shown how a change in the ideal cooling capacity of the system by integrating solar energy into a system operating with geothermal energy.

As shown in Fig. 3, the addition of solar energy to a system operating with geothermal energy has resulted in a significant increase in the ideal cooling capacity of the system during the summer months. The obtained ideal cooling capacity values indicate that the total amount of energy required for cooling the faculty building (125 kW) can be easily supplied. Fig. 4 shows the ideal cooling capacity and maximum power values provided from the geothermal and solar assisted cogeneration energy system in June, July, and August.

Table 1. Monthly average outside air temperatures in Afyon [17]

Months	Average Outside Air Temperatures (°C)
June	19,0
July	21,9
August	21,5

Table 2. Monthly average sunlight intensity in Afyon [18]

Months	Average Sunlight Intensity (kJ/m^2)
June	23880
July	24271
August	22297

Table 3. Instantaneous solar radiation and required collector fields [18]

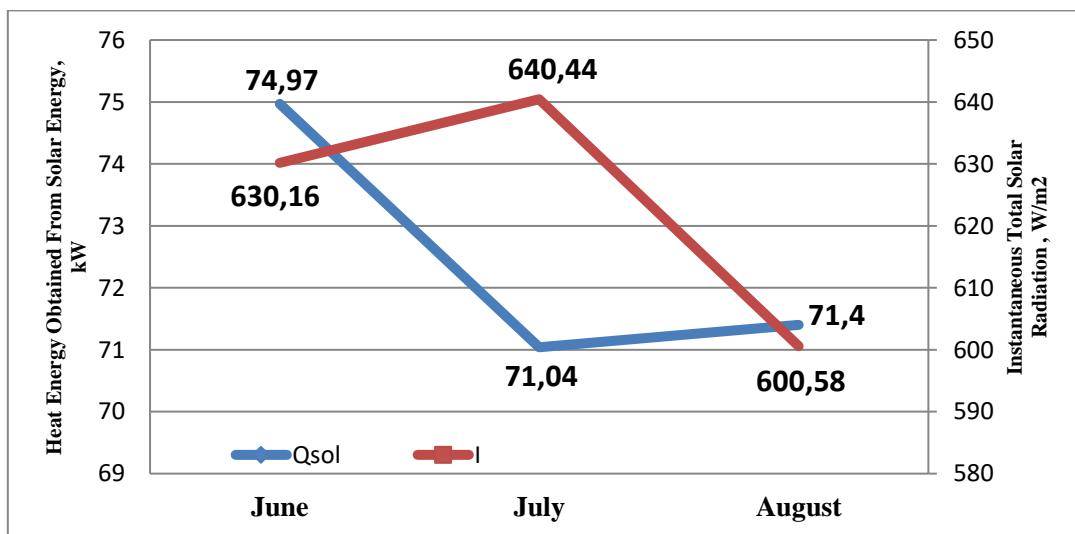| Months	Solar Radiation (W/m^2)	Required Collector Field (m^2)
June	630,16	119
July	640,44	111
August	600,58	119

Figure 2. Heat energy provided from solar energy and instantaneous total solar radiation
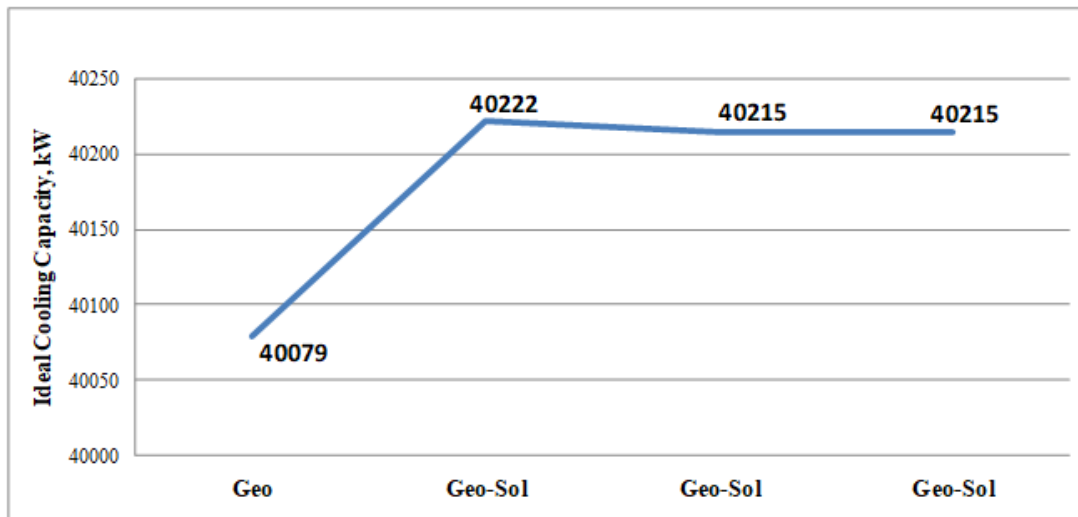
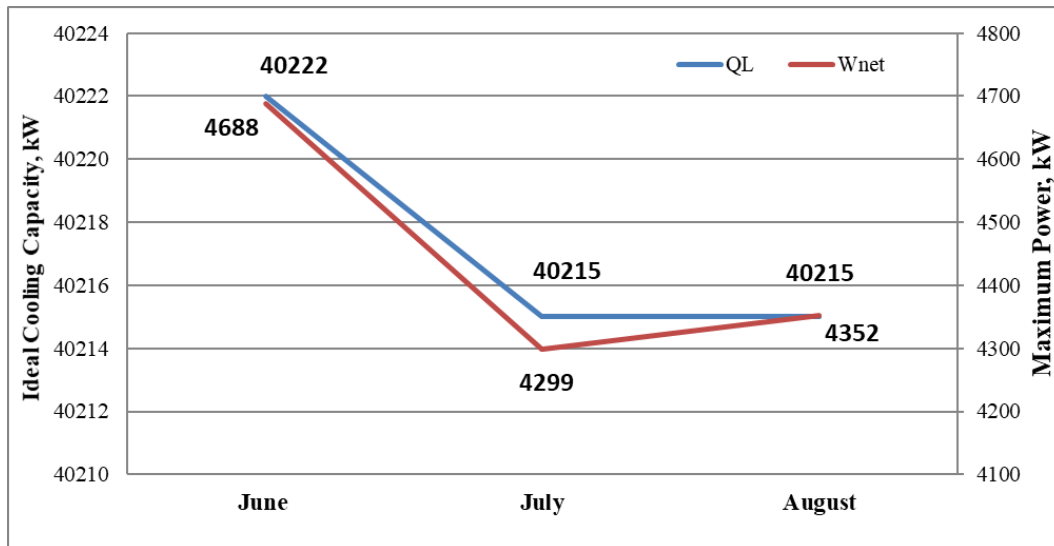Figure 3. Variation of system ideal cooling capacity

Figure 4. Ideal cooling capacity and maximum power values provided from the system

As shown in Fig. 4, the highest ideal cooling capacity value (40,222 kW) and maximum power value (4688 kW) provided from geothermal and solar assisted cogeneration energy system are calculated in June. These results are sufficient to supply the electrical and cooling requirements of the faculty building.

4. Conclusions

Today, with the gain acceleration of industrialization, energy plays a significant role in the world economy. Sustainable energy production and efficient use of this energy have reached a critical level that will affect the whole world. Therefore, in order to supply the increasing energy demand, the whole world has focused its attention on clean energy. As explained by scientific sources, the damages of fossil fuels to the environment are a valid concern. Geothermal energy,

which is one of the renewable energy sources, is the subject of many kinds of research, and it is one of the sustainable energy sources of the future. In that case, technical and economic problems in energy and heat generation should be solved. There are various methods used in the power generation of these systems, and they require electricity and heat inputs from geothermal sources. In this study, the geothermal and solar energy potential of the Afyon province has been investigated. The region has a productive potential in terms of geothermal energy. Afyon province sunshine duration is higher than the average in Turkey. Although it has a very high potential in terms of solar energy, it is seen that the studies related to the utilization of this energy are not sufficient yet. In Afyon province, the conversion of renewable energy sources to energy the expansion of investments related and the realization of new investments will make a significant contribution to

the energy of the region. The number of companies investing in bioenergy, wind energy, and geothermal energy should be increased.

Declaration

Acknowledgment

References

1. Yilmaz, C., *Thermodynamic and economic investigation of geothermal powered absorption cooling system for buildings.* Geothermics, 2017. **70**: p. 239-248.

2. Shahin, M. S., M. F. Orhan and F. Uygul, *Thermodynamic analysis of parabolic trough and heliostat field solar collectors integrated with a Rankine cycle for cogeneration of electricity and heat.* Solar Energy, 2016. **136**: p. 183-196.

3. Li, Y. and Y. Yang, *Thermodynamic analysis of a novel integrated solar combined cycle.* Applied energy, 2014. **122**: p. 133-142.

4. Zhou, C., E. Doroodchi and B. Moghtaderi, *An in-depth assessment of hybrid solar–geothermal power generation.* Energy Conversion and Management, 2013. **74**: p. 88-101.

5. Ezzat, M. F., I. Dıncer, *Energy and exergy analyses of a new geothermal–solar energy based system.* Solar Energy, 2016. **134**: p. 95-106.

6. Astolfi, M., L. Xodo, M. C. Romano and E. Macchi, *Technical and economical analysis of a solar–geothermal hybrid plant based on an organic rankine cycle.* Geothermics, 2011. **40**(1): p. 58-68.

7. Kanoglu, M., C. Yilmaz and A. Abusoglu, *Geothermal energy use in absorption precooling for Claude hydrogen liquefaction cycle.* International Journal of Hydrogen Energy, 2016. **41**(26): p. 11185-11200.

8. Yakut, A. K., A. Şencan, R. Selbaş, E. Dikmen, B. Görgülü, İ. Dostuçok and S. Kutlu, *Güneş enerjisi destekli absorbsiyonlu soğutma sisteminin termodinamik incelenmesi.* Soğutma Dünyası, 2013. **16**(60): p. 76-81.

9. Kuyumcu, M. E., H. E. Şahin, R. Yumrutaş and M. İmal, *Kahramanmaraş kentinde güneş enerjisi destekli absorpsiyonlu soğutma sistemi kullanılarak bir apartman dairesinin soğutulması.* Kahramanmaras SutcuImam University Journal of Engineering Sciences, 2015. **18**(2): p. 25-32.

10. Bilgiç, H. H., H. Yağlı, A. Koç, and, A. Yapıcı, *Deneysel bir organik rankine çevriminde yapay sinir ağları (ysa) yardımıyla güç tahmini.* Selçuk Üniversitesi Mühendislik, Bilim Ve Teknoloji Dergisi, 2016. **4**(1): p. 7-17.

11. Yağlı, H., Y. Koç, A. Koç, A. Görgülü and A. Tandiroğlu, *Parametric optimization and exergetic analysis comparison of subcritical and supercritical organic Rankine cycle (ORC) for biogas fuelled combined heat and power (CHP) engine exhaust gas waste heat.* Energy, 2016. **111**: p. 923-932.

12. Eisavi, B., S. Khalilarya, A. Chitsaz and M. A. Rosen, *Thermodynamic analysis of a novel combined cooling, heating and power system driven by solar energy.* Applied Thermal Engineering, 2018.**129**: p. 1219-1229.

13. Yılmaz, F., *Thermodynamic performance evaluation of a novel solar energy based multigeneration system.* Applied Thermal Engineering, 2018. **143**: p. 429-437.

14. Zhao, L., Y. Zhang, S. Deng, J. Ni, W. Xu, M. Ma and Z. Yu, *Solar driven ORC-based CCHP: Comparative performance analysis between sequential and parallel system configurations.* Applied Thermal Engineering, 2018. **131**: p. 696-706.

15. Cengel, Y. and A. J. Ghajar, *Heat And Mass Transfer : Fundamentals And Application.* 5th edition, McGraw-Hill Science, 2014.

16. Cengel, Y. and M. A. Boles, *Thermodynamics: An Engineering Approach,* 8th edition, McGraw-Hill Science, 2015.

17. Meteoroloji Genel Müdürlüğü, Available from: https://www.mgm.gov.tr/veridegerlendirme/il-ve-ilceler-istatistik.aspx

18. Yigit, A. and I.Atmaca, *Güneş Enerjisi Mühendislik Uygulamaları.* 1st edition, Dora Yayınları, 2018.

Research Article

Estimation of PM$_{10}$ concentrations in Turkey based on Bayesian maximum entropy

Özlem Baydaroğlu Yeşilköy [a], *

[a]Altınbaş University, School of Engineering and Natural Sciences, Department of Civil Engineering, İstanbul/Turkey

ARTICLE INFO

ABSTRACT

Spatial and temporal distribution of PM$_{10}$ is modeled by Bayesian Maximum Entropy (BME) method. It is the spatiotemporal estimation method which combines exact measurements with the secondary information by considering local uncertainties. In this study, daily average PM$_{10}$ data are used to generate spatial and temporal PM$_{10}$ maps. Both annual and seasonal estimations have been realized. This is the first study which concentrates on spatiotemporal distribution of PM$_{10}$ for all regions of Turkey by using Bayesian Maximum Entropy method. Error variances are used as performance criteria in both seasonal and annual predictions. All prediction results stay within the limits of the confidence intervals. In addition, unknown PM$_{10}$ values are estimated, including PM$_{10}$ values over the seas. It is thought that the PM$_{10}$ maps which show all regions of Turkey in detail are quite invaluable and informative.

1. Introduction

As a mixture of solid and liquid particles, particulate matter (PM) may be originated from natural sources such as windblown dust, anthropogenic sources like agricultural and industrial activities, fossil fuel combustion. Since PMs are of vital significance in respect to air quality phenomenon, estimation and forecast of it enables decision-makers to take precautions.

Bayesian Maximum Entropy (BME) [1, 2, 3, 4, 5, 6] is a nonlinear geostatistical approach. In this method, Bayesian conditionalization and entropy maximization are combined to generate spatiotemporal mapping. When compared to other methods, it is seen that the confidence levels provided by BME are narrow. Moreover, error variances are used as performance criteria of results [7].

BME is the only approach which uses not only raw data but also auxiliary data (soft data) in a spatiotemporal mapping. In other words, different kinds of information are merged [8]. BME realizes gaining, interpreting and processing of information in three stages.

BME is employed for estimation and prediction of different kinds of variables, such as ozone [9], soil moisture [10], rainfall [11], soil salinity [12], sea surface temperature [13] and wind [14].

Although distribution of PM is valuable individually for air quality management purposes, it is also associated with climatological conditions, agricultural activities, industries, residential heating types, topographical features and populations. There are many PM studies in Turkey. Some inventory and estimation studies of PM$_{10}$ can be seen below. Alyuz and Alp [15] prepared an emission inventory of primary air pollutants for Turkey investigating in 7 main categories and 53 sub-sectors. It was stated that the calculated PM emission value for the year 2010 was 48.853 t and PM emissions were mainly emitted from the mineral, metallurgical, pulp and paper industries. Furthermore, Saharan dust was the most significant source of PM in Turkey [16]. Güler ve İşçi [17] used a Fuzzy C-Auto Regressive Model (FCARM) and Autoregressive Model (AR) to reflect the regional behavior of weekly PM$_{10}$ concentrations. Results showed that the former model provided better prediction accuracy. Ozel ve Cakmakyapan [18] developed a new approach which was based on gamma-Poisson process in

order to predict PM_{10} concentrations in Central Anatolia Region by using PM_{10} data from 24 air quality monitoring stations for the years between 2007 and 2013. In this study, daily average PM_{10} concentration was found as 148 $\mu g/m^3$. Im et al. [19] investigated high winter-time PM_{10} values using a high resolution the WRF/CMAQ (Weather and Forecasting Model/Community Modelling Air Quality Model) mesoscale model system. Calculated PM_{10} levels by the model underestimated the observations with an average of 10% at the sampling station. Şahin et al. [20] proposed the cellular neural network (CNN) method in order to modeling air pollutants such as PM_{10} concentrations in İstanbul. Meteorological parameters were used for model inputs. Results of the CNN were compared to statistical persistence method (PER) results and it was seen that the CNN and PER outputs were correlated with observations via statistical performance indices. Results indicated that the CNN was more accurate than the PER. Karaca [21] developed a classification method in order to categorize air zones. Geographic Information System (GIS)-based interpolation method and statistical analysis were used in order to generate PM_{10} pollution profiles for Turkey.

There are also many international studies about modeling, analyzing and forecasting of PM_{10} values in the literature. For instance, chemistry-transport models (CTMs) [22, 23], ensemble models with bias-correction techniques [24] and with machine learning algorithms [25], stepwise regression and wavelet analysis [26], universal kriging, land use regression method [27] were implemented in order to forecast PM_{10} levels. Other studies which used BME in prediction are given below. Christakos and Serre [28] analyzed PM distributions in North Carolina by the BME mapping method. Because one of the most significant phenomena was assessing the uncertainty for each of space/time pollution maps in a stochastic pollutant analysis, standard deviations of BME errors were used as a measure of uncertainty. Besides, standard deviations were zero at monitoring stations while they took higher values at regions away from these stations [28]. Results of the study indicated that the PM_{10} maps showed clear variability. Another PM study was realized by Christakos and Serre [29]. They modeled space/time distribution of PM_{10} for a six-year period and optimized its monitoring network for Thailand. In the north of the city, there was a district seasonal fluctuation of PM_{10} values between December and February where this kind of fluctuation in the South Thailand was not seen. Residential exposure of ambient ozone and PM_{10} values were estimated using BME method at multiple time scales by Yu et al. [30]. The same study was carried out with simple kriging and all results were compared. According to results, the usage of soft data enhanced the accuracy of the forecast. Fernando et al. [31] used a stochastic NN model based on neural network called EnviNNet and CMAQ to predict PM in Phoenix. It was found that EnviNNet predicted PM_{10} concentrations better than the CMAQ. Akita et al. [32] proposed a moving window-BME (MWBME) method in order to forecast $PM_{2.5}$ concentrations. In the study, the results were compared to the stationary kriging (SK) and moving window kriging (MWK). It was seen that MWBME had a good capability to catch the highest correlation between observations and forecast results. $PM_{2.5}$ values in United States were estimated using a Land Use Regression Model (LUR) and BME by Beckerman et al. [33] and it was seen that the hybrid model gave more accurate results than each of other models.

In this study, daily average PM_{10} data from 145 air quality monitoring stations of Ministry of Environment and Urbanization of Turkey have been used. Either annual or seasonal estimations have been realized. Zero and constant-local mean (simple and ordinary kriging) are chosen in the last stage of BME.

In all estimations, Bayesian Maximum Entropy Graphical Users Interface (BMEGUI) has been used [see 34].

2. Materials and Methods

2.1 Materials

2.1.1 Study site description

Turkey is a country between $26^0 - 45^0 E$ meridians and $36^0 - 42^0 N$ parallels as seen in Figure 1 (a) and it covers a 783.562 km^2 area. However, maximum and minimum estimation points are taken as 45^0 for the east, 25^0 for the west, 42.1^0 for the north and 36^0 for the south to in order to include all stations. For instance, the spatial location of Çanakkale Gökçeada station is between $25.91^0 W$ and $40.19^0 S$. Figure 1 (b) shows regions of Turkey.

2.1.2. Data description

In this study, the data between the years 2012 and 2016 have been utilized. Means and standard deviations of the data with Gaussian distribution were used as soft data. The data was taken from the web site of Turkey Ministry of Environment and Urban Planning for each station.

Both annual and seasonal estimations have been realized. In the annual estimation, 0.25^0, 0.5^0, 1^0 and 1.5^0 are used as spatial lags where ne week, two weeks and one month are taken as temporal lags. Zero and constant-local mean are chosen as kriging methods. Table 1 shows the study matrix for the annual prediction.

Map of stations are given in Figure 2 (a) and the data points after the kriging of BME approach is given in Figure 2 (b).
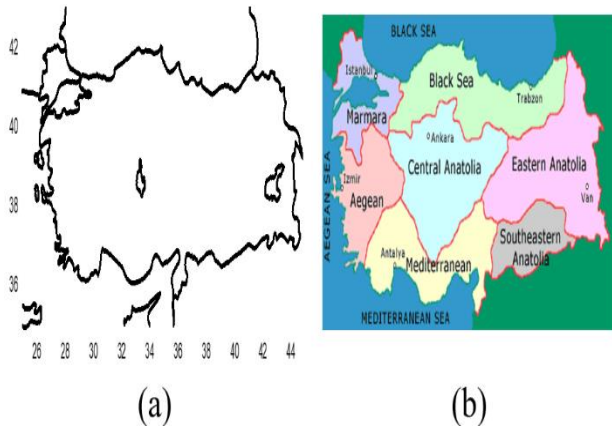
Figure 1. (a) Turkey latitude and longitude map (b) Turkey regions map

Table 1. Study matrix for the annual prediction

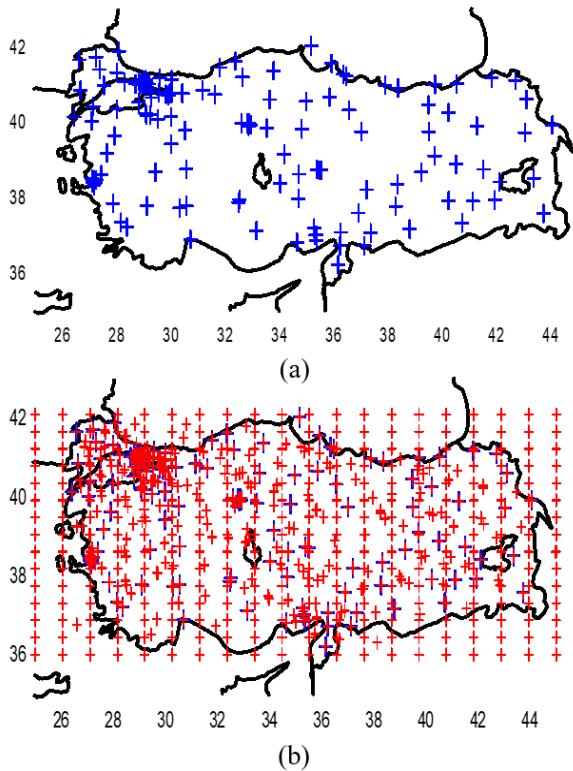| Spatial Lag	Temporal Lag	Local Mean
0.25^0 0.5^0 1^0 1.5^0	1 week 2 weeks 1 month	Zero (Simple kriging) Constant (Ordinary kriging)

(a)

(b)

Figure 2. (a) The stations of the data (b) The data points after the kriging of BME approach

2.2 Method

2.2.1 The Bayesian Maximum Entropy (BME) Method

Space-time interpolation techniques do not consider secondary variables related to primary variables via empirical law while they explain raw data with cross-correlation between primary and secondary variables.

However, empirical laws and soft data can be regarded for by BME [11]. This is a special property of BME.

Bayesian Maximum Entropy (BME) [1, 2, 3, 4, 5, 6] is a nonlinear geostatistical approach. It realizes spatiotemporal analysis and uses spatiotemporal domains. During processing of the data, physical rules, experiences, theories, high order space/time moments, outputs of models etc. are incorporated to the process.

In modern geostatistics, data sets χ_{data} consist of two basis categories as seen below [35].

$$S: \chi_{data} = (\chi_{hard}, \chi_{soft}) = (\chi_1, \dots, \chi_m) \quad (1)$$

where χ_{hard} and χ_{soft} show hard and soft data, respectively. In relation to hard data, specificatory knowledge for the points $m_h (< m)$ is

$$S: \chi_{hard} = (\chi_1, \dots, \chi_{m_h}) \quad (2)$$

Specificatory knowledge base (S) contains single-valued measurements $\chi_i (i = 1, \dots, m_h)$ in space/time. Regarding to the soft data, the specificatory knowledge for the remaining points $m_s = m - m_h$ is given as

$$S: \chi_{soft} = (\chi_{m_{h+1}}, \dots, \chi_m) \quad (3)$$

Figure 3 shows a framework of BME approach.

A spatiotemporal analysis begins with general knowledge base G. At the prior stage, the joint probability density function $f_G(\chi_{map})$ is calculated via general knowledge and maximum entropy theory is applied [36].

At the meta-prior stage, hard and soft data and specificatory knowledge base S are considered.

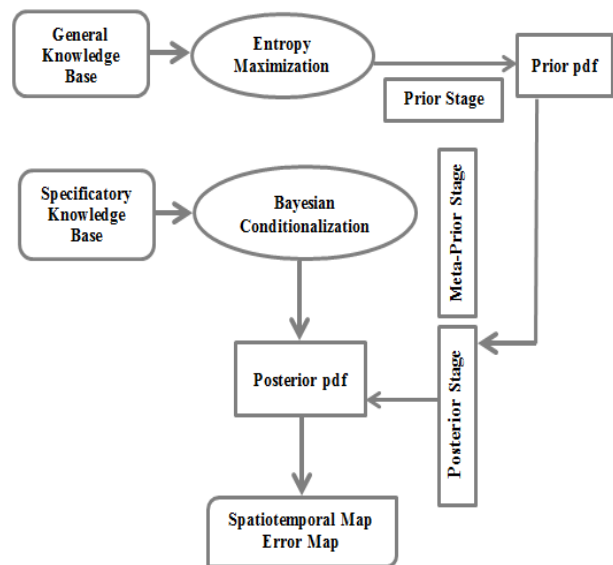At the posterior stage, S and G are integrated to the mapping process [35].

Figure 3. A conceptual framework of the BME approach.

BME posterior probability density function $f_\kappa(\chi_k)$ is as follows [4, 35]

$$f_\kappa(\chi_k) = A^{-1} \int d\chi_{soft} f_S(\chi_{soft}) f_G(\chi_{hard}, \chi_{soft}, \chi_k) \quad (4)$$

where $\kappa = G \cup S$ is available all physical knowledge and A is a normalization parameter.

In this study, because it minimizes mean squared estimation errors, the conditional mean estimation is used.

As a rule, uncertainty measurements are given with variances of forecast errors [37, 38]. The variance of BME posterior pdf can be taken as a measure of a forecast error. Because this value is equivalent to the variance of a forecast error $e_k = x_k - \bar{x}_{k|\kappa}$, it is used as performance criteria.

For Gaussian posterior pdf, the probability of x_k which changes between the interval $[\bar{x}_{k|\kappa} - 1.96\sigma_{k|\kappa}, \bar{x}_{k|\kappa} + 1.96\sigma_{k|\kappa}]$ is 95% [7].

3. Results

Figure 4 a to f shows histograms and summary statistics for daily mean PM_{10} concentrations. From Figure 4(a) to 4(f), it is easily seen that daily mean PM_{10} concentrations are right-skewed series, namely; there is a density of low PM_{10} concentrations.

3.1. Annual prediction of PM_{10}

Regarding the study matrix, PM_{10} concentrations were predicted and the best results are obtained with a 1.5^0-spatial range and 1-week-temporal range and constant local mean. In Figure 5 (a) and (b), the mean PM_{10} concentrations and error variance map can be seen, respectively.

Figure 5. (a) Predicted mean PM_{10} values map (b) Error variance map.

From Figure 5 (a), the spatial variability can be seen. According to the national air quality index, the national limit value of PM_{10} for the year 2017 is 70 μg/m^3. Even though the mean PM_{10} concentration of Turkey is approximately 56 μg/m^3, it is apparent that there are some regions which have PM_{10} concentrations that are beyond the national limit. Especially in the Southeastern Anatolia Region, high PM_{10} concentrations are prominent. The cities with high PM_{10} concentration are Aydın, Afyon, Zonguldak, Kastamonu, Sinop, Adana, Samsun, Ordu, Giresun, Şanlıurfa, Diyarbakır, Batman, Muş, Siirt, Ağrı, Kars, Hakkâri and Iğdır. Some former studies [39, 40, 16, 41] have remarked that usage of the fossil fuels for heating is relatively low in Southeastern Anatolia Region because winter temperatures in the region are not higher than Central and Eastern Anatolia Region. PM_{10} concentrations of the Southeastern Anatolia

Region increase in spring, summer and autumn seasons due to desert dusts transported from North Africa, Arabia and Syria. Because this region is close to desert areas, on the transition path of mesoscale cyclones and located in Western winds zones due to its geographical location, desert dusts are the most important source of air pollution. Furthermore, the reason of high PM_{10} concentrations in the Black Sea Region may be explained with dry atmospheric conditions and thick inversion level near the ground surface of the Marmara Region as specified by Baltaci [41]. In addition, a thick dust layer transported from Libya and transportation of sea spray causes high PM_{10} concentrations in some cities in the Aegean Region [41, 42].

From Figure 5 (b), it can be said that error variance values of the areas which have higher PM_{10} concentrations are prominently low when compared to other areas with higher error variances. It is thought that, the reason of high error variance values may be due to the lack of air quality monitoring stations and/or available data in those areas.

3.2. Seasonal prediction of PM_{10}

Seasonal PM_{10} concentrations were predicted for all seasons, and best results were obtained with a 1^0-spatial range and 1-week-temporal range and for constant local mean for each of them. Figure 6 shows predicted mean PM_{10} concentration maps and error variance maps for spring, summer, autumn and winter seasons.

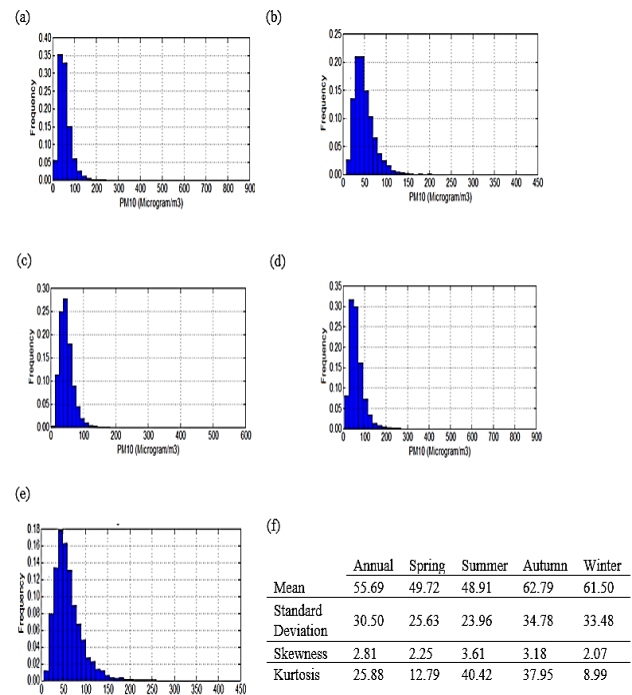|	Annual	Spring	Summer	Autumn	Winter
Mean	55.69	49.72	48.91	62.79	61.50
Standard Deviation	30.50	25.63	23.96	34.78	33.48
Skewness	2.81	2.25	3.61	3.18	2.07
Kurtosis	25.88	12.79	40.42	37.95	8.99

Figure 4. Histograms of daily mean PM_{10} concentrations (a) for all years (b) for spring seasons (c) for summer seasons (d) for autumn seasons (e) for winter seasons (f) Summary statistics
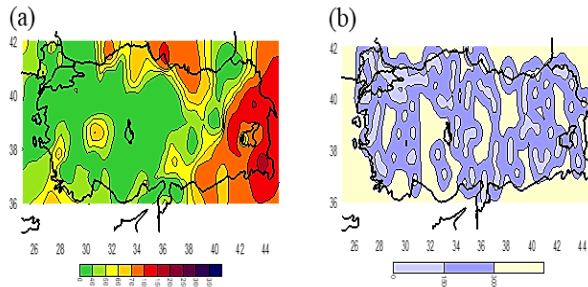
(a)

(b)

Figure 5. (a) Predicted mean PM$_{10}$ values map (b) Error variance map
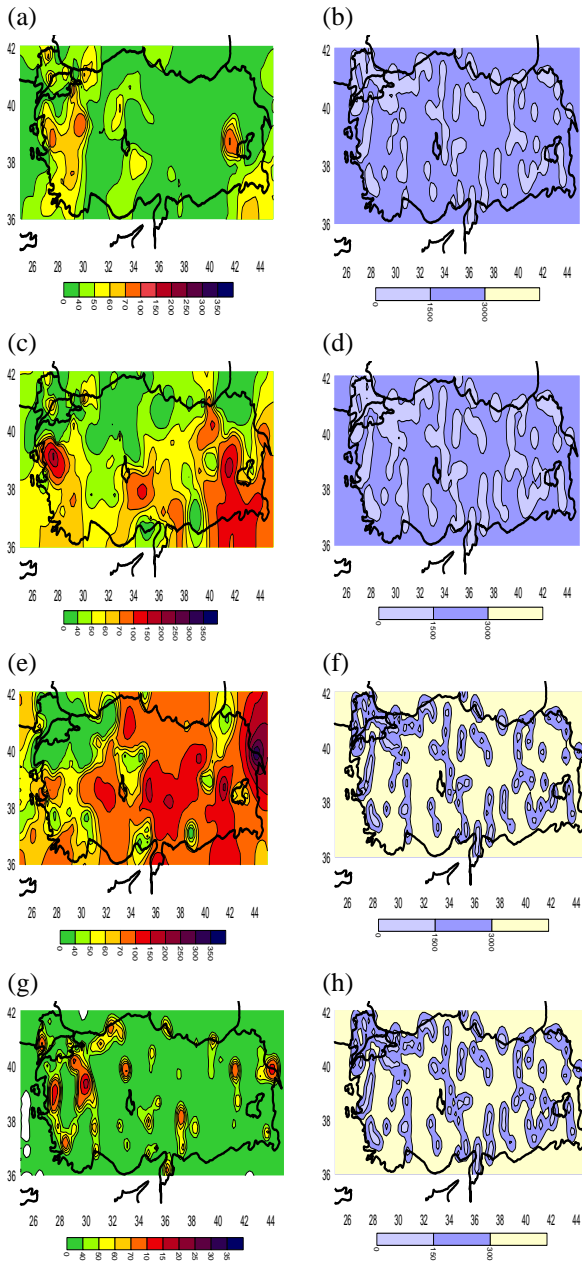
(a)

(b)

(c)

(d)

(e)

(f)

(g)

(h)

Figure 6. (a) Predicted mean PM$_{10}$ values map for spring seasons (b) Error variance map for spring seasons (c) Predicted mean PM$_{10}$ values map for summer seasons (d) Error variance map for summer seasons (e) Predicted mean PM$_{10}$ values map for autumn seasons (f) Error variance map for autumn seasons (g) Predicted mean PM$_{10}$ values map for winter seasons (h) Error variance map for winter seasons

For spring seasons, it can be said that average PM$_{10}$ concentrations are between 24.1 μg/m^3 and 75.3 μg/m^3 as seen in the Figure 4 (f). The stations which have PM$_{10}$ concentrations more than 70 μg/m^3 are Muş, Kütahya, Tekirdağ-Merkez, Bitlis, Yalova, Manisa, Denizli-Bayramyeri, Kırklareli, İstanbul-Aksaray, Kocaeli-Kandıra and Bursa. As seen from Figure 6 (a), Eastern and Central Black Sea Region are associated well with PM$_{10}$ concentrations whereas there are high PM$_{10}$ concentrations in Marmara, Aegean and Southeastern Regions. Besides, the cities which have the lowest-PM$_{10}$ concentrations are Bingöl, Adana, Tunceli, Erzurum and Ardahan.

For summer seasons, it is determined from the Figure 4 (f) that average PM$_{10}$ concentrationsare between 25 μg/m^3 and 72.9 μg/m^3. The stations with PM$_{10}$ concentrations larger than 70 μg/m^3 are Manisa, Muş, Siirt, Niğde, Hakkâri, Bayburt, Kayseri-Hürriyet, Mardin, Ankara-Cebeci, Trabzon-Meydan, Balıkesir, İzmir, Tekirdağ, İstanbul, Denizli, Kocaeli, Karaman, Aksaray, Osmaniye, Kahramanmaraş, Gaziantep, Elazığ, Erzincan, Diyarbakır, Batman and Iğdır. In Figure 6 (c), it is clearly seen that there is a distinctive variability. While relatively high PM$_{10}$ concentrations are appeared in the south and central part of the country, the north of the country has quite low PM$_{10}$ concentrations. From this figure, it is concluded that nonconsumption of fossil fuels for residential heating is a decisive factor in summer seasons for most of the northern Turkey. Moreover, effects of desert dusts are explicit in the southeastern, eastern Anatolia and eastern Mediterranean Regions. In this season, the cities with the lowest-PM$_{10}$ concentrations are Kocaeli, Şanlıurfa, Kırklareli, İstanbul and Kırıkkale.

For autumn seasons, it is seen in the Figure 4 (f), average PM$_{10}$ concentrations change between 28 μg/m^3 and 97.6 μg/m^3. The stations which have PM$_{10}$ concentrations above 70 μg/m^3 are Iğdır, Kayseri-Hürriyet, Muş, Erzincan, Kahramanmaraş-Elbistan, Osmaniye, Siirt, Hatay-Antakya, Batman, Kars-İstasyon Mahallesi, İzmir, Manisa, Afyon, Konya, Ankara, Karaman, Çankırı, Kastamonu, Niğde, Çorum, Amasya, Samsun, Tokat, Sivas, Gaziantep, Sivas, Ordu, Adıyaman, Malatya, Elazığ, Trabzon, Bayburt, Diyarbakır, Mardin, Ardahan, Ağrı, Hakkari and Van. Figure 6 (e) show that there are rather high PM$_{10}$ concentrations are common in Turkey except Marmara Region. In this season, the cities with the lowest-PM$_{10}$ concentrations are Çanakkale, İstanbul, Kocaeli, Yalova and Tekirdağ.

For winter seasons, average PM$_{10}$ concentrations change between 28 μg/m^3 and 95 μg/m^3 as seen in the Figure 4 (f). The stations which have PM$_{10}$ concentrations

above 70 μ g/m^3 are Kütahya, Iğdır, Ankara-Kayaş, Manisa-Soma, Bursa, Bursa-Beyazıt Caddesi, Erzurum, Edirne-Keşan, Bursa-Kestel, Muğla-Musluhittin, Edirne, İstanbul, Denizli, Uşak, Kocaeli, Iğdır, Eskişehir, Afyon, Isparta, Antalya, Düzce, Zonguldak, Karabük, Ankara, Niğde, Adana, Kayseri, Hatay, Kahramanmaraş, Gaziantep, Trabzon, Muş, Ağrı and Hakkâri. From Figure 6 (g), it can be concluded that desert dusts are the most important reason for large PM$_{10}$ concentrations. Other than the abovementioned parts of Turkey, PM$_{10}$ levels are low in winters. Furthermore, it can be said that the areas which have higher PM$_{10}$ concentrations are generally industrial zones.

4. Conclusion

To decrease environmental pollution and public health risks, spatiotemporal mapping of air pollutants is necessary. From this point of view, the first and only spatiotemporal PM$_{10}$ study including all regions of Turkey has been realized.

All variables like climatological conditions, agricultural activities, industries, residential heating types, topographical features, populations should be considered when interpreting PM$_{10}$ levels. According to annual prediction results, Southeastern Anatolia Region has high PM$_{10}$ concentrations. Closeness to deserts, western wind zones, being on the transition path of mesoscale cyclones can be regarded as reasons of high PM$_{10}$ concentrations. Moreover, the eastern and middle part of the Black Sea Region, northeastern part of Central Anatolia, Aegean Region and eastern part of Turkey are high-PM$_{10}$ zones.

According to seasonal PM$_{10}$ maps, there are high PM$_{10}$ concentrations especially in Summer and Autumn seasons. The highest PM$_{10}$ concentrations are realized in Autumn seasons. Apart from major part of the Marmara Region, almost all regions have high PM$_{10}$ concentrations in autumns. This situation can be explained by either the season is the desert dusts effective season or residential heating begins. Besides, the reason of relatively clear appearance of the Marmara Region may be due to wind effects. The PM$_{10}$ prediction map of Summer seasons indicates high PM$_{10}$ concentrations in the southwestern, eastern and northeastern part of Turkey and inner Aegean Region. The increase of PM$_{10}$ in Autumn and Summer seasons may be associated from agricultural activities in addition to lack of rain and desert dusts. Also, these regions are less covered by forests pretending like natural dust filters than Black Sea Region as stated by Karaca [21].

Although Winter seasons have generally the most polluted air due to traffic-based emissions and residential heating, Turkey shows a different PM$_{10}$ profile. Some

regions of the Marmara, inner Aegean, Eastern and Central Anatolia Regions have high PM$_{10}$ concentrations. The sources of this pollution may be industries, heating, traffic and climatic conditions. In addition, the Marmara, Aegean and Southeastern Regions have high PM$_{10}$ concentrations in Spring seasons.

When viewed error variance maps, error variance values are higher in Autumn and Winter seasons than in Spring and Summer seasons since Autumn and Winter seasons have higher fluctuations and variability of PM$_{10}$ concentrations and this situation may cause high error variance values.

One of the most important difficulties faced by the study is the lack of available data. The problems of missing or unreasonable data should be solved and the number of mobile stations should be increased.

For the future studies, it is aimed to realize multi-point mappings of PM$_{10}$ and generating other air pollutants' maps. Furthermore, epidemiologic studies which are focusing on the relationship between PM$_{10}$ values and some diseases especially respiratory disorders should be analyzed and mapped.

Declaration

The author(s) declared no potential conflicts of interest with respect to the research, authorship, and/or publication of this article. The author(s) also declared that this article is original, was prepared in accordance with international publication and research ethics, and ethical committee permission or any special permission is not required.

References

1. Christakos, G. A *Bayesian maximum-entropy view to the spatial estimation problem*. Mathematical Geology, 1990. **22**(7), 763-777.

2. Christakos, G. *Some applications of the Bayesian, maximum entropy concept in Geostatistics*. Fundamental Theories of Physics, 1991a. p.215-229. Kluwer Acad. Publ. Dordrecht, The Netherlands.

3. Christakos, G. *A theory of spatiotemporal random fields and its application to space-time data processing*. IEEE Trans., Systems, Man & Cybernetics, 1991b. V. 21, No.4, p. 861-875.

4. Christakos, G. *Random Field Models in Earth Sciences*. 1992, Academic Press, San Diego, CA.

5. Christakos, G. *Spatiotemporal information systems in soil and environmental sciences*. Geoderma, 1998a. **85**(2), 141-179.

6. Christakos, G. *Multi-point BME space/time mapping of environmental variables*. Computational Methods in Water Resources XII 1998b, Computational Methods in Surface and Groundwater Transport. Computational Mechanics Publ., 1998b. Vol.2., p. 289-296, Southampton, UK.

7. Serre M.L. and Christakos, G. *Modern Geostatistics: Computational BME analysis in the light of uncertain physical knowledge-the Equus Beds study*. Stochastic

Environmental Research and Risk Assessment, 1999. **13**(1-2), p.1-26.

8. Serre M.L., Kolovos, A., Christakos, G., and Modis, K. *An application of the holistochastic human exposure methodology to naturally occuring arsenic in bangladesh drinking water*. Risk Analysis, 2003. **23**(3), p.525-528.

9. Bogaert, P., Christakos, G., Jerrett, M., and Yu, H.L. *Spatiotemporal modelling of ozone distribution in the State of California*. Atmospheric Environment, 2009. **43**(15), p.2471-2480.

10. Fan, L., Xiao, Q., Wen, J., Liu, Q., Jin, R., You, D., and Li, X. *Mapping high-resolution soil moisture over heterogeneous cropland using multi-resource remote sensing and ground observations*. Remote Sensing, 2015. **7**, p.13273-13297.

11. Shi, T., Yang, X., Christakos, G., Wang, J. and Li, L. *Spatiotemporal interpolation of rainfall by combining bme theory and satellite rainfall estimates*. Atmosphere, 2015. **6**(9), p.1307-1326.

12. Douaik, A., Van Meirvenne, M., Toth, T., and Serre, M. *Space-time mapping of soil salinity using probabilistic bayesian maximum entropy*. Stoch. Envir. Res. And Risk Ass., 2004. **18**, p.219-227.

13. Tang, S., Yang, X., Dong, D., and Li, Z. *Merging daily sea surface temperature data from multiple satellites using a Bayesian maximum entropy method*. Front. Earth Sci., 2015. **9**(4): p.722-731.

14. Baydaroğlu, Ö., and Koçak, K. *Spatiotemporal analysis of wind speed via the Bayesian Maximum Entropy*. Environmental Earth Sciences, 2019. **78**(1), 17.

15. Alyuz, U., Alp, K. *Emission inventory of primary air pollutants in 2010 from industrial processes in Turkey*. Science of the Total Environment, 2014. **488**, p.369-381.

16. Kabatas, B., Unal, A., Pierce, R.B., Kindap, T., and Pozzoli, L. *The contribution of Saharan dust in PM_{10} concentration levels in Anatolian Peninsula of Turkey*. Science of the Total Environment, 2014. **488**, p.413-421.

17. Güler, N., and İşçi, Ö.G. *The regional prediction model of PM_{10} concentrations for Turkey*. Atmospheric Research, 2016. **180**, p.64-77.

18. Ozel, G., and Cakmakyapan, S. *A new approach to the prediction of PM_{10} concentrations in Central Anatolia Region, Turkey*. Atmospheric Pollution Research, 2015. **6**(5), p.735-741.

19. Im, U., Markakis, K., Unal, A., Kindap, T., Poupkou, A., Incecik, S., ..., and Mihalopoulos, N. *Study of a winter PM episode in Istanbul using the high resolution WRF/CMAQ modeling system*. Atmospheric Environment, 2010. **44**(26), p.3085-3094.

20. Şahin, Ü.A., Ucan, O.N., Bayat, C., and Tolluoglu, O. *A new approach to prediction of SO2 and PM_{10} concentrations in Istanbul, Turkey: Cellular Neural Network (CNN)*. Environmental Forensics, 2011. **12**(3), p.253-269.

21. Karaca, F. *Determination of air quality zones in Turkey*. Journal of the Air & Waste Management Association, 2012. **62**(4), p.408-419.

22. Konovalov, I.B., Beekmann, M., Meleux, F., Dutot, A, and Foret, G. *Combining deterministic and statistical approaches for PM_{10} forecasting in Europe*. Atmospheric Environment, 2009. **43**(40), p.6425-6434.

23. Nonnemacher, M., Jakobs, H., Viehmann, A., Vanberg, I., Kessler, C., Moebus, S., ..., and Heinz Nixdorf Recall Study Investigative Group. *Spatio-temporal modelling of residential exposure to particulate matter and gaseous pollutants for the Heinz Nixdorf Recall Cohort*. Atmospheric Environment, 2014. **91**, p.15-23.

24. Djalalova, I., Wilczak, J., McKeen, S., Grell, G., Peckham, S., Pagowski, M., ..., and McHenry, J. *Ensemble and bias-correction techniques for air quality model forecasts of surface O3 and PM 2.5 during the TEXAQS-II experiment of 2006*. Atmospheric Environment, 2010. **44**(4), p.455-467.

25. Debry, E., and Mallet, V. *Ensemble forecasting with machine learning algorithms for ozone, nitrogen dioxide and PM_{10} on the Prev'Air platform*. Atmospheric Environment, 2014. **91**, p.71-84.

26. Chen, Y., Shi, R., Shu, S., and Gao, W. *Ensemble and enhanced PM_{10} concentration forecast model based on stepwise regression and wavelet analysis*. Atmospheric Environment, 2013. **74**, p.346-359.

27. Kim, S.Y., and Song, I. *National-scale exposure prediction for long-term concentrations of particulate matter and nitrogen dioxide in South Korea*. Environmental Pollution, 2017. **226**, p.21-29.

28. Christakos, G. and Serre, M.L. *BME analysis of spatiotemporal particulate matter distributions in North Carolina*. Atmospheric Environment, 2000. **34**(20), p.3393-3406.

29. Puangthongthub, S., Wangwongwatana, S., Kamens, R.M., and Serre, M.L. *Modeling the space/time distribution of particulate matter in Thailand and optimizing its monitoring network*. Atmospheric Environment, 2007. **41**(36), p.7788-7805.

30. Yu, H.L., Chen, J.C., Christakos, G., and Jerrett, M. *BME Estimation of Residential Exposure to Ambient PM_{10} and Ozone at Multiple Time Scales*. Environmental Health Perspectives, 2009. **117**(4), 537.

31. Fernando, H.J., Mammarella, M.C., Grandoni, G., Fedele, P., Di Marco, R., Dimitrova, R., and Hyde, P. *Forecasting PM 10 in metropolitan areas: efficacy of neural networks*. Environmental Pollution, 2012. **163**, p.62-67.

32. Akita, Y., Chen, J.C., and Serre, M.L. *The moving-window Bayesian maximum entropy framework: estimation of PM2. 5 yearly average concentration across the contiguous United States*. Journal of Exposure Science and Environmental Epidemiology, 2012. **22**(5), p.496-501.

33. Beckerman, B.S., Jerrett, M., Serre, M., Martin, R.V., Lee, S.J., Van Donkelaar, A., ..., and Burnett, R.T. *A hybrid approach to estimating national scale spatiotemporal variability of PM2.5 in the contiguous United States*. Environmental Science & Technology, 2013. **47**(13), 7233.

34. Bayesian Maximum Entropy Graphical Users Interface (BMEGUI), University of North Carolina. [cited 2015 May 1]. Available from: http://www.unc.edu/depts/case/BMEGUI/BMEGUI3.0.1/BMEGUI3.0.1_WEB_2014. htm

35. Christakos, G. *Modern Spatiotemporal Geostatistics,* 2000. Oxford University Press.

36. Gao, S., Zhu, Z., Liu, S., Jin, R., Yang, G., and Tan, L. *Estimating the spatial distribution of soil moisture based on Bayesian maximum entropy method with auxiliary data from remote sensing*. International Journal of Applied Earth Observation and Geoinformation, 2014*. **32**, p.54-66.

37. Olea, R.A. *Understanding Geostatistics*. Course Notes, 1997. Civil Engineering Dept., Univ. of Kansas, Lawrence, KS.

38. Bogaert, P., and Christakos, G. *Spatiotemporal analysis and processing of thermometric data over* Belgium. Journal of Geophysical Research-All Series-, 1997. **102**, p.25-831.

39. Şengün, T. and Kıranşan, K. *Güneydoğu Anadolu Bölgesi'nde çöl tozlarının hava kalitesi üzerine etkisi.* Türk Coğrafya Dergisi, 2012. (**59**) (in Turkish).

40. Dolar, A. and Saraç, H.T.K. *Türkiye'nin doğu illerindeki hava Kalitesinin PM$_{10}$ açısından incelenmesi* (In Turkish) Iğdır Univ. J. Inst. Sci. & Tech.*,* 2015. **5**(4): p.25-32.

41. Baltaci, H. *Spatial and Temporal Variation of the Extreme Saharan Dust Event over Turkey in March 2016*. Atmosphere, 2017. **8**(2), 41.

42. Koçak, M., Mihalopoulos, N., and Kubilay, N. *Contributions of natural sources to high PM10 and PM2.5 events in the eastern Mediterranean*. Atmospheric Environment, 2007. **41**(18), p. 3806-3818.

Correction

Correction to: An experimental study on production of intelligent textile by using ionochromic materials

Aslıhan Koruyucu [a,*] iD *and Ayben Pakolpakçıl* [b] iD

ª Namık Kemal University, Çorlu Faculty of Engineering, Department of Textile Engineering, Turkey
ᵇ Bursa Uludağ University, Graduate School of Natural and Applied Sciences, Görükle, Bursa, Turkey

Corrections to: Int Adv Res Eng J 03(03):182-188, 2019

DOI: 10.35860/iarej.526440

There was a spelling error in the title of the original article. "*ionocromic*" word was corrected as "*ionochromic*" in the title.

Author name of "*Ayben Pakolpakçıl*", her affiliaction "*b) Bursa Uludağ University, Graduate School of Natural and Applied Sciences, Görükle, Bursa, Turkey*", her E-mail address "*ayben_p@yahoo.com*" and her ORCID "*0000-0002-6981-4980*" were added.

Also the footnote "*This article is based on the master's degree thesis of Ayben Pakolpakçıl*" was added.

All necessary corrections are presented on this page.

Authors apologies for the corrections after publication of the original article.

Declaration

The author(s) declared no potential conflicts of interest with respect to the research, authorship, and/or publication of this article after publication this correction. The author(s) also declared that the article is original, was prepared in accordance with international publication and research ethics, and ethical committee permission or any special permission is not required.

The original article can be found online at
https://doi.org/10.35860/iarej.526440

---

* Corresponding author. Tel.: +90 282 2502334; Fax: +90 282 250 9924.
E-mail addresses: adelituna@nku.edu.tr *(A. Koruyucu)*, ayben_p@yahoo.com *(A. Pakolpakçıl)*
ORCID: 0000-0002-8443-5188 *(A. Koruyucu)*, 0000-0002-6981-4980 *(A. Pakolpakçıl)*
Note: This article is based on the master's degree thesis of Ayben Pakolpakçıl
DOI: 10.35860/iarej.686847